

DETECTION OF HIGH-FREQUENCY X-RAY VARIABILITY  
IN A BLACK HOLE TRANSIENT WITH USA

A DISSERTATION  
SUBMITTED TO THE DEPARTMENT OF PHYSICS  
AND THE COMMITTEE ON GRADUATE STUDIES  
OF STANFORD UNIVERSITY  
IN PARTIAL FULFILLMENT OF THE REQUIREMENTS FOR THE DEGREE OF  
DOCTOR OF PHILOSOPHY

Gayane Shabad

October 2000

© Copyright by Gayane Shabad 2001  
All Rights Reserved

I certify that I have read this dissertation and that in my opinion it is fully adequate, in scope and quality, as dissertation for the degree of Doctor of Philosophy.

---

Elliott D. Bloom (Principal Advisor)

I certify that I have read this dissertation and that in my opinion it is fully adequate, in scope and quality, as dissertation for the degree of Doctor of Philosophy.

---

Peter F. Michelson

I certify that I have read this dissertation and that in my opinion it is fully adequate, in scope and quality, as dissertation for the degree of Doctor of Philosophy.

---

Robert V. Wagoner

Approved for the University Committee on Graduate Studies



## ABSTRACT

Studies of high-frequency variability (above  $\sim 100$  Hz) in X-ray binaries provide a unique opportunity to explore the fundamental physics of spacetime and matter, since the orbital timescale on the order of several milliseconds is a timescale of the motion of matter through the region located in close proximity to a compact stellar object.

The detection of weak high-frequency signals in X-ray binaries depends on how well we understand the level of Poisson noise due to the photon counting statistics, i.e. how well we can understand and model the detector deadtime and other instrumental systematic effects. We describe the preflight timing calibration work performed on the Unconventional Stellar Aspect (USA) X-ray detector to study deadtime and timing issues. We developed a Monte Carlo deadtime model and deadtime correction methods for the USA experiment. The instrumental noise power spectrum can be estimated within  $\sim 0.1\%$  accuracy in the case when no energy-dependent instrumental effect is present. We also developed correction techniques to account for an energy-dependent instrumental effect. The developed methods were successfully tested on USA Cas A and Cygnus X-1 data. This work allowed us to make a detection of a weak signal in a black hole candidate (BHC) transient.

The evidence for high-frequency signals in BHC binaries is scarce and is just emerging. Five BHC binary sources were reported so far by the Rossi X-Ray Timing Explorer

(RXTE) to contain high-frequency quasi-periodic signals (QPOs) in  $\sim 100\text{--}300$  Hz range. We report the  $20\sigma$  detection of high-frequency variability ( $\sim 40\text{--}300$  Hz) with 7.7% fractional rms amplitude in the BHC X-ray transient XTE J1859+226 with USA. This detection is the first confirmation of high-frequency variability in BHC binaries with a different instrument. The Fourier spectral method was applied to the XTE J1859+226 data with corrections for the deadtime and instrumental effects. The USA measurements can be interpreted as indicating a QPO signal that changes its frequency between three dominant “states” at 67 Hz, 134 Hz and 193 Hz. We discuss the high-frequency QPO detection in XTE J1859+226, as well as similar QPO detections in other black hole candidate binaries, in the context of Keplerian, diskoseismic and relativistic precession theoretical models. Currently, the interpretation of these signals within existing models is ambiguous. We performed an energy-dependent timing analysis of a low-frequency 4.9 Hz QPO, its harmonics, and broad-band noise in XTE J1859+226. The increase of fractional rms amplitude of all noise components with energy is seen. The result, if interpreted within the Compton microscope theoretical model, may indicate that the variability in this frequency range could be confined to the outer parts of the accretion disk.

To those who will be

## ACKNOWLEDGMENTS

I started to study physics when I was little. Those were the eighties in Russia. My country was submerged in stagnation and nothing ever seemed to change. My life was predetermined. I was set to become one of those brilliant Russian physicists. Well, this did not happen. In the years to come, things around me changed fast. My classmates from Moscow University managed to divide Russia's oil supply and other natural resources, became rich and strayed from physics. My classmates from Stanford built the first Internet websites, became even more rich and strayed from physics. Through the collapse of old Russia, through the coming to the new land, and through the Silicon Valley Gold Rush, I stayed. I was either lazy, or drawn to the impractical. And I too was rewarded.

I enjoyed studying abstract concepts and hard to reach objects. At times, I was fascinated by the ability of a small group of people to build, launch into space and operate a telescope that looks at objects in the Universe thousands of light years away from Earth. I had a chance to look at a black hole and see what was happening to this black hole several thousand years ago. It was a special experience and it resulted in this work, which is my very humble contribution to humanity's quest for discovery.

I wish to thank my adviser, Elliott Bloom, for giving me an opportunity to work on a unique astrophysics space project and for delegating to me a lot of responsibility. Great



thanks for his engaging interest in physics, encouragement and for his help with this manuscript.

This work stems from the combined effort of our collaboration. I express my thanks to my colleagues and friends at Stanford Linear Accelerator Center in California and Naval Research Laboratory in Washington, DC. I would like to thank all to follow (in no particular order) for their involvement with USA experiment, for their help, physics and life discussions that we had, advice that I received, the jokes exchanged and memorable time spent together on and off work: Gary Godfrey, Warren Focke, John Broeder, Pablo Saz Parkinson, Jim Ampe, Michael Wolff, Elliott Bloom, Chris Chaput, Kent Wood, Kaice Reilly, Michael Lovellette, Daryl Yentis, Cara Golembiewski, Gil Fritz, Mike Kowalski, James Beall, Paul Hertz, Paul Ray, Paul Kunz, Lynn Cominsky, Berrie Giebels, Terry Crandall, Takanobu Handa, Eduardo do Couto e Silva, Mark Yashar, Han Wen, Jeff Scargle, Andy Reid, Michael Hicks, Chris Hall, Linda Lee Evans, Mallory Roberts, Fatin Bulos, Allen Odian and Andrew Lee. Folks at NRL get additional thanks for their hospitality during my many stays in Washington. In particular, I would like to thank Gary Godfrey for his patience and tremendous help with every aspect of my work; Pablo Saz-Parkinson for his work on on-ground calibration data; Jim Ampe for sharing my passion for USA electronics and spending hours and hours of time running tests and explaining to me how it works; Michael Wolff for our work on planning the science program for thermal vacuum tests, it was always a pleasure to work with Michael; Warren Focke for many X-ray astrophysics discussions, during which I tested his patience and found that it goes far, and for his encouragement and help with editing of my thesis; Chris Chaput for his emotional support and practical help and just for being a good friend; John Broeder for responding to all of my SOS signals and for setting an example of real quality work; Chris Hall for helping to arrange my defense and for his choice of a chocolate cake; Berrie Giebels for his European sense of humor and going-away present, Linda Lee Evans for her female company and astrological predictions (they have not come true so far, except that I will be broke after graduate school).

I would like to pay a tribute to late Terry Crandall who made a tremendous contribution to the USA experiment as our computer genius. His inquiring mind, his humor and his eagerness to help will stay in my memory.

I deeply thank my high-school physics teacher Galina Sergeevna for teaching me most of the physics I know.

I wish to thank my fellow physics students from Stanford University: Darwin Serkland for his ingenious advice and for introducing me to American ways; Dana Lehr for her generous help at the times of need, I cannot thank her enough for the discussions that largely fueled the theory part of this thesis; Mallory Roberts for answering any possible physics question I had at any possible time of the day or night, and intriguing discussions we had outside of work. Special thanks go to Marcia Keating who oversaw graduate student affairs in Physics Department for taking our well being personally and for always siding with students in disputes with the professors.

I would also like to thank my defense committee members – Tsuneyoshi Kamae, Peter Michelson and Robert Wagoner for evaluation of my lengthy work, and for providing useful comments and insights. I am grateful to Robert Wagoner for his help with theoretical interpretation of my results.

My years at Stanford will be best remembered due to special people with whom I shared some special moments. I owe my gratitude to Yulya B. - a superwoman and a great friend. I thank Gulya and Ilya for still waiting for me to return to Moscow; Denis and Tanya for late night dinners and teas and so much help – this space is too small to mention it all; Yulya S. for teaching me how to live in the moment and for bringing lots of joy into my life; Katya for her out-of-space personality that I admire and for the shared fun habitat; Ivan for his crazy black hole theories and unmatched parties; Joseph for the passion; Philipp for the intellectual exchange; and Kaice and Klejda for Californian experiences.

I want to thank Evgenia Pribilova and Anatoly Shabad – the best parents ever. I thank my father for creating an aura of suspense around physics, for bringing home the most interesting people, for dragging me to physics conferences with him and for stacking the apartment with books on physics and math. I thank my mother for kindly balancing his sincere effort to make a physicist out of me. I thank my brother Georgii for our many youthful adventures that prevented me from becoming a nerd.

I thank Yuri the most for his help, his love and generosity.

# TABLE OF CONTENTS

<b>Abstract.....</b>	<b>v</b>
<b>Acknowledgments.....</b>	<b>viii</b>
<b>List of Tables.....</b>	<b>xvi</b>
<b>List of Figures.....</b>	<b>xviii</b>
<b>1 Introduction .....</b>	<b>1</b>
1.1 Introduction and History .....	1
1.2 Scope of Work.....	3
<b>2 Black Hole Binary Stars .....</b>	<b>5</b>
2.1 The Nature of Black Hole Binaries .....	5
2.2 Accretion .....	8
2.3 Spectral States .....	12
2.4 Disk Accretion Models.....	14
2.5 High-Frequency QPOs in BHC Binaries .....	17
2.6 High-Frequency QPO Models.....	19
2.6.1 Characteristic Disk Frequencies.....	19
2.6.2 Keplerian Motion Model.....	20
2.6.3 Diskoseismic Oscillations Model.....	21
2.6.4 Relativistic Precession Models.....	23
<b>3 Unconventional Stellar Aspect Experiment.....</b>	<b>26</b>

3.1 ARGOS Mission .....	26
3.2 Instrument Status.....	27
3.3 USA Instrument.....	27
<b>4 Data Analysis Techniques and Deadtime.....</b>	<b>32</b>
4.1 Fourier Transform .....	32
4.2 Deadtime Effects in General .....	33
4.2.1 Introduction .....	33
4.2.2 Change in the Incident Counting Rate .....	34
4.2.3 Change in the Original Statistics.....	35
<b>5 USA On-Ground Deadtime Calibration .....</b>	<b>39</b>
5.1 USA Deadtime Mechanisms .....	40
5.1.1 Deadtime Effects Introduced by the Detector Electronics .....	40
5.1.2 Deadtime Effects Introduced by the Detector Interface Board .....	53
5.1.3 Conclusions .....	59
5.2 USA Data Analysis Issues.....	61
5.2.1 Standard Data Modes .....	61
5.2.2 Timing Idiosyncrasies .....	64
5.2.3 Fourier Power Spectral Density Analysis of the On-Ground Calibration Data. ....	67
5.3 USA On-Ground Calibration Tests .....	68
5.3.1 Thermal Vacuum Tests .....	68
5.3.2 Description of the Data Used for the Analysis.....	71
5.4 USA On-Ground Calibration Results.....	71
5.4.1 Deadtime Model.....	71
5.4.2 Poisson Noise Power Spectrum Framework .....	80
5.4.3 Power Spectra of the Calibration Data.....	81
5.4.4 Comparison of the Power Spectra of the Data in Different Data Modes..	85
5.4.5 Power Spectra of the Simulated Data.....	85

5.4.6	Comparison of the Power Spectra of the Simulated Data With the Power Spectra of the Calibration Data.....	87
5.4.7	Recipe for the Deadtime Correction.....	97
5.5	Energy-Dependent Instrumental Effect.....	103
5.5.1	The Essence of the Effect.....	105
5.5.2	Procedure for the Deadtime Correction to Energy-Selected Power Spectra.....	110
5.6	Future Work .....	115
<b>6</b>	<b>Detection of High-Frequency Variability and Other Studies of Black Hole Transient XTE J1859+226.....</b>	<b>116</b>
6.1	X-ray Nova XTE J1859+226 .....	116
6.2	Light Curve of the Source .....	118
6.3	Observations and Data Analysis .....	119
6.4	High-Frequency Variability in XTE J1859+226.....	120
6.4.1	Power Spectra of XTE J1859+226.....	120
6.4.2	Power Spectra of Cas A .....	126
6.4.3	Power Spectra of Cygnus X-1 .....	127
6.5	Low-Frequency QPOs.....	130
6.6	Temporal Properties versus Photon Energy .....	132
6.7	Discussion .....	134
6.7.1	High-Frequency QPOs .....	134
6.7.2	Temporal Properties versus Photon Energy .....	140
<b>7</b>	<b>Summary.....</b>	<b>145</b>
	<b>Appendix .....</b>	<b>148</b>
A.1	Thermal Vacuum Tests Data Used for the Analysis .....	148
A.2	The Results of the Fits to the Power Spectra of the On-Ground Calibration Data.....	150
A.3	The Results of the Fits to the Power Spectra of the Simulated Data .....	152
A.4	List of XTE J1859+226 USA Fits Files .....	154

<b>References .....</b>	<b>156</b>
-------------------------	------------

## LIST OF TABLES

Table 2.1	Properties of the compact objects [81]. Solar mass $M_{\odot}=2\times 10^{33}$ g and the solar radius $R_{\odot}=7\times 10^{10}$ cm. ....	6
Table 2.2	List of all BHC transients with high-frequency QPOs. Fractional rms amplitudes could vary slightly for various observations. * Frequencies derived from the combined power spectra of 50 observations (Section 6.4.1). For XTE J1859+226, RXTE and USA data are taken during the same outburst.....	18
Table 5.1	Description of the USA science data modes. For the details refer to [104] and [28] .....	61
Table 5.2	Asymptotic maximum number of events one science frame can hold and break rates. The rates in the last column are approximate (rounded to the nearest 100) average rates over 100 simulations of a Poisson process. ....	62
Table 5.3	PSD parameters used for the calibration data analysis. ....	67
Table 5.4	Summary of the results of the deadtime model fit to the data. The DIB resync time for the data set marked with * is 63 $\mu$ s. For the rest of the data the DIB resync time is 40 $\mu$ s. Samples of 5 million data events (or as many as were available) and 50 million Monte Carlo events were used for each fit. ....	77



Table 5.5 Results of the straight line fit to the deadtime as a function of rate: $\tau = ar_{in} + b$ .....	80
Table 5.6 Results of the parabolic fit. $P_1 = ar_o^2 + br_o + c$ . 13 dof. ....	103
Table 5.7 Results of the parabolic fit. $P_2 = ar_o^2 + br_o + c$ . 13 dof. ....	103
Table 5.8 Channel to energy conversion for modes 1 and 2 [78]. The energy numbers (except the last one) are lower boundaries. Layer 1.....	106
Table 5.9 Results of the fit to the ground data with (5.12). ....	113
Table 5.10 Results of the fit to the ground data with (5.13). ....	115
Table 6.1 Results of the fit to the on-orbit data with (5.13). 1. XTE J1859+226 in a very high state. 305 degrees of freedom. 2. XTE J1859+226 in a high state. 304 dof. 3. Cas A. 304 dof. 4. Cygnus X-1. 302 dof. ....	122
Table 6.2 Results of the QPO fit with three Lorentzian functions and the power law. Power law $Af^\alpha$ parameters are: $A=1.6\pm1.7$ , $\alpha=-1.5\pm0.5$ . The $\chi^2$ for 23 degrees of freedom is 1.06. Energy range: 4.2-19.8 keV.....	126
Table 6.3 Results of the QPO fit. Sub-harmonic: $\chi^2/16=0.56$ . Fundamental: $\chi^2/33=1.17$ . First harmonic: $\chi^2/69=0.93$ . Energy range: 1.1-19.8 keV..	132

## LIST OF FIGURES

Figure 2.1	Diagram of the two-component advective flow model courtesy Chakrabarti & Titarchuk [7]. The components of the model are described in the text.....	16
Figure 3.1	The Advanced Research and Global Observation Satellite (ARGOS).....	27
Figure 3.2	USA detector front and side view.....	28
Figure 3.3	Detailed view of one USA detector unit.....	29
Figure 3.4	USA proportional chamber.....	29
Figure 3.5	USA effective area for one detector unit and two wire layers as a function of photon energy. ....	30
Figure 4.1	Binned time interval density, $F(t)$ , for a Poisson process affected by non-extended deadtime. Bin size: 2 $\mu$ s. The curve results from a simulation of one million Monte Carlo events with $r_o=4100$ Hz counting rate and deadtime $\tau=16.4$ $\mu$ s. The simulation parameters are relevant to the discussions of Section 5.4. The distribution is shifted from zero by the value of the deadtime.....	37
Figure 4.2	Leahy normalized power spectrum of a Poisson process with non-extended deadtime. The curve results from a simulation of one million Monte Carlo events with $r_o=4100$ Hz counting rate and a deadtime	

	$\tau=16.4 \mu\text{s}$ . The simulation parameters are relevant to the discussions of Section 5.4. The time series bin size is $2 \mu\text{s}$ . The segment length is $T=0.26 \text{ s}$ . The plot is an average of 930 PSDs. The power spectrum is logarithmically binned. The dashed line is the Leahy normalized power spectrum for a Poisson process without deadtime. ....	38
Figure 5.1	Diagram of the USA event timing flow. Currently only detector 0 is functioning in orbit. ....	40
Figure 5.2	Diagram of the USA detector electronics. ....	42
Figure 5.3	Width of the one-shot pulse as a function of the distance between incoming pulses. ....	45
Figure 5.4	Amplifier input and output. Horizontal time scale is $2 \mu\text{s}$ per division (10 divisions total). Value per division for each channel for the vertical voltage scale is indicated under the plot (8 divisions total). Channel 1: input pulse. Channel 4: pulse out of the amplifier. The amplifier is not saturated. ....	47
Figure 5.5	Amplifier input and output. Horizontal time scale is $2 \mu\text{s}$ per division (10 divisions total). Value per division for each channel for the vertical voltage scale is indicated under the plot. Channel 1: input pulse. Channel 4: pulse out of the amplifier. The amplifier is saturated. ....	48
Figure 5.6	Amplifier output. The large signal out of the amplifier is followed by the nominal signal. ....	49
Figure 5.7	Amplifier output. Horizontal time scale is $5 \mu\text{s}$ per division (10 divisions total). Vertical voltage scale is $500 \text{ mV}$ per division (8 divisions total). The negative tails of the output pulses are shown. Five waveforms correspond to five different input voltages. From top to bottom: input voltage is $300 \text{ mV}$ (the amplifier reaches the saturation threshold at this input voltage); input voltage is 3 times the saturation threshold input voltage; 6 times; 10 times; and 30 times. Average of 64 acquisitions. ....	49

Figure 5.8	Amplifier output. Horizontal time scale is 50 $\mu$ s per division (10 divisions total). Vertical voltage scale is 100 mV per division (8 divisions total). The negative tails of the output pulses are shown. Five waveforms correspond to five different input voltages. From top to bottom: input voltage is 300 mV (the amplifier reaches the saturation threshold at this input voltage); input voltage is 3 times the saturation threshold input voltage; 6 times; 10 times; and 30 times. Average of 64 acquisitions.....	50
Figure 5.9	One-shot output. Horizontal time scale is 20 $\mu$ s per division (10 divisions total). Value per division for each channel for the vertical voltage scale is indicated under the plots. Channel 1: large 3 V pulse into the amplifier (10 times input value that saturates the amplifier). Channel 2: small 10 mV pulse into the amplifier. Channel 4: one-shot stretching indicator. .	51
Figure 5.10	Amplifier output. Horizontal time scale is 50 ms per division (10 divisions total). Vertical voltage scale is 100 mV per division (8 divisions total). Negative tail of the output pulse with noise. The input voltage is 10 times the saturation threshold input voltage. Single acquisition. ....	53
Figure 5.11	Diagram of the DIB event processing. Currently only detector 0 is functioning in orbit.....	55
Figure 5.12	Timing profiles of pulse height and timing interrupts. ....	58
Figure 5.13	Average number of events held in one frame versus observed counting rate for a Poisson event distribution with non-extended deadtime. Each data point is an average of 100 simulations. Low-bit rate modes. ....	63
Figure 5.14	Average number of events held in one frame versus observed counting rate for a Poisson event distribution with non-extended deadtime. Each data point is an average of 100 simulations. High-bit rate modes. ....	64

- Figure 5.15 Observed counting rate from the X-ray source as a function of yaw angle. Curve on the left corresponds to the rates observed in the detector 1 and on the right in the detector 0..... 70
- Figure 5.16 The deadtime model fit to the time interval distribution. a) Histogram of the time interval distribution of the detector 0, mode 3 data (5 million events). Crosses represent the model (50 million events). Deadtime  $\tau=16.368 \mu\text{s}$ , bin size:  $t_b=2 \mu\text{s}$ ,  $r_o=4075 \text{ Hz}$ .  $\chi^2=1.707$  (dof=494). The  $0^{th}$  bin contains the same time events. b) Difference between the data and the model. Range up to  $200 \mu\text{s}$  is shown as the most interesting. There are no deviations of the model from the data beyond this range. .... 74
- Figure 5.17 The deadtime model fit to the time interval distribution. a) Histogram of the time interval distribution of the detector 1, mode 4 data (2 million events). Crosses represent the model (50 million events). Deadtime:  $\tau=16.51 \mu\text{s}$ , bin size:  $t_b=2 \mu\text{s}$ ,  $r_o=1035 \text{ Hz}$ .  $\chi^2=0.979$  (dof=493). The  $0^{th}$  bin contains same time events. b) Difference between the data and the model. Range up to  $200 \mu\text{s}$  is shown as the most interesting. There are no deviations of the model from the data beyond this range. .... 75
- Figure 5.18 Deadtime as a function of the incident rate. Detector 0 and detector 1 are marked with triangles and dots, respectively. The dashed lines show the best constant fit.  $\chi^2=3.870$  for detector 0 (dof=4).  $\chi^2=2.104$  for detector 1 (dof=5)..... 78
- Figure 5.19 Deadtime as a function of the incident rate. Detector 0 and detector 1 are marked with triangles and dots, respectively. The dashed lines show the best linear fit.  $\chi^2=0.573$  for detector 0 (dof=3).  $\chi^2=1.388$  for detector 1 (dof=4)..... 79
- Figure 5.20 a) Power spectrum of the mode 3, detector 0 data fitted with (5.2).  $r_o=4075 \text{ Hz}$ ,  $t_b=96 \mu\text{s}$ . Total exposure time: 21.8 ks. Fitting range:

	0-5000 Hz. Solid line: fit. b) Difference between the power spectrum of the data and the fit function.....	83
Figure 5.21	a) Power spectrum of the mode 3, detector 1 data fitted with (5.2). $r_o=3035$ Hz, $t_b=96$ $\mu$ s. Total exposure time: 17.9 ks. Fitting range: 0-5000 Hz. Solid line: fit. b) Difference between the power spectrum of the data and the fit function.....	84
Figure 5.22	a) Power spectrum of the simulated data fitted with (5.2). Parameters of the model: $r_o=4075$ Hz, $\tau_0=16.383$ $\mu$ s. $t_b=96$ $\mu$ s. Total exposure time: 49.0 ks. Fitting range: 0-5000 Hz. Solid line: fit. b) Difference between the power spectrum of the simulated data and the fit function. ....	86
Figure 5.23	a) Power spectrum of the mode 3, detector 0 data. $r_o=4075$ Hz, $t_b=96$ $\mu$ s. Total exposure time: 21.8 ks. b) Difference between the power spectra of the calibration data and the simulated data. Parameters of the model: $r_o=4075$ Hz, $\tau_0=16.383$ $\mu$ s. $t_b=96$ $\mu$ s. Total exposure time: 49.0 ks. Solid line: function (5.3).....	88
Figure 5.24	a) Power spectrum of the mode 3, detector 1 data. $r_o=3035$ Hz, $t_b=96$ $\mu$ s. Total exposure time: 17.9 ks. b) Difference between the power spectra of the calibration data and the simulated data. Parameters of the model: $r_o=3035$ Hz, $\tau_0=16.383$ $\mu$ s. $t_b=96$ $\mu$ s. Total exposure time: 65.9 ks. Solid line: function (5.3).....	89
Figure 5.25	$P_1$ and $P_2$ coefficients describing fit to the calibration data. $t_b=32$ $\mu$ s. Points marked with triangles correspond to detector 0 and with dots to detector 1. The error bars are omitted, since they are smaller than the size of the data points.....	91
Figure 5.26	a) $P_1 - P_1^{extended}$ coefficients. b) $P_2 - P_2^{extended}$ coefficients. $t_b=32$ $\mu$ s. Points with error bars correspond to the calibration data, crosses to the model, dots to the non-extended deadtime, and triangles to the extended	

deadtime (obviously, triangles form zero baseline). Data at low rates was collected from detector 1 and at high rates from detector 0 (see Table A.1). For all the points, except the ones corresponding to calibration data, the error bars are omitted, since they are smaller than the size of the data points. ....	93
Figure 5.27 a) $\Delta P_1 = P_1^{sd} - P_1^d$ . b) $\Delta P_2 = P_2^{sd} - P_2^d$ . $r_o=4075$ Hz. Detector 0 data. ....	94
Figure 5.28 a) $\Delta P_1 = P_1^{sd} - P_1^d$ . b) $\Delta P_2 = P_2^{sd} - P_2^d$ . $r_o=3035$ Hz. Detector 1 data. ....	95
Figure 5.29 a) Parabolic fit to the coefficients $P_1$ for the simulated data. The error bars are omitted, since they are smaller than the size of the data points. b) Residuals of the fit. $t_b=96$ $\mu$ s. The deadtime used in the simulation at all rates is the detector 0 deadtime. ....	100
Figure 5.30 a) Parabolic fit to the coefficients $P_2$ for the simulated data. The error bars are omitted, since they are smaller than the size of the data points. b) Residuals of the fit. $t_b=96$ $\mu$ s. The deadtime used in the simulation at all rates is the detector 0 deadtime. ....	102
Figure 5.31 a) $P_1 - P_1^{extended}$ coefficients. Points with error bars correspond to the simulated data. b) $P_2 - P_2^{extended}$ coefficients. $t_b=96$ $\mu$ s. The deadtime used in the simulation at all rates is the detector 0 deadtime. ....	104
Figure 5.32 Power spectrum of the mode 2, detector 0, channel 6 ground data. $r_o=523$ Hz. $t_b=96$ $\mu$ s. Total exposure time 0.7 ks. Dashed line represents expected power spectrum without the energy-dependent instrumental effect present. ....	107
Figure 5.33 ACF. The data set is the same as in Figure 5.32. $r_o=523$ Hz. $t_l=96$ $\mu$ s. $N_\gamma = 2 \cdot 10^5$ . First bin with $ACF=N_\gamma$ is omitted. Dashed line represents ACF function calculated for a Poisson process with parameters of the	

	data set. Beyond the shown time range, the data does not deviate from Poisson. ....	108
Figure 5.34	Power spectrum of the mode 2, detector 0, channel 4 ground data. $r_o=394$ Hz. $t_b=96$ $\mu$ s. Total exposure time 0.7 ks. Dashed line represents expected power spectrum without the energy-dependent instrumental effect present. ....	110
Figure 5.35	Power spectrum of the mode 2, detector 0, channel 6 ground data fitted with (5.12). $r_o=523$ Hz. $t_b=96$ $\mu$ s. Total exposure time 0.7 ks. Fitting range: 0-5000 Hz. Solid line: fit. Dashed line: $bP^{other}(f)$ . ....	112
Figure 5.36	Same as in Figure 5.35, but zoomed into the lower frequency region. ....	113
Figure 5.37	Residuals of the fit to the power spectrum with (5.13). Same data set as in Figure 5.35. Fitting range: 300-5000 Hz. The residuals are consistent with zero in $\sim$ 30-5000 Hz region. ....	114
Figure 6.1	The 2-12 keV daily averaged ASM light curve of XTE J1859+226 during the outburst. Modified Julian Date 51450 corresponds to September 29, 1999. ....	118
Figure 6.2	Noise-subtracted power spectrum of the mode 1 XTE J1859+226 data. Energy range: 4.2-19.8 keV. Very high state. $r_o=465$ Hz. $t_b=96$ $\mu$ s. Total exposure time 13.4 ks. Range used to determine the noise: 300-5000 Hz. Range used to calculate rms amplitude: 40-300 Hz. ....	121
Figure 6.3	Power spectra of XTE J1859+226 RXTE data in two energy bands courtesy Cui et al. [15]. The solid lines represent the best-fit model to the data. The QPO frequency in the hard band is $187^{+14}_{-11}$ Hz. The power spectra are not corrected for deadtime. ....	123
Figure 6.4	Noise-subtracted power spectrum fitted with the three Lorentzian functions and the power law. Same data set as in Figure 6.2. Fitting range: 5-500 Hz. Solid line is a fit. Dashed line is a power law only. ....	124



- Figure 6.5 Noise-subtracted power spectrum of the mode 1 XTE J1859+226 data. Energy range: 4.2-19.8 keV. High state.  $r_o=274$  Hz.  $t_b=96$   $\mu$ s. Total exposure time 6.6 ks. Range used to determine the noise: 300-5000 Hz. High-frequency variability is weaker or absent in the high state. The dotted line shows how the signal with the same rms amplitude as in the very high state would have looked like..... 125
- Figure 6.6 Power spectrum of the mode 1, channel 2 Cas A data fitted with (5.13).  $r_o=106$  Hz.  $t_b=96$   $\mu$ s. Total exposure time 22.7 ks. Fitting range: 300-5000 Hz. Dashed line is  $bP^{other}(f)$  (5.10)..... 127
- Figure 6.7 Residuals of the fit to the Cas A power spectrum with (5.13). Same data set as in Figure 6.6. Fitting range: 300-5000 Hz. The residuals are consistent with zero in  $\sim 0$ -5000 Hz region. .... 128
- Figure 6.8 Noise-subtracted power spectrum of the mode 1 Cygnus X-1 data. Energy range: 4.2-19.8 keV.  $r_o=377$  Hz.  $t_b=96$   $\mu$ s. Total exposure time 23.6 ks. Range used to determine the noise: 320-5000 Hz. Solid line is a power law with index  $-1.53$ . .... 129
- Figure 6.9 Power spectrum of the mode 2 XTE J1859+226 data. Energy range: 1.1-19.8 keV.  $r_o=1049$  Hz.  $t_b=960$   $\mu$ s. Total exposure time 0.3 ks. The power due to the noise, corrected for the deadtime is shown in a dashed line (the energy dependent instrumental effect is ignored, since it is insignificant on the shown y-scale)..... 131
- Figure 6.10 Fractional rms amplitudes as a function of energy. Clockwise from upper left: Fundamental frequency QPO, range 4.4-5.5 Hz. Low-frequency noise component, range 0.1-1 Hz. Sub-harmonic, range 2.3-2.9 Hz. First harmonic, range 9.5-10.3 Hz..... 133
- Figure 6.11 Parameter space for the mass and spin of a black hole courtesy Cui et al. [12]. Top: GRO J1655-40. Bottom: GRS 1915+105. The solid line shows the spectroscopic results of Zhang et al. [107], with the shaded

region indicating the estimated uncertainty [12]. Two lines corresponding to precession model of Cui et al. (gravitomagnetic precession) were computed for the precession at the marginally stable orbit (upper curve) and at the radius where the integrated flux peaks (lower curve). The shaded area for the measured mass represents the confidence region. The mass of GRS 1915+105 is not known..... 135

Figure 6.12 PBV correlation. The frequency of low-frequency QPO versus the frequency of the high-frequency QPO detected during the same observation. Diamonds: GRO J1655-40. Circles: XTE J1550-564. Squares: XTE J1859+226. See references in Table 2.2 for the source of data points. The lines are  $2\nu_{nod}$  versus  $\nu_{per}$  in the weak field and slow rotation approximation. Doted line:  $m=3.5$ . Solid line:  $m=7$ . Dashed line:  $m=14$ . Three groups of lines correspond to different angular momentum parameter  $a$  . ..... 139

Figure 6.13 Energy dependence of a QPO in GRS 1915+105 on 1996 May 05. Plot is provided by Lehr [38]. Result of Monte Carlo simulations. Solid line: ratio of spectrum from photons injected at  $7.5-8.5M$  to total disk spectrum. Dashed: same ratio for photons injected at  $9-10M$  . Dotted: same ratio for photons injected at  $11-12M$  . Normalized by  $rdr$  . ..... 143

# CHAPTER 1: INTRODUCTION

## 1.1 Introduction and History

Studies of high-frequency variability in X-ray binaries provide a unique opportunity to explore the fundamental physics of spacetime and matter. The dynamical timescale on the order of several milliseconds is a timescale of the motion of matter through the region located in close proximity to a compact object. For example, the orbital timescale of  $\sim 1$  millisecond (1000 Hz) corresponds to a 32 km distance from a  $10 M_{\odot}$  black hole. Thus, theories of the physics of the inner accretion disk, the orbital motion of matter in relativistic gravity and relativistic disk oscillations can be probed by studying high-frequency signals from black hole candidate binaries (BHC).

A number of theoretical predictions of the millisecond variability in X-ray binaries were made in 1970s and 1980s (reviewed by van der Klis [98]). During those two decades millisecond variability from a BHC Cygnus X-1 had been reported twice. Rothschild et al. in 1974 [76] reported millisecond bursts in Cygnus X-1 data from a rocket X-ray experiment. However, these results were based on a wrong assumption [66] [101] of a constant Poisson expectation of the number of counts in the light curve. No model-independent variability in the time domain was found in independent studies [43]. Meekins et al. [49] in 1984 reported detection of a strong variability in Cygnus X-1 in the 3-10 millisecond region ( $\sim 100$ -300 Hz in a frequency domain). The data came from the

High Energy Astrophysical Observatory (HEAO A-1) experiment. Chaput et al. [8] proved the result wrong showing that the detected variability resulted from a HEAO A-1 instrumental effect.

With the launch of the microsecond timing resolution Rossi X-Ray Timing Explorer (RXTE, [4]) in 1995, a variety of millisecond phenomena in neutron star binaries emerged. The broad-band noise components and quasi-periodic oscillations (QPOs) in these objects now cover the frequency range up to  $\sim 2$  kHz. Three different millisecond phenomena were discovered by RXTE in low-magnetic-field neutron stars: the accreting millisecond pulsar, burst oscillations, and kilohertz QPOs [98]. In addition, significant broad-band noise components up to 1 kHz were observed for several neutron star binaries [87].

However, the evidence for high-frequency signals in BHC binaries is scarce and is just emerging. Recent studies with RXTE data of BHC binaries in the low state showed that the broad-band noise power rapidly decreases above 10-50 Hz and becomes one-two orders of magnitude lower than for neutron stars above the same frequencies [87]. Statistically significant broad-band noise variability above 50 Hz was reported this year for only one BHC binary source - Cygnus X-1 [31], [74]. The variability in both spectral states of Cygnus X-1 extends up to  $\sim 50$ -300 Hz with a fractional rms amplitude above 100 Hz at the level of  $\sim 2$ -3% [74], which is much smaller than in the neutron stars [87]. However, much of this power is likely to be the result of the “low-frequency leakage” in the power spectrum [18], [97] for which no correction was made.

A new high-frequency phenomenon was discovered within the past three years in the BHC transients. QPOs in the frequency range  $\sim 100$ -300 Hz were found in four sources: GRO J1655-40, XTE J1550-564, 4U 11630-47, and XTE J1859+226 (see Table 2.2 and references therein). These reported QPO signals were small with fractional rms amplitudes of several percent. The 67 Hz QPO in GRS 1915+105 [15] is usually discussed together with these QPO, although it is not clear if they are related. All the signals were detected with RXTE. In this thesis we report the observation of the QPOs in

XTE J1859+226 with USA. USA is the only instrument, besides RXTE, to confirm high-frequency QPOs in a BHC transient. A number of theories have been proposed to explain high-frequency QPOs in black-hole transients (Section 2.6). But very little is known so far about this new phenomenon. More observations of BHC transients by microsecond timing resolution experiments to provide richer phenomenology of high-frequency QPOs are needed.

## **1.2 Scope of Work**

The essence of this work is the detection of high-frequency variability (40-300 Hz) in a BHC transient XTE J1859+226 with the USA experiment.

The detection of high-frequency variability in X-ray binaries depends on how well we understand the level of Poisson noise due to the photon counting statistics, which, in turn, depends on how well we can understand and model the detector's deadtime and other systematic effects. A large body of this thesis describes the long road to this detection: experimental timing calibration work on the USA detector, the development of deadtime models, deadtime correction methods, and the development of correction techniques to account for instrumental imperfections.

Chapter 2 provides the theoretical background on the physics of X-ray binary BHC systems relevant to the discussion of the theories behind high-frequency variability. It describes the nature of BHC binaries, accretion mechanisms, spectral states and accretion disk models. We talk in detail about observational high-frequency phenomena in BHC binaries, and the theories that attempt to explain it.

Chapter 3 describes the USA experiment: the detector and the ARGOS mission. Chapter 4 describes the data analysis techniques and provides the general discussion on the subject of deadtime and how the deadtime affects observational data.

Chapter 5 is dedicated to the USA on-ground calibration work, which was carried out before launch to understand the detectors' deadtime and other instrumental effects. It

contains the description and results of USA preflight thermal vacuum tests, issues in USA timing, the deadtime model, and methods for correcting deadtime and instrumental imperfections.

In Chapter 6 we report a  $20\sigma$  detection of a signal in the power spectrum of XTE J1859+226 in the 40-300 Hz frequency range. To verify our understanding of the instrumental noise, we test the deadtime correction method on power spectra of Cas A – a Poisson source, and Cygnus X-1 – a well studied BHC binary. In this chapter we also investigate temporal properties of the source as a function of photon energies. At the end we discuss the high-frequency variability results in the context of Keplerian, diskoseismic and relativistic precession models. We also discuss the dependence of the rms amplitude of low-frequency power spectrum components on energy within several models.

Chapter 7 is the summary of this work.

## CHAPTER 2: BLACK HOLE BINARY STARS

### 2.1 The Nature of Black Hole Binaries

An X-ray binary system contains a compact star accreting material from a companion star. With few exceptions, X-ray binaries have companions with masses either  $\lesssim 1 M_{\odot}$  or  $\gtrsim 10 M_{\odot}$ . These two classes of binaries are called low-mass X-ray binaries (LMXBs) and high-mass X-ray binaries (HMXBs). It is generally believed that three types of compact objects exist in nature. The compact objects are formed when a star exhausts its nuclear fuel, and the loss of the outward thermal pressure leads to gravitational collapse. The remains of the collapsed star can form a white dwarf, a neutron star or a black hole.

A white dwarf is a hot compact object, for which the inward gravitational pull is balanced with the outward Fermi electron-degeneracy pressure. The typical properties of compact objects are listed in Table 2.1. The mass of the white dwarf is always less than the Chandrasekhar limit  $M_{ch} = 1.4 M_{\odot}$ .

If the matter is compressed further than the characteristic density of a white dwarf, the free electrons are forced to combine with protons to form neutrons (inverse beta-decay). The self-gravitating mass of neutrons is a neutron star. The neutron star equilibrium is

Object	Mass (M)	Radius (R)	Mean Density
White dwarf	$\lesssim M_{\odot}$	$\sim 10^{-2} R_{\odot}$	$\lesssim 10^7$
Neutron star	$\sim 1-3 M_{\odot}$	$\sim 10^{-5} R_{\odot}$	$\lesssim 10^{15}$
Black hole	arbitrary	$2GM/c^2$	$\sim M/R^3$

Table 2.1 Properties of the compact objects [81]. Solar mass  $M_{\odot} = 2 \times 10^{33}$  g and the solar radius  $R_{\odot} = 7 \times 10^{10}$  cm.

supported generally by the Fermi pressure of the degenerate neutrons. The equation of state for the neutron stars is incomplete, thus there is no certain upper limit on the neutron star mass. The neutron star mass upper limit depends on the assumptions about the constraints on the possible equations of state. Currently, the popular upper limit to the mass of the neutron star is the Rhoades & Ruffini limit [75] of  $\sim 3 M_{\odot}$ .

If the core mass is too large to form a neutron star, it is generally believed that the core continues to collapse into a gravitational singularity called a black hole. Predicted by general relativity and the neutron star equation of state, a black hole is a region of spacetime, from where nothing can escape to the outside world, not even light. The mean density for a  $3 M_{\odot}$  black hole is  $\sim 10^{16} \text{ g/cm}^3$ , and smaller for larger masses. (Nuclear density is  $\sim 10^{14} \text{ g/cm}^3$ .)

There is a theoretical class of compact objects, named Q-stars, that allow for masses exceeding the Rhoades-Ruffini mass limit for neutron stars without requiring collapse to a black hole (for an overview of Q-stars see Bloom [3]). A Q-star is an N-body system of nucleons and electrons that does not need gravity to be stable. In such a system the stable new phase of bulk nuclear matter dominates the gravitational attraction, and the hadronic forces largely provide for the stability of the star independent of gravity. The mass limit for a Q-star is  $890 M_{\odot}$ , resulting from the low density of a high-mass Q-star compared to a conventional neutron star. This large mass limit allows that stellar mass black holes do not exist.



A stationary black hole is characterized by only three independent observable quantities [6]: the mass  $M$ , angular momentum  $J$  and charge  $Q$ . The gravitational field in a simple case of a spherical, non-rotating and electrically neutral black hole is described by the Schwarzschild metric [88], [81]

$$ds^2 = -(1 - 2M/r)dt^2 + (1 - 2M/r)^{-1}dr^2 + r^2d\Omega^2, \quad (2.1)$$

where a two-dimensional spherical surface has a proper circumference  $2\pi r$ . The geometrized units  $c = G = 1$  are used. The boundary of a region of spacetime that cannot communicate with the outside world is called the event horizon or the surface of the black hole. It lies at the Schwarzschild radius  $r_s = 2M \cong 3m$  [km], where  $m = M/M_\odot$ .

For a test particle with nonzero rest mass orbiting a Schwarzschild black hole, the effective potential depends on a black hole mass  $M$  and test particle angular momentum per unit mass  $L$ . The local minima in the effective potential correspond to the radii of stable orbits. Such orbits exist only for  $L > 2\sqrt{3}M$ . The innermost or marginally stable circular orbit occurs at  $r_{ms} = 3r_s = 6M \cong 9m$  [km] for the particle with a marginally bound angular momentum per unit mass of  $2\sqrt{3}M$ .

For rotating black holes the effective potential and radius of the innermost stable orbit depend on the angular momentum  $J$  of the black hole. The rotating electrically neutral black hole is described by the Kerr metric [34], [81]. The angular momentum of a Kerr black hole is characterized by the dimensionless angular momentum parameter  $a = cJ/(GM^2)$  where  $-1 \leq a \leq 1$ . (Thorne [92] estimates that in the presence of an accretion disk,  $a$  takes values in the range from  $-0.998$  to  $0.998$ .) The parameter is positive for the corotating or prograde orbits, where test particle and the black hole angular momenta are parallel and negative for the counterrotating or retrograde orbits. It is zero for non-rotating (Schwarzschild) black hole. The radius of a marginally stable circular orbit for the Kerr metric in Boyer-Lindquist coordinates [5] is given by [81]

$$\begin{aligned}
r_{ms} &= M(3 + Z_2 \mp [(3 - Z_1)(3 + Z_1 + 2Z_2)]^{1/2}), \\
Z_1 &= 1 + (1 - a^2)^{1/3} [(1 + a)^{1/3} + (1 - a)^{1/3}] \\
Z_2 &= (3a^2 + Z_1^2)^{1/2}.
\end{aligned} \tag{2.2}$$

The upper sign corresponds to prograde orbits, and lower to retrograde orbits. For a non-rotating Kerr black hole with  $a=0$  (Schwarzschild black hole)  $r_{ms} = 6M \cong 9m$  [km] and the event horizon lies at  $2M \cong 3m$ . For the maximally rotating Kerr black hole ( $a=1$ ), the event horizon lies at  $M \cong 1.5m$  [km]. For the prograde orbits and maximum rotation,  $r_{ms} = M \cong 1.5m$  [km]. For the retrograde orbits and maximum rotation,  $r_{ms} = 9M \cong 13.5m$  [km].

## 2.2 Accretion

Accretion is a process by which a compact star in a binary system captures matter from the companion star. As matter falls towards a compact star, the gravitational potential energy is converted into electromagnetic radiation, making the binary system visible in X-rays. In general, the modeling of a gas accretion flow into compact object and of the properties of the emitted radiation is a difficult problem. One must consider dynamical equations that would have to describe hydrodynamic flow of gas in the presence of magnetic field (in the case of white dwarfs and neutron stars), geometry of the flow, relativistic effects, radiation transfer and boundary conditions both at large distances, where the gas joins the accreting mass, and close to the compact star. It is no surprise that the accretion problem has been only solved for a few idealized cases. Below, we will consider accretion onto black holes, which is characterized by the absence of the magnetic field from the black hole (but not from the disk) and the presence of the event horizon.

There are two major modes of the matter transfer from a companion star to a black hole: through stellar wind or through Roche lobe overflow. The spectral type of the companion star determines the mode.

Large young stars have a substantial stellar wind. The wind is an outflow of plasma or gas accelerated by radiation pressure. In HMXBs the companion is an O or B star with optical and UV luminosity on the order or greater than that of the accretion disk around the compact star [10], [65]. The OB star companion has a substantial stellar wind that removes between  $10^{-4} M_{\odot}$  and  $10^{-10} M_{\odot}$  in a year with a velocity of 1000-2000 km/s [102], [35]. The fraction of the wind captured by a black hole in a relatively close orbit can supply enough material to power the X-ray source. Even if the Roche lobe of the system is full, wind may contribute a significant component to the overall accretion.

In LMXBs, the companion is an old star (later than type A) or a white dwarf. This type of star does not have strong enough wind to power X-ray emission. The mass transfer in this case can occur only when the companion fills its critical gravitational potential lobe (Roche lobe). The transfer through the Roche lobe overflow happens if the companion star expands in radius beyond the Roche lobe or if the distance between binary's stars shrinks due to the loss of angular momentum. Once the Roche lobe is filled in either scenario, the companion star will lose its material. The matter stream flows over the inner Lagrangian point between two stars forming an accretion disk around the compact object.

The geometry of the accretion flow can be spherical or the flow can form a disk. The geometry is determined by the angular momentum per specific mass of the flow [35].

The specific angular momentum of the material captured from a stellar wind is determined by the gradients and asymmetries in the wind [80]. The magnitude of the captured angular momentum from a stellar wind is usually too small to form a disk [17], and the resulting geometry of accretion is spherical (spherically symmetric accretion flow). The accretion is highly inefficient, since mass leaves the star in all directions, not just towards the compact object, and only the fraction of the wind passing close to the compact object is accreted. If the specific angular momentum is higher, a disk can form in the wind-fed binary. Numerical simulations showed that if the disk forms, it may change its direction of rotation [1], [46]. The changes in rotation together with the effects

of a Kerr black hole on the inner edge of the accretion disk are proposed as a cause for the spectral state transitions of BHC binary Cygnus X-1 [107]. We will focus on disk accretion, since the BHC transient sources are believed to be LMXBs [90].

Accreting matter forms a disk when its specific angular momentum is too large for it to descend on the accreting object directly. The accretion via Roche lobe overflow in black hole binaries satisfies this condition and always results in disk formation. The infalling matter occupies successively closer circular orbits in the equatorial plane of the compact object. For the matter to spiral in, angular momentum must be transferred out of the system. The angular momentum is transferred to the outer layers through viscous interactions. The outer radius of the disk is limited by the tidal forces that transfer angular momentum back to the companion orbit. The inner edge of the accretion disk around a black hole cannot be closer than the innermost stable orbit. During the angular momentum transfer in the disk, the gravitational energy is released as heat. The radiatively efficient geometrically thin disk radiates the released energy perpendicular to the plane of the disk. The estimates of the viscosity needed to transfer sufficient angular momentum and dissipate sufficient energy in a disk at orbital equilibrium are higher than the molecular viscosity in plasma. Some additional mechanisms must be at work, and, as of today, the physics of the transport of the angular momentum is not well understood. Recent studies by Hawley et al. [27] showed that the transport of the angular momentum may be explained as resulting from the generation of turbulence by a magnetorotational instability in accretion disk.

The efficiency,  $\varepsilon$ , of the process that converts accreting matter to radiation is

$$\varepsilon = L / \dot{M} c^2, \quad (2.3)$$

where  $L$  is the luminosity, observed at a distance and  $\dot{M}$  is the rest mass accretion rate [81]. In the case of disk accretion, the total energy radiated by the matter as it drifts towards the inner edge of the disk is the gravitational binding energy of the matter at the innermost stable orbit (assuming the energy radiated later as the mass falls from the edge

to the event horizon is negligible). The efficiency for the non-rotating black hole is 5.7% and 42% for a maximally rotating black hole and prograde disk [81]. In comparison, the efficiency of nuclear burning is 0.9%, thus accretion is a highly efficient process.

The luminosity of the source cannot exceed its Eddington limit  $L_{Edd}$  [20] for a steadily accreting spherically symmetric source. The limit is the result of competition between gravity on the infalling mass and the radiation pressure of the photons emitted from the disk. The maximum luminosity is

$$L_{Edd} = 4\pi GMm_p / \sigma_T = 1.3 \times 10^{38} m \text{ erg s}^{-1}, \quad (2.4)$$

where  $\sigma_T = 6.65 \times 10^{-25} \text{ cm}^2$  is a Thomson cross-section and  $m = M / M_\odot$ . The corresponding maximum accretion rate is

$$\dot{M}_{Edd} = L_{Edd} / \epsilon c^2 = 1.4 \times 10^{17} m / \epsilon \text{ g s}^{-1}, \quad (2.5)$$

where  $\epsilon$  is an efficiency of the accretion process.

Most of the radiation from the accreting matter comes from the innermost regions of the disk. For the geometrically thin, optically thick accretion disk (Novikov & Thorne [55], Shakura & Sunaev [79]) orbiting a Kerr black hole, the integrated flux emitted from the top and bottom faces of the disk peaks at location [63]

$$r_{peak} = r_{ms} / \eta, \quad (2.6)$$

where  $\eta$  varies from 0.62 to 0.76 as  $a$  goes from  $-1$  to  $1$  with  $\eta=0.71$  for a non-rotating black hole.

In the next section we discuss observational manifestation of a disk accretion, and later, in Section 2.4, the models of an accretion disk and how they apply to the observational data.

## 2.3 Spectral States

Historically, five different spectral states have been identified in black hole binaries. We summarize the properties of these states using information from the review papers by van der Klis [96], Esin et al. [21] and Rutledge et al. [77]. The classification of the states is approximate and is based on the shape of the energy spectrum, the value of the flux in the 1-10 keV energy range, and the timing variability. It is possible that black hole binaries do not occupy states, but their behavior changes continuously as a function of observable parameters. We list the spectral states in the order of increasing luminosity (increasing mass accretion rate): the quiescent/off state, low/hard, intermediate, high/soft and very high.

The quiescent or off state: the quiescent energy spectrum is non-blackbody with photon indices slightly softer than in the low state and the X-ray flux several orders of magnitude lower than in the other states.

The low or hard state: the energy spectrum has power law shape ( $dF/dE = \beta E^{-\alpha}$ , where  $dF/dE$  is the differential flux,  $E$  is the energy,  $\beta$  is the proportionality constant and  $\alpha$  is a constant called photon index) with a photon index of  $\sim 1.5$ -2 and an exponential cutoff around several tens of keV. The total luminosity is, in general, 10% of Eddington. The power spectrum is characterized by constant rms below some frequency ( $\sim 0.01$ -10 Hz), decreasing roughly as a power law with an index from  $\sim -2$  to  $\sim -1$  above this frequency. The broad-band variability is strong with a fractional rms of several tens of percent.

The intermediate state: this state is observed during transitions between low and high states. Its energy spectrum is intermediate between these two states showing both power law component  $>10$  keV (“hard component”) and ultra-soft component (“soft component”). The power spectrum is also intermediate in character between low and high states. It is constant below the break frequency ( $\sim 0.1$ -10 Hz), and decreasing above it.

The high or soft state: the energy spectrum is dominated by an ultra-soft blackbody-like component with a characteristic temperature  $\sim 1$  keV. The total luminosities exceed the low/hard state values. The power law tail is also seen, but this hard component is much less luminous than in the low state of the same source. The power law component does not show evidence of a cutoff. The photon index of the power law is almost fixed at  $\sim 2.5$ . The power spectrum has a  $1/f$  power law shape with a break at high frequencies. The rms variability is weak ( $\sim$  few %). In our studies of a BHC transient XTE J1859+226 no significant variability was detected in the power spectrum in its high state (see Section 6.4.1).

The very high state: the state is characterized by high luminosities ( $\sim 2$ -8 times higher than in the high/soft state). The two energy spectrum components, power law tail and blackbody component have comparable flux. The power law component has a photon index  $\sim 2$ -3 and does not show evidence of a cutoff even out to a few hundred keV. The power spectrum has  $1/f$  low-frequency noise, followed by constant level noise and then a power law. The QPOs with frequencies between  $\sim 3$ -10 Hz are present after the second break frequency. The broad-band noise is intermediate in fractional rms between the high and low states ( $\sim 1$ -15%). We detected a 4.9 Hz QPO, high-frequency variability (40-300 Hz) and broad-band noise in the XTE J1859+226 power spectra in its very high state (see Section 6.4 and 6.5).

There are exceptions to the canonical states. The spectral behavior of some sources (for example, GRS 1915+105 [52]) does not fit the canonical description. And not all of the sources display (according to current knowledge) all of the five spectral states.

The BHC binaries undergo state transitions on the scale from a month to several years. The sources with luminosity that varies over many orders of magnitudes during the transitions (or outbursts) are called transient sources. This definition is not strict, since there is no definite distinction between transient and non-transient sources (non-transient sources always change spectral states).

In this work we use “low”, “high” and “very high” terminology to describe the spectral states.

## 2.4 Disk Accretion Models

In this section we discuss various accretion models. These models are relevant to our understanding of various physical radii in the binary systems that are associated with high-frequency variability according to some theories. Some of these models accommodate movements of the inner accretion disk that are proposed to explain the change in the frequency of high-frequency QPOs.

The standard accretion model is geometrically thin, optically thick disk model obtained by Shakura & Sunyaev [79] and by Novikov & Thorne [55]. Shakura & Sunyaev introduced the parameter  $\alpha$  to incorporate the unknown mechanism of disk viscosity. They made the assumption that the viscosity is proportional to the total pressure (radiation plus gas). The radiation emitted from the disk has a modified blackbody energy spectrum (called disk-blackbody or multicolor spectrum). The name multicolor comes from a fact that the observed energy spectrum is the composite of the range of temperatures  $T(r)$ . In the model the accretion disk extends all the way down to the marginally stable orbit.

The above model successfully describes the soft component in the energy spectrum of X-ray binaries. However, a harder power law component observed in the spectrum cannot be explained within standard disk model. (BHCs and some neutron stars have significant fluxes of hard photons, up to 100 keV or more). The thin accretion disk model explains only the soft component in the energy spectrum. Thus, the models have been proposed that add Comptonization mechanisms to the disk models (Thorne & Price [93], Liang & Price [42], Ostriker [62], Bisnovatyi-Kogan & Blinnikov [2]). In these models, the soft photons from the disk gain energy by undergoing inverse Compton scattering through a hot electron plasma. The exact geometry, structure and origin of the Compton “cloud” or “corona” are unknown.



The advection dominated accretion flow (ADAF) models have been proposed by Chakrabarti & Titarchuk [7], and Narayan [54], and others to self-consistently explain the soft and hard power law energy spectrum components. In those models, the bulk of the energy is advectively carried inward along with the matter rather than radiated away. Different models propose different structure of the accreting region. Figure 2.1 illustrates the two-component advective flow (TCAF) model [7]. The accreting region consists of an optically thick Keplerian (geometrically thin) accretion disk surrounded by an optically thin sub-Keplerian disk. The Keplerian disk component behaves like a classical Keplerian disk. It consists of viscous gases that are accreted through the Roche lobe from a companion star. The soft X-rays dominate the radiation from the disk. The sub-Keplerian disk consists of low-viscosity gas that comes from the far regions of the Keplerian disk.

The sub-Keplerian gas has low angular momentum and flows advectively towards the black hole, keeping angular momentum constant. As it moves towards the black hole, the ram pressure due to the radial motion builds up. Where the ram pressure of the flow becomes the same as the thermal pressure of the rotation-dominated post-shock region (at the centrifugal barrier), a shock wave forms. The inner edge of both disks extends to the location of the standing shock. For matter with marginally bound angular momentum, the shock location is at  $\sim 5-10 r_s$  (depending on a black hole spin). For higher angular momentum, shocks form farther away. (If the angular momentum is lower than marginally bound, the disk might not have a shock at all). Note that in ADAF models the inner edge of the disk is located further from the black hole than in the thin disk models where the inner edge is located at the marginally stable orbit. The kinetic energy of the accreting sub-Keplerian gas is converted into thermal energy of the hot optically thin geometrically thick post-shock halo. The soft photons from the Keplerian disk undergo inverse Compton scattering through the electrons of the hot halo and emerge as hard X-rays. This model does not completely address the complex five-state phenomenology of the BHC binaries.

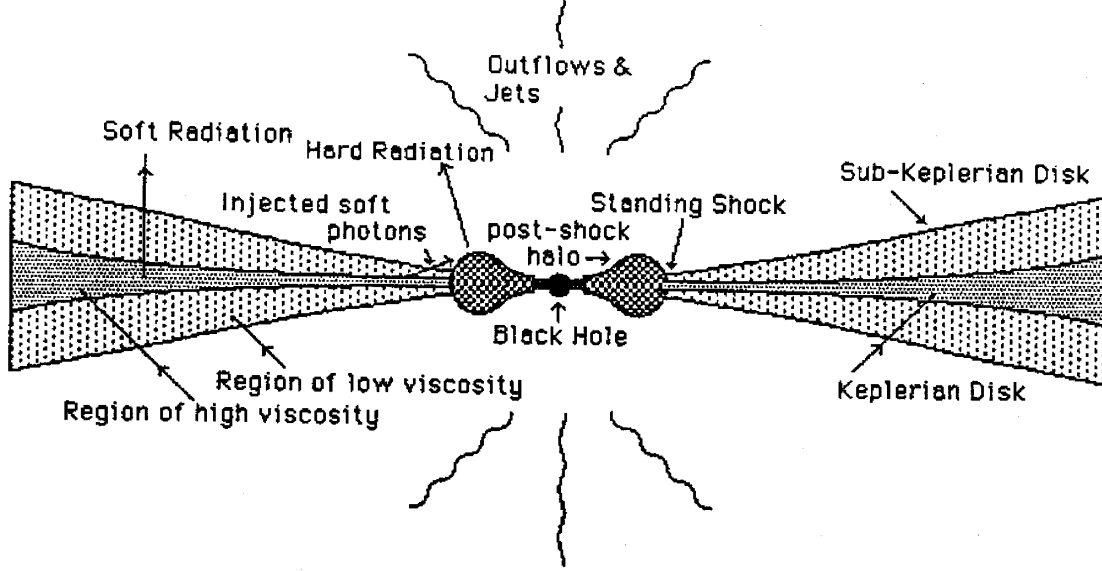


Figure 2.1 Diagram of the two-component advective flow model courtesy Chakrabarti & Titarchuk [7]. The components of the model are described in the text.

The spectral state changes in this model are driven by the change in a single parameter – mass accretion rate. During a low state (low accretion rate), the Keplerian disk radiates soft photons that are later Comptonized by the hot post-shock halo, accounting for the power law component in the energy spectrum. When the accretion rate increases, the additional flux of soft X-rays cools the post-shock halo through inverse Compton scattering. Thus the power law component is being suppressed and the ultra-soft spectrum is enhanced.

Esin et al. [21] developed a self-consistent ADAF model with a different structure of the accretion region that unifies four spectral states, except a very high state. In the model, the accretion flow consists of two zones, an inner advection dominated accretion flow that extends from the black hole horizon to a transition radius  $r_{tr}$ , and, beyond the transition radius, the outer optically thick, geometrically thin accretion disk. The disk is surrounded by a hot corona, which is a continuation of the inner ADAF.

The spectral state changes in this model are driven by the change in the accretion rate. At low mass accretion rate,  $\dot{m} \lesssim 0.01$  ( $\dot{m} = \dot{M} / \dot{M}_{Edd}$ ), the inner ADAF zone radiates inefficiently and the thin disk is at large radii ( $r_{tr} \sim 10^2 - 10^4 r_s$  for a non-rotating black hole). The luminosity is low and the source is in a quiescent state. As the accretion rate increases from  $\dot{m} = 0.01$  to  $\dot{m}_{crit} \approx 0.08$ , the radiation efficiency of ADAF increases and the system becomes more luminous. The spectrum is hard and peaks around 100 keV (on the energy times differential flux  $E(dF/dE)$  versus energy  $E$  plot). This is the low state.

As accretion rate further increases from  $\dot{m} > \dot{m}_{crit}$  to the second critical value about 10% higher, the size of the ADAF continuously shrinks, and the transitional radius decreases. Meanwhile, the X-ray spectrum changes continuously from hard to soft. This is the intermediate state. Finally, when  $\dot{m}$  is sufficiently large, the ADAF zone disappears and the disk extends all the way to the marginally stable orbit. The spectrum is dominated by the ultra-soft component with a weak hard tail. This is the high state. The model, however, cannot fully explain a very high state. The model also needs modifications to incorporate Kerr geometry.

## 2.5 High-Frequency QPOs in BHC Binaries

The overview and history of millisecond phenomena in X-ray binaries was presented in the Introduction (Section 1.1). In summary, a variety of millisecond phenomena (frequency range up to  $\sim 2$  kHz) have been recently discovered in neutron star binaries (reviewed by van der Klis [98]): accreting millisecond pulsar, burst oscillations, kilohertz QPOs and broad-band variability. However, the evidence of high-frequency signals in BHC binaries is scarce and just emerging. The broad-band variability has been recently reported to extend to  $\sim 300$  Hz in one BHC binary - Cygnus X-1 [31], [74] (see more details in Section 1.1).

Source	Frequency (Hz)	Rms (%)	References
GRS 1915+105	67	~1 at 2-60 keV	[52]
GRO J1655-40	295	~0.8 at 2-25 keV	[72],[51],[84]
4U 1630-47	184	~1.5 at 6-20 keV	[70],[73]
XTE J1550-564	184, 161, 186, 238 (1998 outburst)	~1 at 2-30 keV	[69],[29],[71]
	284, 235, 182 (1999 outburst)	~1.3 at 2-60 keV	[83],[84]
XTE J1859+226	187, 82, 150 (RXTE)	~3.5 at 6-60 keV	[45],[15]
	67, 134, 193* (USA)	~4 at 4-20 keV	this thesis

Table 2.2 List of all BHC transients with high-frequency QPOs. Fractional rms amplitudes could vary slightly for various observations. \* Frequencies derived from the combined power spectra of 50 observations (Section 6.4.1). For XTE J1859+226, RXTE and USA data are taken during the same outburst.

The QPOs in the frequency range ~100-300 Hz were found in five BHC transients (Table 2.2). The 67 Hz QPO in GRS 1915+105 is usually discussed together with the other four sources, although it is not clear if they are related. The QPOs in all five sources were detected in RXTE data. The QPO in XTE J1859+226 has also been confirmed with USA.

All of the sources, but GRO J1655-40, show the increase of fractional rms amplitude of high-frequency QPO with energy. (The detection of the 295 Hz QPO is limited only to one (2-25 keV) energy range [72]). For three sources - GRO J1655-40, XTE J1550-564 and 4U 1630-47, high-frequency QPOs were reported to be present only when the X-ray spectrum was dominated by a hard power law component.

There are two distinct groups among the sources listed in Table 2.2. One group has a stable frequency that does not change with changing luminosity of the source (GRS 1915+105, GRO J1655-40 and 4U 1630-47). The stability of the 295 Hz QPO in GRO J1655-40 is somewhat uncertain, since it was detected in a combined power spectrum from several observations. In the other group, the QPO frequency fluctuates significantly (XTE J1550-564 and XTE J1859+226). Two of the sources in the first

group (GRS 1915+105 and GRO J1655-40) are among the few known microquasars – they display radio jets.

The mass of GRO J1655-40 was measured to be  $7.0 \pm 0.2 M_{\odot}$  [61], making it an excellent BHC.

In the next section we discuss some physical models that attempt to explain high-frequency QPOs in BHC binaries. In Section 6.7.1 we discuss how these models relate to the experimental data on the BHC transients discussed above (Table 2.2) in general, and for XTE J1859+226 in particular.

## 2.6 High-Frequency QPO Models

Several models have been proposed to explain high-frequency QPOs in BHC binaries (see reviews by Cui [14] and van der Klis [98]). The models invoke general relativistic effects in the inner accretion disk because of the short timescales of the oscillations involved. In this section we provide a brief overview of some of the most popular models. But first, we give the characteristic frequencies of the accretion disk that are central to the understanding of high-frequency QPO models.

### 2.6.1 Characteristic Disk Frequencies

There are three fundamental general relativistic frequencies that are invoked in the models discussed below.

One is the Keplerian frequency  $\nu_{\phi}$  - the frequency of free particles, orbiting a Kerr black hole in circular orbits and in the equatorial plane, measured by a static observer at infinity [81]

$$\nu_{\phi} = M^{1/2} / (2\pi(r^{3/2} + aM^{3/2})) , \quad (2.7)$$

where the geometrized units  $c = G = 1$  are used.

The second is the radial epicyclic frequency  $\nu_r$  corresponding to radial perturbations of the circular orbits of free particles. For a Kerr black hole, as measured by an observer far from the disk [60]

$$\nu_r^2 = \nu_\phi^2 (1 - 6M/r + 8aM^{3/2}/r^{3/2} - 3a^2M^2/r^2). \quad (2.8)$$

The third frequency is the vertical epicyclic frequency  $\nu_\theta$  corresponding to vertical perturbations of free-particle circular orbits [33]

$$\nu_\theta^2 = \nu_\phi^2 (1 - 4aM^{3/2}/r^{3/2} + 3a^2M^2/r^2). \quad (2.9)$$

For Newtonian gravity these three frequencies are degenerate. However, general relativistic effects break the degeneracy.

## 2.6.2 Keplerian Motion Model

One proposed model [52], [72] has the high-frequency QPOs in black holes associated with the Keplerian motion of self-luminous blobs or hot spots at the marginally stable orbit around the black hole. Another possibility in this model has the blobs occulting, not self-luminous. For a rotating Kerr black hole, the Keplerian frequency, given by  $\nu_\phi$  (2.7), in practical units is

$$\nu_\phi = 3.22 \times 10^4 m^{-1} ((r/r_g)^{3/2} + a)^{-1} \text{ Hz}, \quad (2.10)$$

where  $m = M/M_\odot$  and  $r_g = GM/c^2 \cong 1.5m [\text{km}]$ .

Associating a QPO frequency with a Keplerian frequency provides restrictions on the relationship of the black hole mass and the angular momentum for a given radius. The radius can be the radius of a marginally stable orbit, or any other physical radius of a region associated with the excitation of the QPO.

An important inconsistency results from tying the QPO frequency to the Keplerian frequency at exactly the inner edge of the disk at the last marginally stable orbit. General relativistic effects cause the emissivity (of the unperturbed disk) to vanish at the last stable orbit [63], [26].

Thus in this model, the QPO frequency can be interpreted as a Keplerian frequency at a model-dependent radius  $r_{peak}$  corresponding to the region of peak disk integrated flux, close to the inner edge of the disk (see (2.6) for the value of  $r_{peak}$  for the geometrically thin, optically thick accretion disk). Alternatively, other radii like the standing shock radius in the TCAF [7] model or a transition radius in the ADAF model of Esin et al. [21] can be considered.

### 2.6.3 Diskoseismic Oscillations Model

Nowak et al. [58] proposed to associate stable QPOs with oscillation modes in the accretion disk. These normal modes of oscillation are trapped in what are effectively resonant cavities of the disk that exist due to relativistic effects [32], [56], [57], [64], [82], [99]. There are three fundamental disk frequencies - (2.7), (2.8) and (2.9) that create trapping regions.

Three types of trapped adiabatic oscillations have been identified: internal gravity (g) modes, corrugation (c) modes and pressure (p) modes. The g-mode oscillations involve predominantly vertical displacements of the disk. They are trapped near the maximum of the radial epicyclic frequency in the resonant cavity (the radial epicyclic frequency reaches its maximum at  $r = 8M$  for a non-rotating black hole and goes to zero at  $r_{ms}$ ). They occupy a large radial area of size  $\sim M$  of the inner region in the disk where most of the luminosity is emitted. Therefore, these modes are expected to be the most likely to be observed. The p-modes result from mostly radial displacements trapped between the inner edge of the disk and radii inward of the location of the radial epicyclic frequency maximum. These modes are very narrowly confined at the inner disk edge and, thus, do not significantly modulate the luminosity. A second branch of p-modes with larger radial

extents may be trapped in the outer region of the disk. The uncertain physics of the outer boundary of the disk complicates predictions about their behavior. The c-mode oscillations are non-radial incompressible waves that slowly precess about the black hole spin axis. They are trapped in the inner disk where the difference between the Keplerian and vertical epicyclic frequency is significant (the difference increases with black hole angular momentum). Since the waves are incompressible, they cause little temperature or pressure fluctuations in the disk, but can modulate X-ray emission from the disk or scattered photons from Comptonizing corona. The modulation is due to the changing orientation of the disk that results in the changing projection of the area of the disk in the direction of observer.

The radial g-modes are the most observable and robust. The g-mode frequencies are

$$f_g = 7.14 \times 10^2 (1 - \varepsilon_{nj}) m^{-1} F(a) \text{ Hz}, \quad (2.11)$$

$$\varepsilon_{nj} \approx \left( \frac{n+1/2}{j+\delta} \right) \frac{h}{r},$$

where  $m = M / M_{\odot}$  and  $F(a)$  is a known function of the angular momentum parameter, ranging from  $F(0)=1$  to  $F(0.998)=3.44$  ( $F(-1)=0.60$ ). The properties of the disk enter through the small correction term  $\varepsilon_{nj}$ , which depends on the disk thickness  $2h(r)$  and the radial ( $n$ ) and vertical ( $j$ ) mode numbers, with  $\delta \sim 1$ . For the thin-disk models in which  $h/r \sim 0.1 L / L_{Edd}$  (in the mode trapping region),  $\varepsilon_{nj}$  is typically on the order of 0.01 for the lowest modes ( $n \sim j \sim 1$ ). Thus, the mode frequency is relatively independent of luminosity, and radial g-mode can be used to explain stable frequency QPOs.

The quality factor,  $Q = f / \Delta f$ , of the QPO caused by the lowest g-modes can range from  $\sim 1$  to  $\sim 100$  depending on the disk viscosity and the number of modes excited. The rms amplitude of these QPOs is estimated to be on the order of  $\sim 1\%$  [57].



### 2.6.4 Relativistic Precession Models

Inclined with respect to the equatorial plane (plane perpendicular to the spin axis), free-particle eccentric orbits in the vicinity of a spinning black hole experience nodal precession (a wobble of the orbital plane) due to relativistic frame dragging [41], and relativistic periastron precession.

The nodal and the periastron precession frequencies are given by [86]

$$\nu_{nod} = \nu_{\phi} - \nu_{\theta}, \quad (2.12)$$

$$\nu_{per} = \nu_{\phi} - \nu_r, \quad (2.13)$$

where  $\nu_{\phi}$  is the orbital frequency (2.7), (2.10),  $\nu_{\theta}$  is the vertical epicyclic frequency (2.9) and  $\nu_r$  is the radial epicyclic frequency (2.8).

Two models have been proposed to explain high-frequency QPOs using relativistic precession. They differ in which frequencies the authors associate with high-frequency QPOs.

Cui et al. [13], [12] proposed that certain types of QPOs in BHC binaries are produced by X-ray modulation at the nodal precession frequency of the accretion disk  $\nu_{nod}$ . The node is a point where a nonequatorial orbit intersects the equatorial plane. During the nodal precession, the tilted orbital plane of a test particle precesses around the same axis and in the same direction as the black hole spin. This model does not require eccentric orbits.

Lense & Thirring [41] derived a nodal precession frequency  $\nu_{nod}$  in the weak-field limit ( $M/r \ll 1$ )

$$\nu_{nod} = f_{LT} = 6.45 \times 10^4 \text{ am}^{-1} (r/r_g)^{-3} \text{ Hz}, \quad (2.14)$$

where  $m = M / M_{\odot}$  and  $r_g = GM / c^2$ .

For a rapidly rotating black hole ( $a \approx 1$ ), the accretion disk can extend very close to the event horizon ( $r = M$ ), where the weak-field approximation breaks down. The exact problem has been solved analytically by Wilkins [103]. Plots of disk precession frequency in this case as a function of angular momentum for various masses at the radius  $r_{peak}$  can be found in Cui et al. [12]. For certain models, the precession frequency is calculated assuming the precession is confined to the innermost stable orbit. As with the Keplerian motion model, the frequency can be calculated for any physical radius of interest in the disk.

Stella et al. [86] proposed that high-frequency QPOs in BHC binaries are produced by X-ray modulation at the periastron precession frequency  $\nu_{per}$  of the accretion disk. The theory attempts to explain the observed correlation both in neutron star and BHC binaries between the low-frequency and high-frequency QPOs (or peaked noise components). In neutron star binaries with kHz QPOs, the correlation exists between the low-frequency QPOs and lower kHz QPOs. These phenomenological correlations (PBV correlations) were recently discovered by Psaltis, Belloni, & van der Klis [67]. The correlation is also observed between lower and upper kHz QPOs in neutron star binaries. Stella et al. [86] proposed to identify the high-frequency QPOs in neutron star and BHC binaries, and lower kHz QPOs in neutron star binaries with  $\nu_{per}$ , low-frequency QPOs with  $2\nu_{nod}$  and upper kHz QPOs in neutron star binaries with the Keplerian frequency  $\nu_{\phi}$  of the innermost disk regions.

In the weak field ( $M / r \ll 1$ ) and slow rotation ( $a \ll 1$ ) approximation, the dependence of these frequencies on  $\nu_{per}$  has the explicit form [86]

$$\nu_{\phi} \approx 3.3 \times 10 m^{-2/5} \nu_{per}^{3/5} \text{ Hz}, \quad (2.14)$$

$$\nu_{nod} \approx 6.7 \times 10^{-2} a m^{1/5} \nu_{per}^{6/5} \text{ Hz}, \quad (2.15)$$

where  $m = M / M_{\odot}$ .

The dependencies (2.14) and (2.15) match the observed patterns of low-frequency versus high-frequency QPO diagrams for many neutron star and some BHC sources [86]. The position of the QPO on the diagram gives information about the location of the QPO in the disk. For high-frequency QPOs these radii are close to marginally stable orbits. Note that this theory implies that both low-frequency and high-frequency QPO originate from the same narrow annulus in the disk.

In Section 6.7.1 we discuss how this theory applies to high-frequency QPOs in BHC binaries.

Cui et al. [12], Merloni et al. [50] and Stella et al. [86] have reviewed the potential problems of the relativistic precession models. Among them: explanation of the origin of the tilted orbits; mode excitation mechanisms; X-ray modulation mechanisms and precession confinement to a particular radius. Also, why modes only with particular frequencies  $\nu_{nod}$  or  $\nu_{per}$ ,  $2\nu_{nod}$  and  $\nu_{\phi}$  are excited needs to be explained.

In both of the relativistic precession models and the Keplerian model, the QPO frequency variations of a given source are considered to be due to the variations in the location of the inner edge of the accretion disk or other characteristic radius (as discussed in Section 2.6.2.) At present, the physical mechanism determining the radius at which QPOs are produced and the radius variation in each source and across different sources are unknown. There is evidence in neutron star binaries [98] that the radius decreases with increasing accretion rate. The ADAF model by Esin et al. [21] discussed in Section 2.4 incorporates the changing location of the inner edge of the disk.

## **CHAPTER 3: UNCONVENTIONAL STELLAR ASPECT EXPERIMENT**

### **3.1 ARGOS Mission**

The Unconventional Stellar Aspect (USA) is one of the experiments on the Advanced Research and Global Observation Satellite (ARGOS). The full review of the ARGOS mission and the USA experiment is provided by Ray et al. [68]. The 5000 lb ARGOS satellite was launched in space on February 23, 1999 aboard a Boeing Delta-II rocket. ARGOS carries 9 experiments with various scientific and engineering goals. USA is mounted on the anti-velocity face of ARGOS as shown in Figure 3.1. The scientific goal of USA is the timing of bright Galactic X-ray binaries, pulsars, AGN and the exploration of applications of X-ray sensor technology. USA was activated on April 30, 1999.

ARGOS is flying in a low-earth nearly circular orbit at an altitude of 830 km with an orbital inclination of  $98.7^\circ$ . The orbit is sun-synchronous with a beta angle of  $25\text{--}45^\circ$ , i.e. it crosses the equator at local times of about 14:00 on the day side and 02:00 on the night side. Due to this nearly polar orbit, USA passes through the Earth's radiation belts, located above  $|50^\circ|$  latitude, several times per orbit. Since the detector is turned off to prevent breakdowns in the radiation belts and the South Atlantic Anomaly, the data is

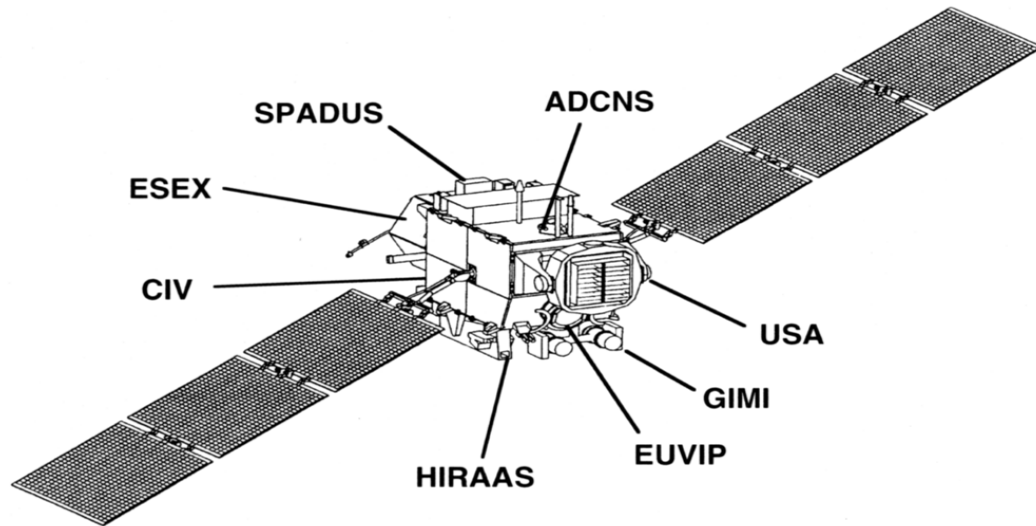


Figure 3.1 The Advanced Research and Global Observation Satellite (ARGOS).

collected effectively during two  $\sim 20$  minute low latitude segments per orbit (out of 102 minutes orbital period). The availability of some sources can be restricted due to Earth occultation, yoke obscuration and a minimum viewing angle to the sun of  $\sim 30^\circ$ .

### 3.2 Instrument Status

On June 8, 1999 one of the two USA detectors (Detector 1) suffered an event that caused high-level gas leak, and the detector lost its gas supply. Probably, the thin,  $5\ \mu\text{m}$ , Mylar window was hit and punctured by a small space debris. Currently, only Detector 0 is operational cutting to half the initial effective area of the experiment.

### 3.3 USA Instrument

The USA instrument consists of two detector units. Each detector unit consists of a multiwire constant flow proportional counter, collimator, gas system and detector electronics, shown together in Figure 3.2. The detailed views of one USA detector unit and the proportional chamber are shown in Figure 3.3 and Figure 3.4.

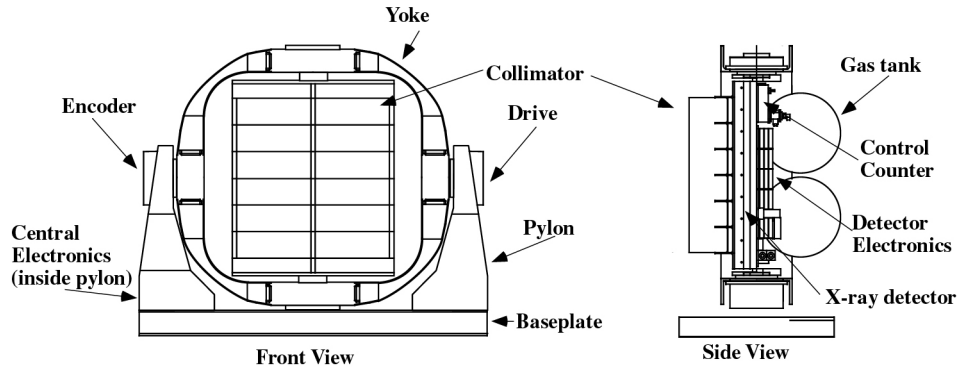


Figure 3.2 USA detector front and side view.

The proportional counters are covered with a 5  $\mu\text{m}$  Mylar window, 85% transmission nickel mesh to support the Mylar window, and a 1.9  $\mu\text{m}$  thick aluminized Mylar heat shield. The detectors are filled with a P-10 gas (a mixture of 90% argon and 10% methane) at a pressure of 16.1 psia (at room temperature). The gas is supplied from a spherical titanium gas bottle mounted on the detector backplane. The detector interior contains an array of wires that forms two layers of nine 2.8 square cm cells, each containing one anode wire that runs the length of the chamber. A perimeter wire runs along the periphery of the counter as a part of a cosmic ray veto system. The detector electronics are designed to accept X-ray events that trigger only one anode wire. Cosmic ray events detected in more than one wire or in the perimeter wire are rejected with  $\sim 99\%$  efficiency. The veto system and detector electronics are discussed in more detail in Section 5.1.1.

The chamber high-voltage is automatically adjusted to stabilize the gain, using a feedback mechanism that monitors the pulse height distribution of the X-ray events from a  $^{55}\text{Fe}$  calibration source in a small proportional control counter.

The collimators support the counter window and restrict the field of view to  $1.3^\circ \times 1.3^\circ$  (FWHM) with  $\sim 0.05^\circ$  flat top. The collimator is a honeycomb of hexagonal copper tubes

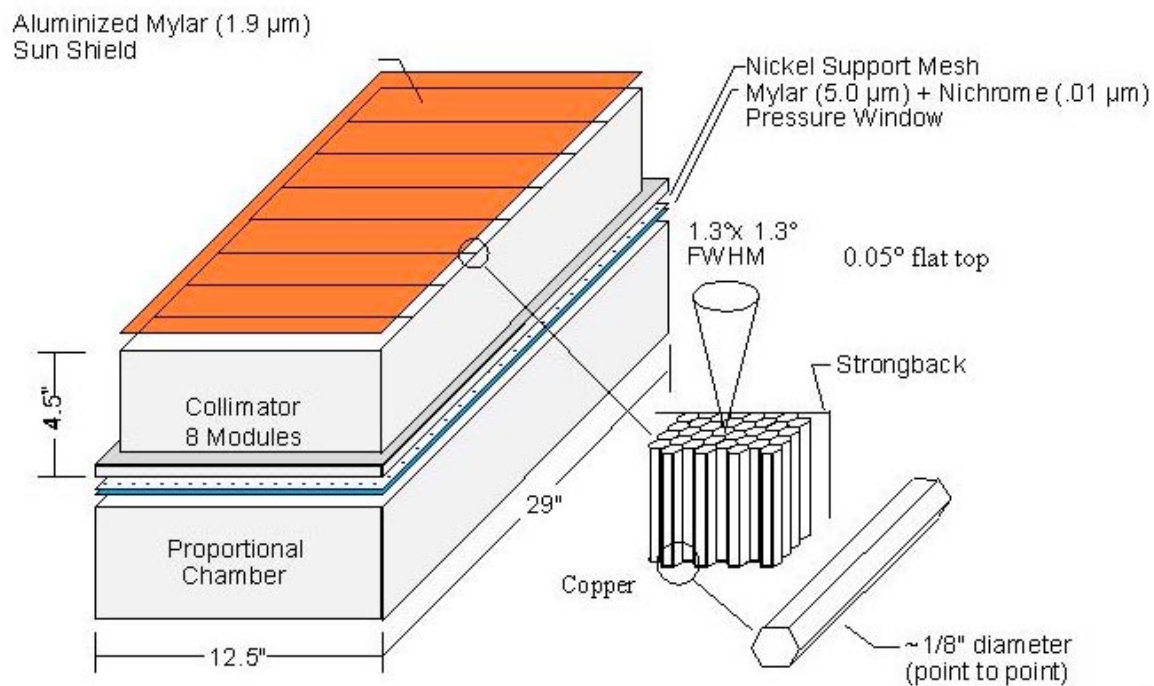


Figure 3.3 Detailed view of one USA detector unit.

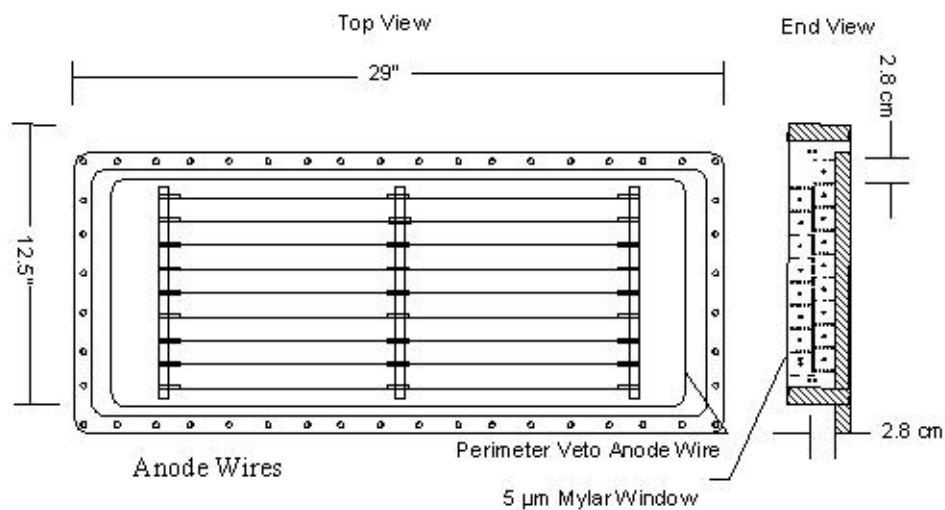


Figure 3.4 USA proportional chamber.

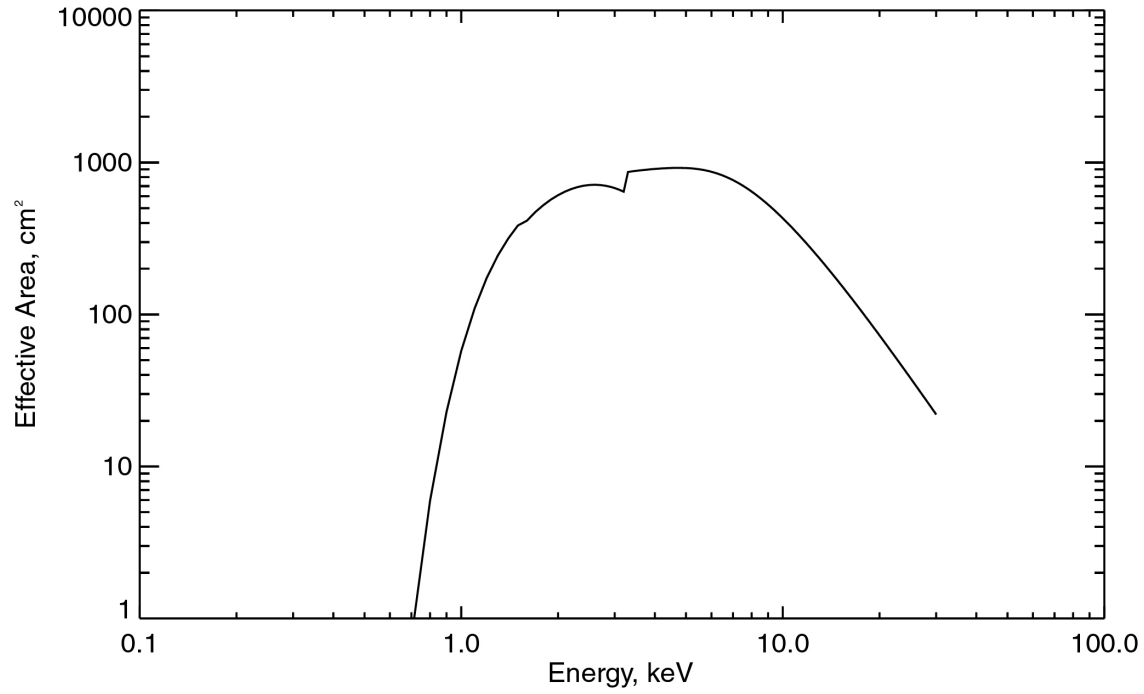


Figure 3.5 USA effective area for one detector unit and two wire layers as a function of photon energy.

formed into eight modules. For a discussion of the construction and calibration of the collimator see Wen [100].

The two detector units are supported by a two-axis gimbal pointing system. The units are supported by a yoke along an axis that enables rotations in yaw. The yoke is supported by two pylons along a perpendicular axis that enables rotations in pitch. Each axis has a drive unit that forms the pivot on one end of the axis and a position encoder unit that supports the opposite end.

The total collecting area of one detector is  $1513 \text{ cm}^2$ . The energy range is  $\sim 1\text{-}20 \text{ keV}$  (see Figure 3.5 for the effective X-ray acceptance of one detector), and energy resolution is 17% at 5.9 keV.



The Central Electronics (CE), including the Detector Interface Board (DIB), performs time tagging and formatting of the X-ray science and housekeeping data (see Section 5.1.2 for more details on DIB). The event time tagging clock inside the detector electronics enables  $\sim 1 \mu\text{s}$  accuracy. This clock is synchronized with the 1 Hz spacecraft clock (with corresponding GPS time tag). There are five telemetry DIB data modes – one spectral and four event modes. The best timing resolution USA can achieve is  $2 \mu\text{s}$ . Section 5.2.1 describes the USA data modes in detail.

## CHAPTER 4: DATA ANALYSIS TECHNIQUES AND DEADTIME

### 4.1 Fourier Transform

Time variability in astrophysical X-ray sources is often studied by means of the Fast Fourier Transform (FFT), which ultimately yields a Fourier power spectrum.

The amplitudes  $X_j$  of the complex discrete Fourier transform of a time series of length  $T$  divided into  $N$  equal-length bins are

$$X_j = \sum_{k=0}^{N-1} x_k e^{i2\pi jk / N} \quad (j = 0, 1, 2, \dots, N/2), \quad (4.1)$$

where  $x_k$  ( $k=0, 1, \dots, N-1$ ) is the number of counts in the  $k^{th}$  time bin of the light curve. ( $N$  is usually an integer power of 2 to enable high efficiency of the FFT algorithms). The corresponding Fourier frequency is  $f_j = j/T$ . The PSD at frequency  $f_j$  is equal to the squared magnitude of the  $j^{th}$  Fourier coefficient  $|X_j|^2$ .

The distribution of the PSDs over all possible frequencies forms the Fourier power spectrum. The Leahy normalized power spectrum [36] is given by

$$P_j = \frac{2|X_j|^2}{N_{ph}}, \quad (4.2)$$

where  $N_{ph}$  is the total number of photons within a time series of length  $T$  ( $N_{ph}$  equals to the value of the zeroth Fourier coefficient,  $x_0$ ). For a purely Poisson process, this definition of the power spectrum gives the PSD a value of 2, and the  $P_j$  follow a  $\chi^2$  distribution of 2-degrees of freedom.

## 4.2 Deadtime Effects in General

In this section we discuss general effects of the deadtime on timing data. For a thorough discussion of the subject see reference [106].

### 4.2.1 Introduction

The deadtime,  $\tau$ , is a time during which the detector is occupied processing an event and thus cannot process another event. For practical reasons two types of deadtime are usually discussed [53]. They differ in the way a detector responds to incoming events while the detector is dead. The detector is said to have extended (or paralyzable) deadtime if an event that arrives while the detector is processing the previous event extends the deadtime by  $\tau$ , measured from the last arrival time. In the case of non-extended (or non-paralyzable) deadtime an incoming event has no effect whatsoever while the detector is dead.

These two types of deadtime are usually discussed for two reasons. First their effects on counting statistics had been extensively studied and analytical solutions exist to correct the data for these types of deadtime [106]. Second in some cases they can approximate rather well, in certain regimes, the real deadtime behavior of a detector.

The hardware and signal processing software of the timing detectors usually introduce non-extended or extended or a combination of both deadtime types into the data stream.

These idealized types in some cases and timing regimes can be a good approximation to reality. However, a number of additional factors should be taken into account when describing a detector's deadtime. For example, there can be more than one signal path in the detector, e.g., veto and coincidence paths. In this case the interaction between paths should be taken into account. In addition there can be very specific detector features or malfunctions that disturb the event timing. Due to all these factors, the deadtime of a real detector is usually not characterized using the simplest model. Hence, a deadtime calibration of the detector is required that entails a careful examination of how the event-timing stream is modified by the detector.

In this thesis we address these issues with regard to the USA detectors. Since the USA electronics deadtime is best described as non-extended, we focus more on the discussion of this type of deadtime.

For the practical purposes of analyzing X-ray data there are two important ways that deadtime affects the data. Deadtime decreases the incident event rate due to the loss of events and changes the statistical behavior of the incident process. In the analysis presented in this report we assume that the incident events obey Poisson statistics.

#### **4.2.2 Change in the Incident Counting Rate**

In the case of non-extended deadtime,  $\tau$ , in the detector, the incident event rate,  $r_{in}$ , and the observed event rate,  $r_o$ , are related by [106]

$$r_o = \frac{r_{in}}{1 + r_{in}\tau} . \quad (4.3)$$

For extended deadtime,  $\tau$ , the relationship is

$$r_o = r_{in}e^{-r_{in}\tau} . \quad (4.4)$$

The deadtime is more noticeable at high counting rates. When the rates are low the deadtime occurs mostly during the gaps between events. At high rates the time interval between events is comparable to the deadtime, and a large fraction of events are lost.

For small rates or small deadtime (i.e.  $r_{in}\tau \ll 1$ ) the distinction between the two types becomes negligible. To first order in  $r_{in}\tau$ , the observed event rate formulas are the same

$$r_o \approx r_{in}(1 - r_{in}\tau) . \quad (4.5)$$

### 4.2.3 Change in the Original Statistics

The deadtime affects the original Poisson statistics of the process. Of particular interest is the effect of the deadtime on the time interval distribution and the Power Spectral Density (PSD).

The time interval distribution, i.e. the distribution of intervals between photon arrival times, can be examined for the presence of deadtime effects. For a Poisson process, the time interval probability density  $f(t)$  is

$$f(t) = U(t)r_{in}e^{-r_{in}t} , \quad (4.6)$$

where  $U(t)$  is the unit-step function.

The probability density  $F(t)$  for the Poisson process with non-extended deadtime will be

$$F(t) = U(t - \tau)r_{in}e^{-r_{in}(t - \tau)} . \quad (4.7)$$

Thus, due to non-extended deadtime, the exponential distribution gets shifted by the amount of deadtime,  $\tau$ .

In the case of extended deadtime, the probability density is calculated using

$$F(t) = \sum_{j=1}^J A_j, \quad (4.8)$$

where

$$A_j = U(t - j\tau)[(-1)^{j-1}/(j-1)!]r_{in}^j(t - j\tau)^{j-1}e^{-jr_{in}\tau}, \quad (4.9)$$

and  $J$  is the largest integer below  $t/\tau$ .

Figure 4.1 shows an example of a binned time interval distribution of a Poisson process with non-extended deadtime.

For an actual experiment, the power spectrum (4.2) consists of two components: an intrinsic signal from the source, and noise from the counting statistics introduced by the detection process (statistical fluctuations in the data) [106]. The Fourier amplitudes of the actual time series are the sum of source signal  $X_j^{signal}$  and noise  $X_j^{noise}$

$$X_j = X_j^{signal} + X_j^{noise}. \quad (4.10)$$

The power spectrum (ignoring normalization) will be equal to

$$P_j = P_j^{signal} + P_j^{noise} + X_j^{signal} X_j^{*noise} + X_j^{*signal} X_j^{noise}. \quad (4.11)$$

If the two processes are independent, the cross terms average to zero and the power spectrum of the intrinsic source signal is

$$P_j^{signal} = P_j - P_j^{noise}. \quad (4.12)$$

The cross terms do not always average to zero. If the deadtime effects are significant the processes might not be independent. In this case after we subtract the noise term from the power spectra there will still remain some contribution from the counting statistics.

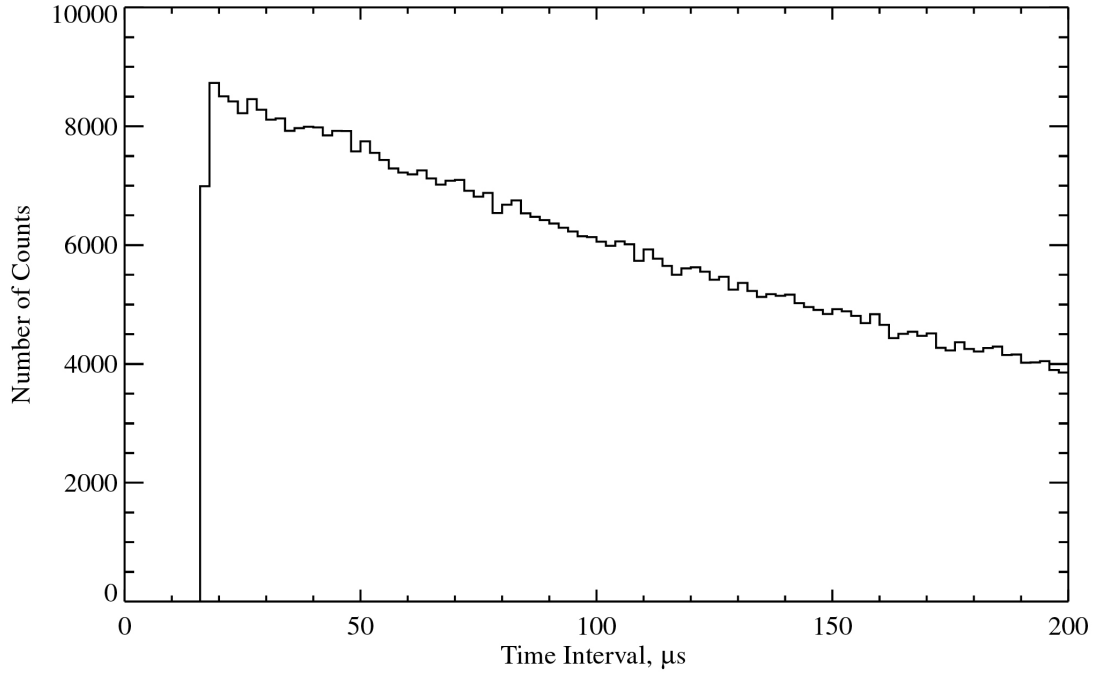


Figure 4.1 Binned time interval density,  $F(t)$ , for a Poisson process affected by non-extended deadtime. Bin size:  $2 \mu\text{s}$ . The curve results from a simulation of one million Monte Carlo events with  $r_o = 4100 \text{ Hz}$  counting rate and deadtime  $\tau = 16.4 \mu\text{s}$ . The simulation parameters are relevant to the discussions of Section 5.4. The distribution is shifted from zero by the value of the deadtime.

In the absence of deadtime  $P_j^{noise}$  is the power spectrum of a Poisson process. The Leahy normalized power spectrum of a Poisson time series has an expected value of 2.

The presence of the deadtime in the detector affects  $P_j^{noise}$  in a certain way depending on the type and value of the deadtime, counting rate, and the size of the time series bin. An analytical expression exists for  $P_j^{noise}$  in the special cases of non-extended and extended deadtime [106]. Figure 4.2 shows an example of a power spectrum of a Poisson process with non-extended deadtime. The dotted line shows the power spectrum of a Poisson time series.

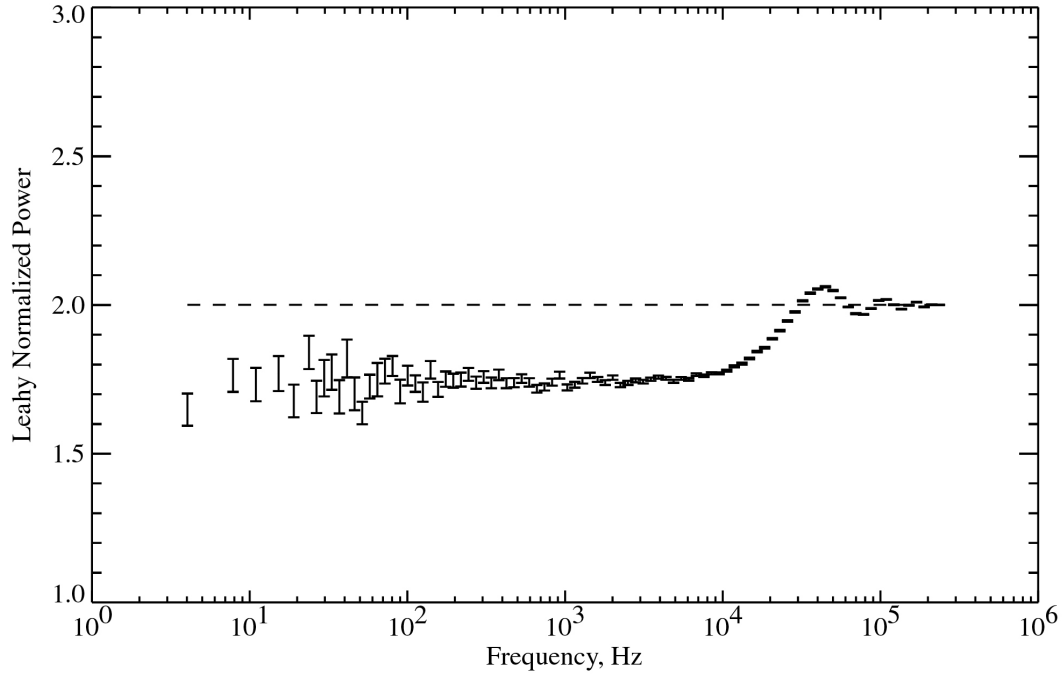


Figure 4.2 Leahy normalized power spectrum of a Poisson process with non-extended deadtime. The curve results from a simulation of one million Monte Carlo events with  $r_o=4100$  Hz counting rate and a deadtime  $\tau=16.4$   $\mu$ s. The simulation parameters are relevant to the discussions of Section 5.4. The time series bin size is 2  $\mu$ s. The segment length is  $T=0.26$  s. The plot is an average of 930 PSDs. The power spectrum is logarithmically binned. The dashed line is the Leahy normalized power spectrum for a Poisson process without deadtime.

One practical result of a deadtime calibration is to describe  $P_j^{noise}$  for a particular detector.



## **CHAPTER 5: USA ON-GROUND DEADTIME CALIBRATION**

Obtaining physics from the USA detector for a number of important topics requires an accurate deadtime model for the detector. In particular, an accurate deadtime model is important when the data is being searched for small high-frequency signals, like the one detected in XTE J1859+226 and discussed in this thesis.

In this work, we discuss primarily the on-ground calibration efforts. Our results focus on USA thermal vacuum and brass board studies of the detector's deadtime behavior. The chapter consists of two parts. In Sections 5.1-5.4 we describe USA preflight thermal vacuum tests, issues in USA timing, the deadtime model, and methods for correcting deadtime and instrumental effects. Methods are developed for power spectrum correction when no selection of time series based on energy is made (i.e. power spectra are calculated for all the energy channels combined). While looking at on-orbit data, the USA team discovered that in some cases, power spectra calculated for selected energy channels are distorted. At the end of this chapter (Section 5.5) we describe our preliminary understanding of this effect. We derive a correction method, which is based on the results of the first sections.

This chapter presents calibration results for both USA detectors. Currently only detector

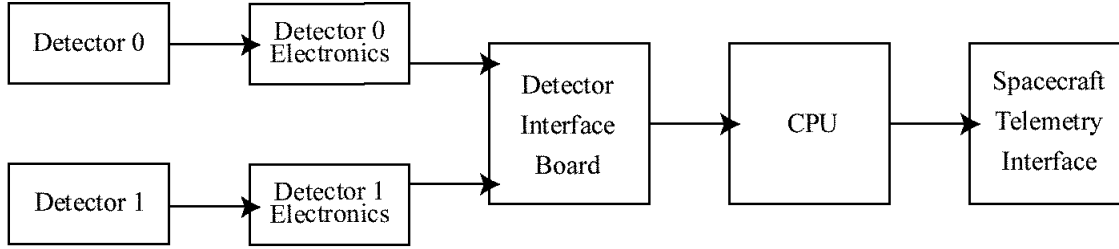


Figure 5.1 Diagram of the USA event timing flow. Currently only detector 0 is functioning in orbit.

0 is functioning in orbit (see Section 3.2).

The USA thermal-vacuum calibration tests were carried out by the NRL and SLAC collaboration.

## 5.1 USA Deadtime Mechanisms

There are two electronics units that introduce deadtime effects in the USA detectors: the detector electronics boards and the Detector Interface Board (DIB). Each of the two proportional counters has its own set of detector electronics boards. The two detectors share one DIB. For details of the USA electronics and the DIB consult [104].

Figure 5.1 shows the diagram of the timing signal flow from the proportional counters to the spacecraft telemetry interface.

### 5.1.1 Deadtime Effects Introduced by the Detector Electronics

#### Detector Electronics Response to Nominal Events

The detector electronics boards process the signals from the proportional chamber anodes. For each valid event (i.e. event that is not vetoed and does not occur while the detector is dead), a 1 bit Valid Event Flag (VEF) with 1  $\mu$ s accuracy, an event time, a 1-bit layer ID, and a 7-bit pulse height datum is produced by the detector electronics and the DIB.

The block diagram for the part of the detector electronics relevant to the deadtime discussion is shown in Figure 5.2.

The anode wires in each detector are grouped into five paths: four signal paths and one perimeter veto path. Each detector has two layers of anode wires. Each layer has only two continuous wires, A and B. These wires interleave to form a single layer. There is also a single perimeter wire, which is a part of the cosmic ray veto system. Overall in one detector the signals are collected from wires 1A (layer 1), 1B (layer 1), 2A (layer 2), 2B (layer 2), and the perimeter veto wire, or 5 signals in all.

Each signal from the chamber has its own amplifier and discriminator. A pulse coming from the chamber is amplified and passes through the discriminator if its amplitude exceeds the 0.106 V discriminator threshold. After the pulse exits the discriminator it goes through the monostable timer, which stretches the signal and creates digital pulse. The signal is stretched to a width of 5  $\mu\text{s}$  to be processed by the veto logic circuitry further down the line. Digital pulses from the five chains enter the Digital Veto Logic and ADC (Analog to Digital Converter) Control block. The analog sum of four of the five amplified analog signals, wires 1A, 1B, 2A, and 2B, enters the Pulse Stretcher block. If the sum is greater than 0.14 V (discriminator threshold inside the Pulse Stretcher block), the analog signal is stretched, nominally to about 16  $\mu\text{s}$  (on the USA brass board this number was measured to be 15.6  $\mu\text{s}$ ). The Digital Veto Logic and ADC Control block receives a signal from the Pulse Stretcher Block that indicates whether the pulse is currently being stretched. It also sends a control signal to the ADC to start conversion and receives a status signal from the ADC indicating whether the ADC is converting.

The Digital Veto Logic and ADC Control block carries out the rejection of background events. This block uses a 1 MHz clock, which provides a 1  $\mu\text{s}$  accuracy for all timing functions the block performs. Any signal in one of the five paths coming into this block will keep it busy for  $\tau_{logic}=7.5\pm1$   $\mu\text{s}$  (it takes 7.5 clock cycles to process the event), and no other signal can be processed by the block during this time. During the first

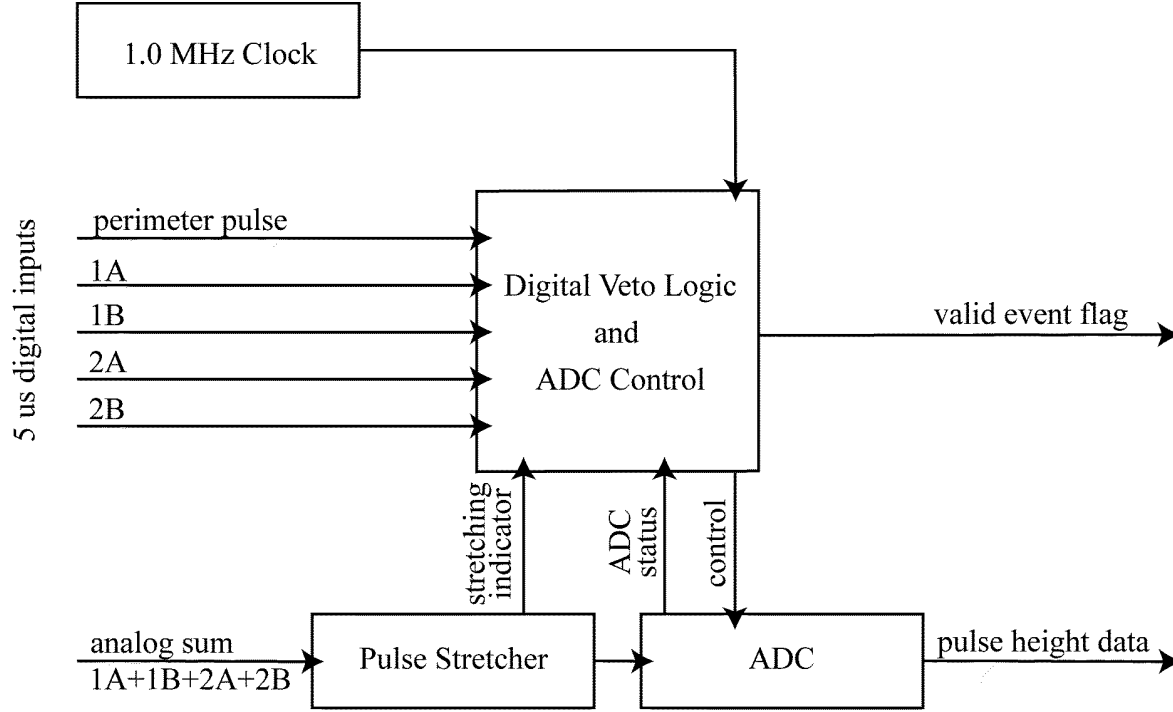


Figure 5.2 Diagram of the USA detector electronics.

$3.5 \pm 1 \mu\text{s}$  ( $\tau_{\text{coin}}$ ) the decision is made whether the event is valid or should be vetoed. If the event is valid, VEF is generated (1-bit digital signal with  $1 \mu\text{s}$  accuracy), and a signal is sent to the ADC to start conversion. The ADC digitizes the input pulse and, when finished, outputs a 7-bit pulse height datum (the ADC is actually a 12-bit unit, but only the highest order 7 bits are read out and used to produce the pulse height information for the various data modes); the layer ID is also supplied by this logic. If the event is vetoed, no VEF and no pulse height data are output.

The following events are vetoed: 1) Any event that triggers the perimeter veto wire. 2) Any coincidence event, which is an event that causes a signal in more than one out of five wires. Two pulses need to come closer than  $\tau_{\text{coin}}$  to be considered in coincidence. In addition, the VEF and the pulse height data will not be output when the detector is dead (busy processing a previous event).

A period of deadtime in the detectors electronics can be generated by one of the following: 1) A valid X-ray event. 2) A background perimeter or coincidence event.

A valid X-ray event creates a  $\tau_{valid}$  deadtime, during which no other event can be detected. Deadtime  $\tau_{valid}$  is the longer of two times: the duration of the output signal of a monostable one-shot,  $\tau_{one-shot}$ , or the duration of the ADC conversion process counted from the first instant of event detection ( $\tau_{ADC} + \tau_{coin}$ ). The value of the  $\tau_{valid}$  deadtime is not a fixed number. It changes slightly due to the specific monostable one-shot behavior and the interplay between the one-shot and the ADC for events very close in time.

In more detail, the incoming signal pulse has to be stretched before it arrives at the ADC input since the ADC requires a constant value at its input during conversion (it does not have a sample and hold on its input). The Pulse Stretcher block is driven by the output of the monostable one-shot (discussed in more detail below) and stretches the pulse for the duration of  $\tau_{one-shot}$ . Once the stretching starts, the stretching indicator goes high. The ADC receives a control signal from the Digital Veto Logic and ADC Control block  $3.5\mu s$  ( $\tau_{coin}$ ) later, if no veto has occurred, and starts converting. At this point ADC status indicator goes high. The ADC status indicator stays high for the duration of  $\tau_{ADC}$  from the moment the conversion begins. The ADC keeps converting if either the stretching or the ADC status is high. It means that ADC is converting for at least the duration  $\tau_{ADC}$  and will continue to convert, if, after time  $\tau_{ADC}$  elapses, the stretching indicator is still high. If the stretching indicator goes low, but the ADC is not done converting yet, it will continue to convert until time  $\tau_{ADC}$  elapses (until ADC status indicator goes low). During the period from the start of stretching to the end of conversion ( $\tau_{valid}$ ), the detector will not generate VEFs and pulse height data for the subsequent events.  $\tau_{ADC}$  has a nominal value of approximately  $12 \pm 1 \mu s$ . This value is defined by the internal ADC timer, which is connected to the 1 MHz clock. The  $1 \mu s$  uncertainty in ADC conversion time is associated with this clock.

While  $\tau_{ADC}$  is always approximately constant, the time the pulse is being stretched,  $\tau_{one-shot}$ , can be highly variable due to an unexpected behavior of the monostable one-shot. The one-shot, inside the Pulse Stretcher block, is responsible for stretching an incoming pulse to a certain width  $\tau_{one-shot}$ . It does not retrigger until its output returns to zero (the chip used in the USA electronics is a Signetics 74121 non-retriggerable one-shot). The monostable one-shot was designed to output a standard length pulse of about 16  $\mu\text{s}$  when triggered by a valid event. Tests on the brass board have shown that when the time between triggering pulses is large, the output pulse width is 15.6  $\mu\text{s}$ . This value was measured [24] for the USA brass board electronics. When there is a sequence of pulses entering the one-shot with a high duty cycle, the output pulse width is shortened. The 74121 one-shot used in the USA electronics is known for erratic behavior at high duty cycle [30]. The output pulse width shortening is due to the one-shot timing capacitor not having enough time to fully recharge at high duty cycles. The timer in this one-shot is based on the capacitor voltage. It takes some time for the capacitor to completely discharge after the one-shot is done firing. If the next pulse arrives within about 20  $\mu\text{s}$  later, it will take less time for the capacitor to charge due to its residual charge and thus a narrower width output will result. We have measured pulses as short as 5  $\mu\text{s}$  coming out of the one-shot. For this measurement, two pulses were put into two different X-ray wires on the brass board electronics delayed in time one with respect to the other. A range of time delays between pulses was tried, including a minimal time delay of  $\sim 2 \mu\text{s}$  between the end of the first pulse and the beginning of the second one. The second signal pulse triggered a shorter one-shot pulse, which was shortened by varying amounts depending on the time delay.

Figure 5.3 shows a summary of the measurements on the brass board one-shot, and a linear approximation to the values observed. This curve can be used to make a higher order correction to the deadtime model discussed in Section 5.4.1. (Note that in the case when  $\tau_{one-shot} < \tau_{ADC} + \tau_{coin}$ , the ADC can produce a wrong pulse height value since the input to the ADC goes to zero before ADC is done converting (there is no sample and

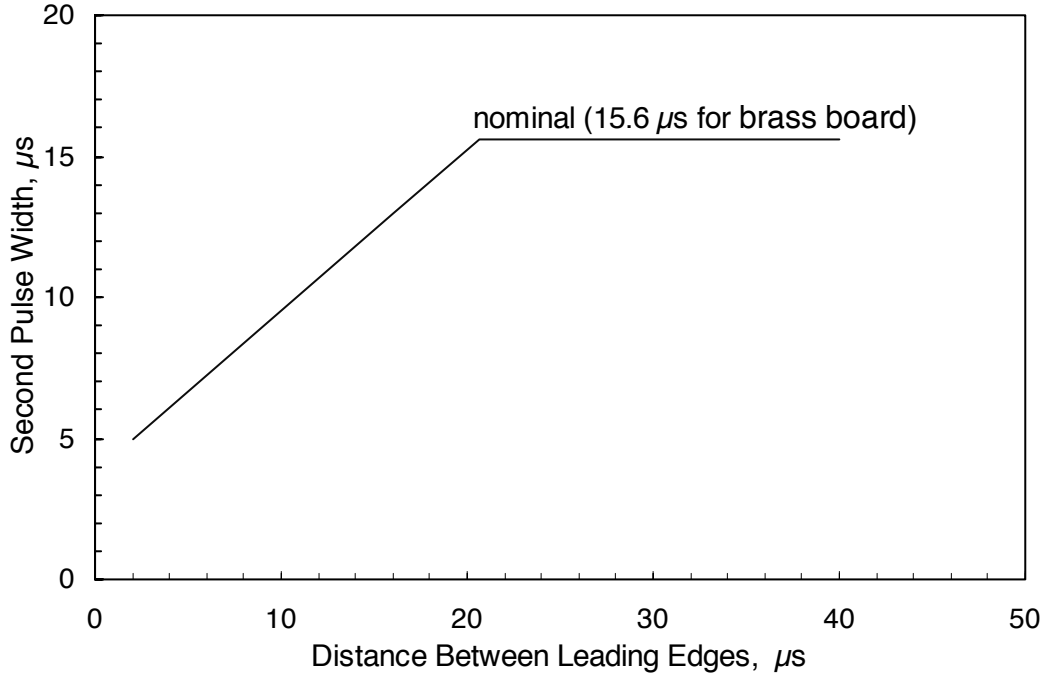


Figure 5.3 Width of the one-shot pulse as a function of the distance between incoming pulses.

hold on the input to the ADC). The specification for the conversion time for the first 7 bits is nominally 7  $\mu\text{s}$ . These 7 bits will have a correct value only if  $\tau_{one-shot}$  is greater than 10.5  $\mu\text{s}$ . At high temperatures specification for the conversion time is 15  $\mu\text{s}$  (9  $\mu\text{s}$  for the first 7 bits). Thus at higher temperatures the wrong energy readings will occur if  $\tau_{one-shot}$  is less than 12.5  $\mu\text{s}$ . The pulse height corrections have not been included in this work.)

Initially,  $\tau_{valid}$  was solely defined by  $\tau_{one-shot}$ . But very short pulses (with the width less than  $\tau_{ADC} + \tau_{coin}$ ) coming out of the Pulse Stretcher block into the ADC created a situation where the ADC failed catastrophically. This situation arose when the new pulse arrived at the ADC input while it was still converting the previous pulse. This condition locked up the ADC, and it could not subsequently output pulse height information. To fix the problem, the feedback between the Pulse Stretcher block and the ADC was added (the ADC status line in Figure 5.2). With the addition of the feedback, the ADC continues to

convert until finished, and does not accept a new pulse for the duration of  $\tau_{ADC}$  (during this time the ADC status stays high). This addition gave the deadtime,  $\tau_{valid}$ , the complicated nature described above.

In summary,  $\tau_{valid}$  deadtime is the longer of two times:  $\tau_{one-shot}$  or  $\tau_{ADC} + \tau_{coin}$ .  $\tau_{one-shot}$  is on average 15.6  $\mu$ s. Occasionally, in the case of pulses coming close together, the stretching time can decrease to as short as 5  $\mu$ s.  $\tau_{ADC}$  is  $3.5 \pm 1 + 12 \pm 1$   $\mu$ s, where 3.5  $\mu$ s is the time between event detection and start of the ADC conversion, 12  $\mu$ s is the nominal ADC conversion time, and 1  $\mu$ s is the uncertainty imposed by the clock. Thus,  $\tau_{ADC} + \tau_{coin}$  varies from pulse to pulse from 13.5  $\mu$ s to 17.5  $\mu$ s.  $\tau_{valid}$  varies from 13.5  $\mu$ s to 17.5  $\mu$ s as well, and can assume a number of values in between. For some exotic event sequences, it can be as short as 12  $\mu$ s or as long as 20  $\mu$ s. The deadtime model, to be discussed in Section 5.4.1, that assumes non-extended electronics deadtime of  $\sim 16.4$   $\mu$ s and effects of the DIB, agrees well with the calibration data.

If an event makes a signal in the perimeter wire, it causes the detector to be dead for the period of time  $\tau_{logic}$ . This deadtime is determined by the time that it takes the Digital Veto Logic and ADC Control block to process any event. If another perimeter wire event comes in within this time it will not be detected. If an X-ray wire event comes in within this time it also will not be detected, but it will start the Pulse Stretcher one-shot, causing the detector to be dead for an additional period of time of  $\tau_{one-shot}$ . It will not start the ADC conversion.

In the case of a coincidence event, the detector is dead for the period of time  $\tau_{one-shot}$ . The coincidence signal starts the one-shot but does not start the ADC conversion.

### **Detector Electronics Response to Large Events**

The other important issue in understanding the deadtime is whether the response of the



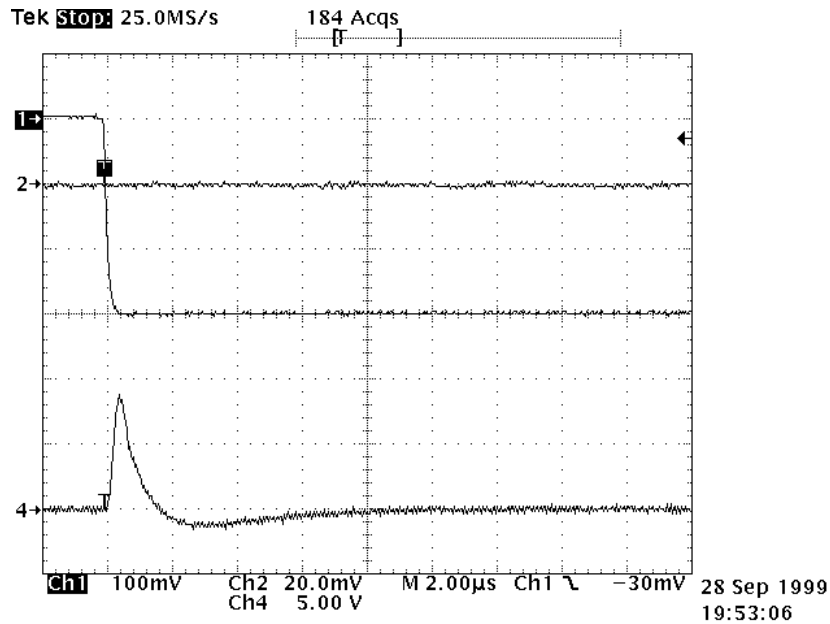


Figure 5.4 Amplifier input and output. Horizontal time scale is  $2\text{ }\mu\text{s}$  per division (10 divisions total). Value per division for each channel for the vertical voltage scale is indicated under the plot (8 divisions total). Channel 1: input pulse. Channel 4: pulse out of the amplifier. The amplifier is not saturated.

electronics depends on the energy of the X-rays. In particular, the response of the electronics to events with much larger pulse amplitude than nominal (high Z cosmic rays and high energy X-rays) needs to be addressed. Note that the amplitude of the pulse in the anode wire is linearly proportional to the energy of an event.

Tests on the ground were conducted to find out how the detector electronics response depends on the energy of the event. Sets of tests were performed with the USA brass board electronics in April 1998 by Gary Godfrey and Gayane Shabad and in September 1999 by Jim Ampe. For the details on the April 1998 tests see [24]. The results of both sets of tests are presented in this section. They are consistent with each other.

There was a concern that due to an overload of the circuit, large amplitude input pulses might cause the amplifiers to ring, producing a number of signals at positive voltage above the baseline. These positive signals might retrigger the discriminator and introduce additional bogus pulses. We did not detect any output ringing for input pulses as large as

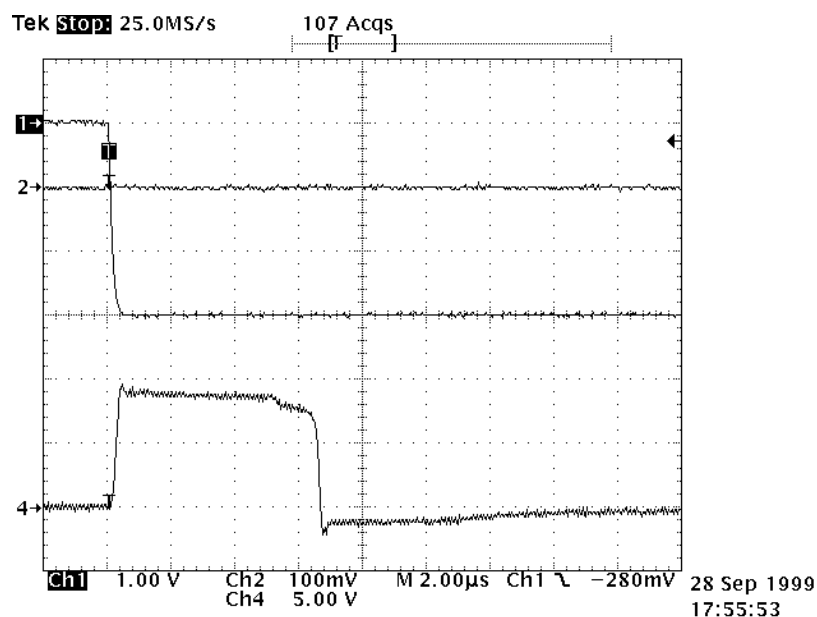


Figure 5.5 Amplifier input and output. Horizontal time scale is 2  $\mu$ s per division (10 divisions total). Value per division for each channel for the vertical voltage scale is indicated under the plot. Channel 1: input pulse. Channel 4: pulse out of the amplifier. The amplifier is saturated.

30 times the amplifier saturation value (the amplifier is saturated with 300 mV input pulses that correspond to approximately 20 keV energy events).

However, high Z events can affect the detector response in a different way. Figure 5.4 shows a typical waveform of a signal after going through the amplifier, when the amplifier is not saturated. The output pulse has a positive part (which is the polarity that the discriminators and ADC use) and a negative one (which has to do with the fact that the circuit is AC coupled and there must be equal positive and negative areas). The tail of the pulse approaches zero baseline. Figure 5.5 shows typical waveform of a signal after the amplifier when the input pulse is large enough to saturate the amplifier.

The large pulse from the high Z event on an X-ray wire causes a suppressed baseline on the signal out of the amplifier that goes to the one-shot. A pulse that arrives later on any X-ray wire rides on this suppressed baseline (see Figure 5.6). This second pulse might not pass the 0.14 V discriminator threshold or, if detected, might have a smaller pulse height

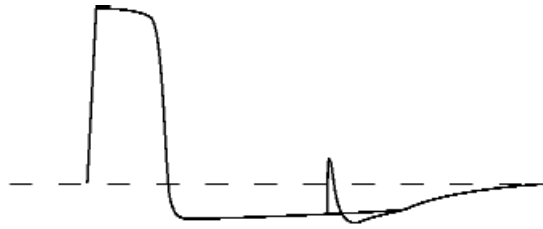


Figure 5.6 Amplifier output. The large signal out of the amplifier is followed by the nominal signal.

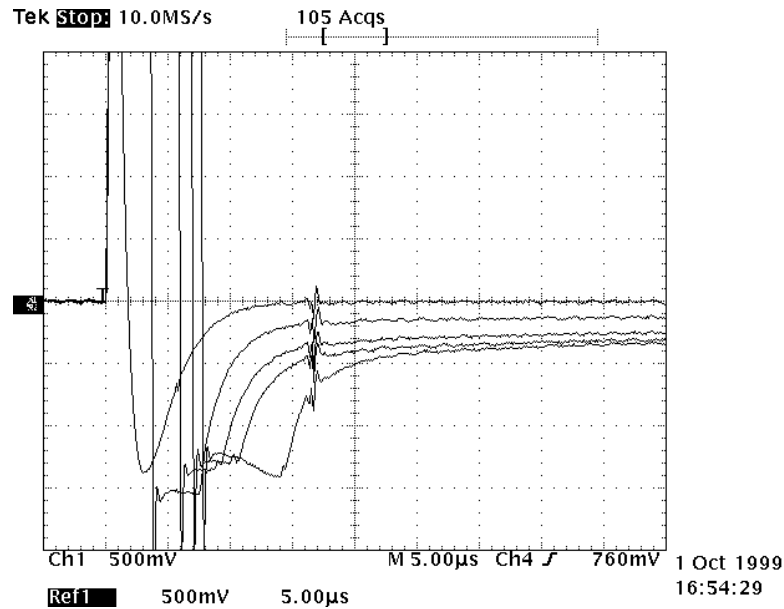


Figure 5.7 Amplifier output. Horizontal time scale is  $5\ \mu\text{s}$  per division (10 divisions total). Vertical voltage scale is 500 mV per division (8 divisions total). The negative tails of the output pulses are shown. Five waveforms correspond to five different input voltages. From top to bottom: input voltage is 300 mV (the amplifier reaches the saturation threshold at this input voltage); input voltage is 3 times the saturation threshold input voltage; 6 times; 10 times; and 30 times. Average of 64 acquisitions.

value. Sometimes, in order to be detected at all, the second pulse would have to arrive later, when the baseline had returned closer to zero. Thus, large pulses can introduce long periods of deadtime and decrease the energy of the events.

The value of the deadtime depends on the energies of the two consecutive events. The following figures help to characterize this effect. Figure 5.7 shows the amplifier output pulse shapes for various amplitudes of the input pulses from the external pulse generator. Figure 5.8 shows the negative tails on a finer voltage scale. From Figure 5.8 we can

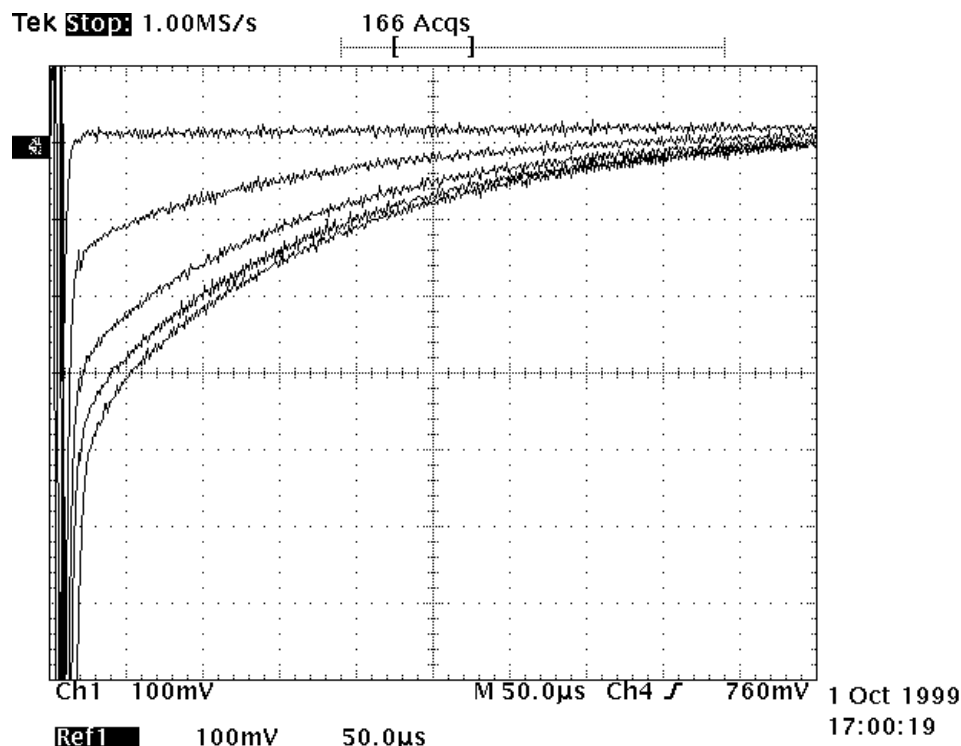
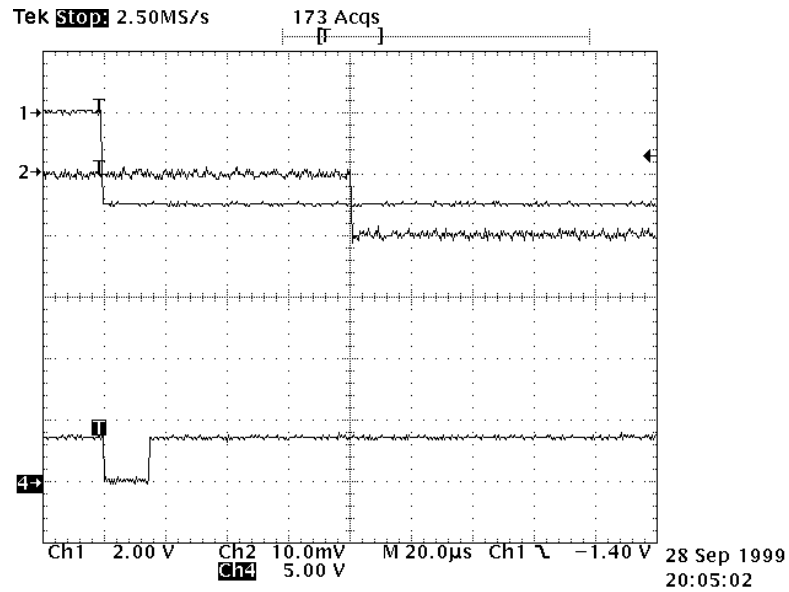


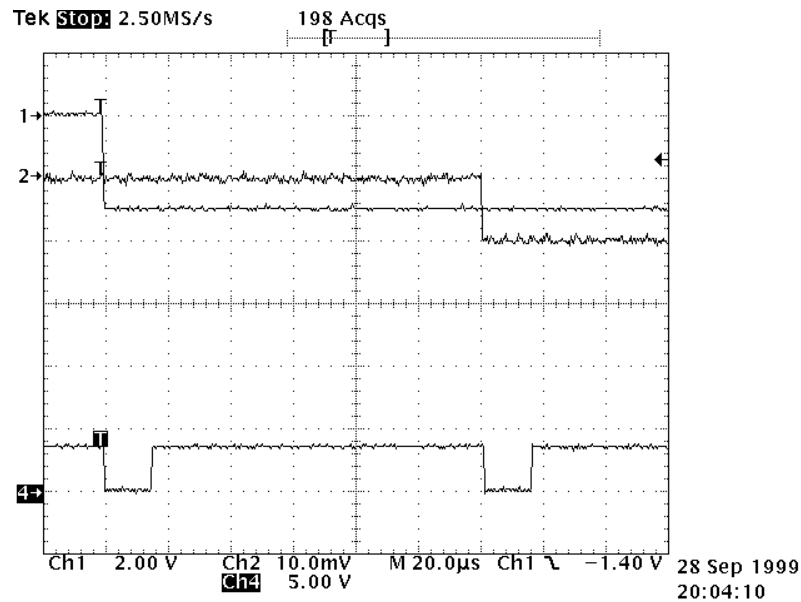
Figure 5.8 Amplifier output. Horizontal time scale is 50  $\mu$ s per division (10 divisions total). Vertical voltage scale is 100 mV per division (8 divisions total). The negative tails of the output pulses are shown. Five waveforms correspond to five different input voltages. From top to bottom: input voltage is 300 mV (the amplifier reaches the saturation threshold at this input voltage); input voltage is 3 times the saturation threshold input voltage; 6 times; 10 times; and 30 times. Average of 64 acquisitions.

estimate the value of the deadtime for two pulses with given energy. For example, if the amplitude of the first input pulse is 10 times greater than the saturation threshold value (or 3 V) and the amplitude of the following pulse is 10 mV (corresponding to 300 mV pulse out of the amplifier) then the second pulse will be detected if it arrives approximately 140  $\mu$ s after the first. The second pulse will be detected if it rises 140 mV (the value of the discriminator threshold) above zero baseline. Thus, to be detected, the second pulse has to arrive at the moment when the baseline from the first pulse is at -160 mV.

We confirmed that the deadtime indeed depends on the energy by generating two consecutive pulses and looking at the output of the one-shot. Figure 5.9 shows the one-shot stretching indicator for the case when the amplitude of the first pulse is 3 V and the



a) The second pulse is not detected with 95% probability when pulses are separated by  $80 \mu\text{s}$



b) The second pulse is detected with 95% probability when pulses are separated by  $120 \mu\text{s}$

Figure 5.9 One-shot output. Horizontal time scale is  $20 \mu\text{s}$  per division (10 divisions total). Value per division for each channel for the vertical voltage scale is indicated under the plots. Channel 1: large 3 V pulse into the amplifier (10 times input value that saturates the amplifier). Channel 2: small 10 mV pulse into the amplifier. Channel 4: one-shot stretching indicator.

amplitude of the second pulse is 10 mV. The time between the detection of the first pulse and the detection of the second varied in the 80-120  $\mu$ s range during the repeated measurements. This variation is due to electronic noise. The electronic noise cannot be seen in Figures 4.7 and 4.8, since they show the average of many acquisitions. The noise raises the amplitude of the second pulse, and the second pulse is detected closer to the first pulse than the estimated 140  $\mu$ s. Figure 5.10 shows the single acquisition of the amplifier output pulse in the case when the input pulse is 10 times greater than the saturation threshold value. The second 10 mV pulse will be detected 120  $\mu$ s after the first one.

The model describing deadtime as a function of the pulse height of the first and second pulses can be built based on the information presented in this section. The model should take into account the electronics noise.

The other effect introduced by large events is self-vetoing. The pulses with amplitudes 1.9 times the amplitude that saturates the amplifier and higher on an X-ray wire are not recorded by the data acquisition system. The explanation for self-vetoing, confirmed by the measurements, is that large pulses induce noise in the power supply line that triggers the signal wire discriminators, and thus the event is vetoed as a coincidence.

In summary, pulses with large pulse height (starting from approximately twice the amplitude that saturates the amplifier, which corresponds to  $\sim 40$  keV energy events) cause varying deadtime in the detector electronics. These pulses result mainly from high Z cosmic rays and some from high energy X-rays. The varying deadtime depends on the energies of both the large pulse height event and the subsequent event. The large pulse height events affect the pulse height values for the subsequent events. In addition, large pulse height events (with energy greater than  $\sim 38$  keV) will self veto and will not be detected in the data stream.

Careful comparison of the on-ground calibration data from the laboratory X-ray source

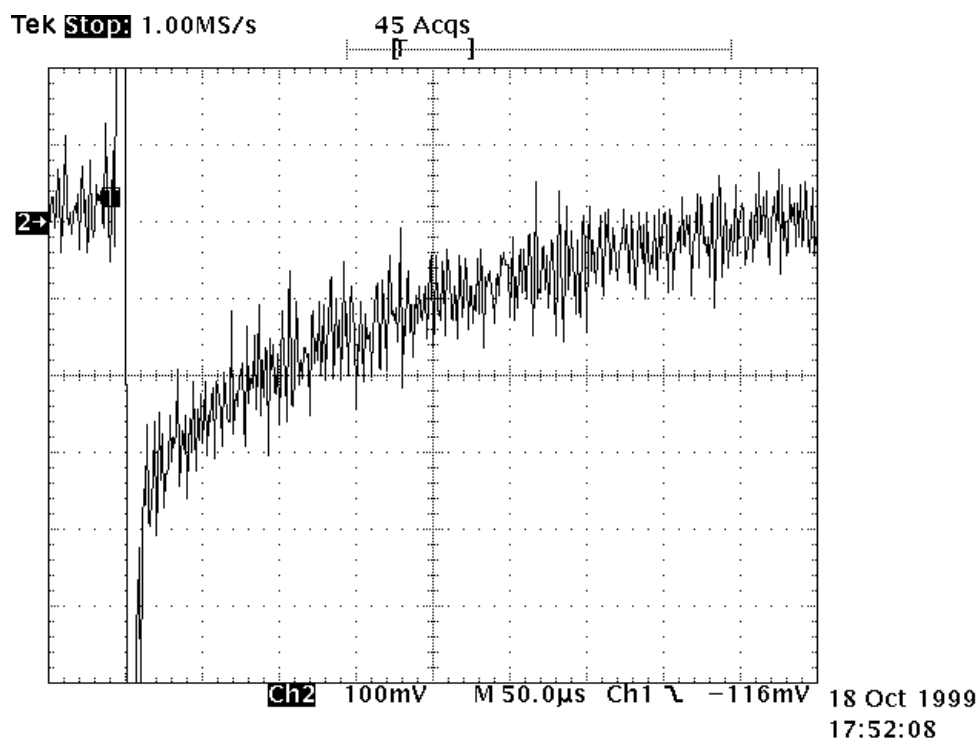


Figure 5.10 Amplifier output. Horizontal time scale is 50 ms per division (10 divisions total). Vertical voltage scale is 100 mV per division (8 divisions total). Negative tail of the output pulse with noise. The input voltage is 10 times the saturation threshold input voltage. Single acquisition.

(with no large energy background events present) with on-orbit calibration data will show how big these effects are.

### 5.1.2 Deadtime Effects Introduced by the Detector Interface Board

The Detector Interface Board (DIB) receives Valid Event Flag and pulse height data from the two proportional counters and processes it for the transmission to the spacecraft interface. Its function is to assign a time to a valid event, to match the pulse height value and the time value for the event, and to pass the correct word with the event information to the Central Processing Unit (CPU).

We found, during the calibration tests, that sometimes the DIB introduces timing distortions. One idiosyncrasy we found was a small fraction of same time events (STE) in all of the calibration data files. STE are sequential events that have the same time stamp

values. However these events can be distinguished as they have correct energy values. We have measured that for two events that have the same time, the first one is assigned the time stamp of the second and the second one has the correct time stamp. This idiosyncrasy affects the event time interval distribution by introducing data in  $0^{th}$  bin (events with zero time intervals between them, see Figure 5.16). It affects the power spectrum as well since some fraction of the events has incorrect times. Below we provide a schematic explanation for how the DIB handles the science events and a model for the STE idiosyncrasy.

Figure 5.11 illustrates how the DIB handles a science event. The DIB is connected to the detector electronics with a physical line from each detector signaling that it has received an X-ray. The DIB is also connected to the ADC Mux Board. This board is a part of the central electronics and there is only one board for both detectors. The ADC Mux board provides the electrical interface between the DIB and the X-ray detectors. The board implements the serial transfer of the data to and from both detectors.

When a science event occurs in a detector, the DIB receives a VEF signal from that detector. The detector also sends pulse height data through the serial port to the ADC Mux Board. The ADC Mux Board processes the 8-bits of serial ADC data into a parallel data format. The DIB also receives an interrupt from the ADC Mux Board signaling that there is pulse height data to be read, with a time delay of approximately  $16\ \mu\text{s}$  after it receives the VEF (see Figure 5.12a).

The DIB has hardware buffers for storing the VEF (timing) interrupts, pulse height interrupts, and the arrival time values of the VEF. There are two buffers of each type (one for each detector). The size of the buffer for the VEF and the pulse height interrupts is 1 bit. The size of the buffer for storing the event time value is 24 bits. The ADC pulse height values are stored in the two hardware 8 bit buffers (one for each detector) on the ADC Mux Board.



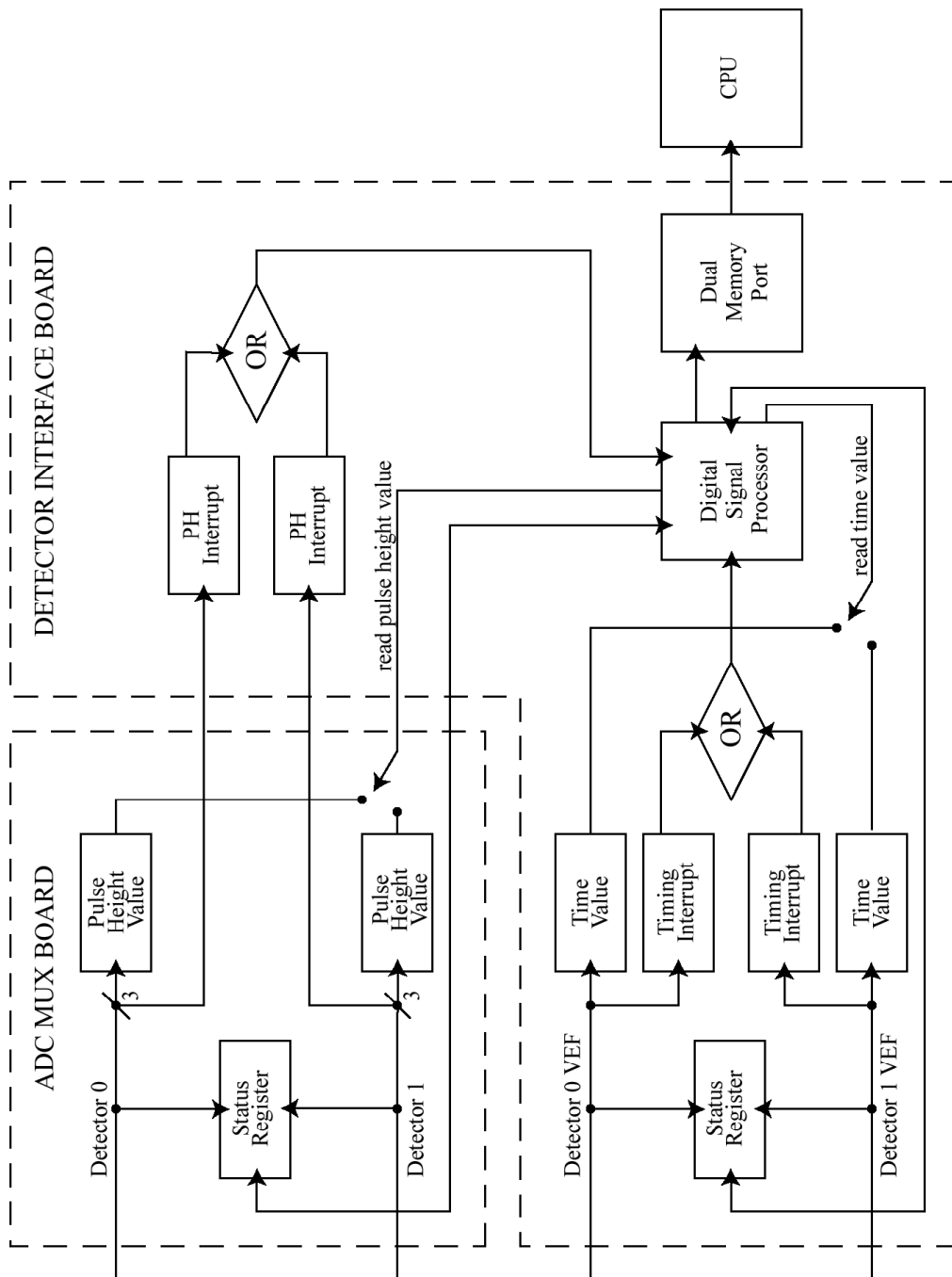


Figure 5.11 Diagram of the DIB event processing. Currently only detector 0 is functioning in orbit.

The DIB also has separate software buffers inside the local DIB RAM for storing the arrival time values of the VEF and pulse height interrupts. There are two buffers of each type (one for each detector). The event words with matched time and pulse height information are stored inside the Dual Memory Port on the DIB. The Dual Memory Port can store 2047 event words.

Both the ADC Mux Board and the DIB have status registers that contain information about which detector caused a particular interrupt.

The DIB Digital Signal Processor (DSP) receives a highest-level priority interrupt when there is one or more VEF interrupts in the interrupt buffers. VEF interrupts have higher processing priority over the pulse height interrupts. Interrupts generated from the two timing interrupt buffers are logically ORed and applied to the DSP. Upon the DSP receiving the interrupt, it first reads the status register to determine which detector caused the interrupt. It then reads the appropriate hardware time value and puts the value in a software buffer in the DIB RAM. It takes the DSP a few microseconds to execute the interrupt routine (see Figure 5.12a). The execution time depends on how busy the DSP is servicing various software tasks. This time will vary from event to event depending on the rate and the time separation. During the time the DSP is processing an interrupt it does not recognize any other interrupts. After the event time is read out the time interrupt is cleared from the hardware buffers. The time value will be overwritten in the hardware when the next event comes in.

The DSP receives a second priority interrupt when one or more science pulse height datum is received by the ADC Mux Board and is ready to be read. The two pulse height interrupt signals are logically ORed and applied to the DSP. Upon receiving the interrupt the DSP masks all other hardware interrupts. The DSP determines the time of the pulse height interrupt and stores this time value in the software buffer in the DIB RAM. The DSP reads a status register located on the ADC Mux board to determine which detector produced the pulse height data. The DSP then reads the particular pulse height data and combines it with the time value stored in the software buffer. The DSP then generates a

correctly formatted pulse height/time word, which is stored in the Dual Port Memory on the DIB. The execution time for the DSP to process one pulse height value is on the order of a few microseconds (see Figure 5.12a). As with the timing interrupt, the execution time depends on how busy the DSP is servicing various software tasks, and will vary from event to event depending on the rate and the time separation. During this time the DSP does not recognize any other interrupts. Reading the pulse height value clears the pulse height interrupt from the hardware buffer. The pulse height value will be overwritten in the hardware when the next event comes in.

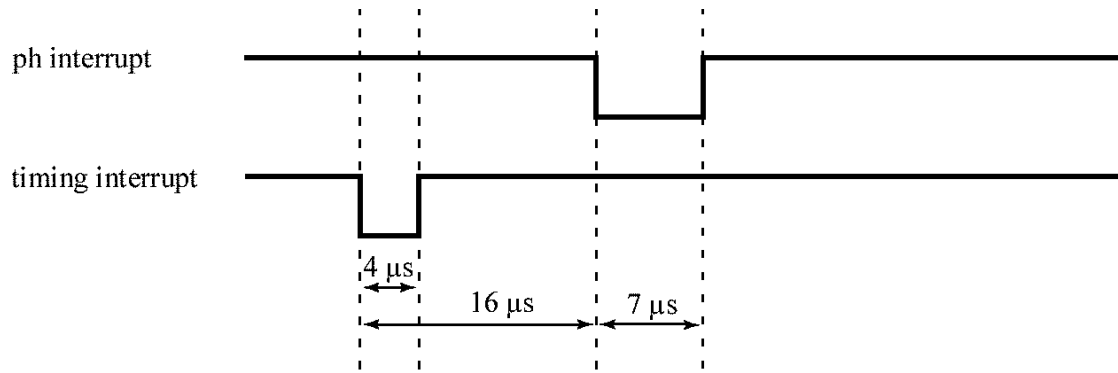
If the DIB receives interrupts from two detectors at the same time it first services the interrupt from detector 0 and then the one from detector 1.

When the DSP reads the pulse height value, it compares the time of the event with the time at which the pulse height value has been read. If the time difference is greater than the preset DIB resync time (currently 40  $\mu$ s on orbit, but reprogrammable) than the event time value and pulse height are assumed to be out of synch and the event is discarded.

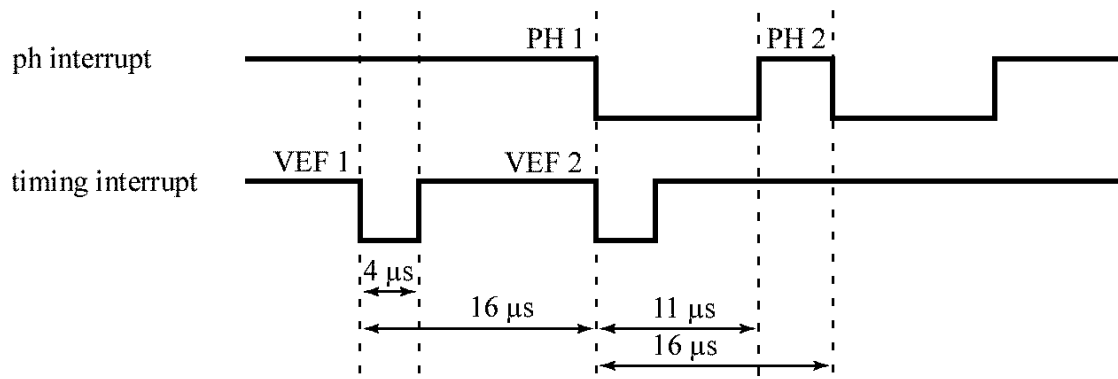
The CPU board reads out the DIB Dual Port Memory for the event words once every second.

Two photons will have the same time value in the data stream if the VEF interrupt from the second event is executed by the DSP before the pulse height interrupt from the first event. In particular this scenario always takes place when the two events come close together. This fact was verified by the measurements with the USA brass board electronics.

Figure 5.12b shows the pulse height and the timing interrupts in the case of two events coming into the detector 16  $\mu$ s apart. The DSP executes the first VEF interrupt and writes the time value into the DIB RAM. The next interrupt the DIB executes is also the VEF interrupt from the second event. The DIB writes the time value of the second event into the DIB RAM overwriting the time value from the first event. Then, the DSP receives a



a) Single event



b) Two events 16 μs apart

Figure 5.12 Timing profiles of pulse height and timing interrupts.

pulse height interrupt from the first event. The pulse height value from the first event is matched with the time value of the second event and written into the Dual Memory Port. When the DIB receives the second event's pulse height interrupt, the second pulse height value is matched with the second event's time value and is written to the Dual Memory Port. Thus, in the end, the two photons in the data have the same time value (with the first event having the time of the second) and the correct pulse height value.

The result of the measurements showed that the two events have to arrive at most 17 μs

apart for this scenario to happen. This is the time between the VEF interrupt and the moment when the pulse height interrupt masks all the other interrupts. The actual time is between 17  $\mu$ s and 18  $\mu$ s, but since the VEFs come into DIB with 1  $\mu$ s resolution, we use 17  $\mu$ s time for simulating the DIB performance. Occasionally, during the tests with high-count X-ray source some events separated by 17  $\mu$ s made it to the final data stream (less than 0.001%). This shows that this time can vary depending on the number of commands the DIB performs between the VEF interrupt and the moment when pulse height interrupt masks all the other interrupts. However, this happens infrequently, and a model that assumes exactly 17  $\mu$ s describes STE's well.

At high counting rates, some valid events might be lost and not written into the science frame due to the fact that the DSP takes time to process interrupts. While the DSP is executing interrupts, the time and pulse height values can be overwritten by subsequent events. This might introduce additional DIB deadtime at high rates. The question of whether all of the valid events are written into the science frame needs further study. The most significant loss of events would be expected during operation with high rates in both detectors. During the on-ground calibration, the performance of the DIB for comparably high rates in both detectors was not studied. The experimental setup allowed us to achieve a high rate from the calibration source in only one detector at a time. Since one detector was lost early in the mission, the question on how the DIB handles data from both detectors is not important anymore. However, there is a possibility that even with one detector in operation at high rates the DIB introduces event loss (i.e. deadtime). The deadtime model developed in Section 5.4.1 slightly underestimates real deadtime (see discussion in Section 5.4.6). That might be an indication that real deadtime is bigger due to the loss of events in the DIB.

### **5.1.3 Conclusions**

Due to the effects discussed above, a single non-extended deadtime number cannot characterize the USA electronics and DIB deadtime.

In summary, those effects are: 1) The erratic output signal length of the detector electronics monostable one-shot for events that are close in time. This effect becomes more frequent in the data stream for higher rates. 2) The existence of the parallel data path for the perimeter and coincidence veto signals. The perimeter and coincidence veto events introduce different deadtime (typically shorter) into the detector than the photon signal events, and thus affect the event Poisson process. The size of this effect depends on the perimeter and coincidence veto rates, and valid event rates. 3) A dependence of deadtime on energy. Very large pulse heights can cause longer than nominal deadtime in the detector. In this case the value of the deadtime depends on the energy of the large pulse height event and the event that follows, and on the large pulse height event rate, as well as all other rates in the detector (perimeter and coincidence veto, and valid events rate). 4) STE. The way STE affect timing depends on the values of all the rates in the detector. 5) Potential loss of events by the DIB. 6) The energy-dependent instrumental effect discussed in Section 5.5.

During on-ground timing calibrations only effects 1), 4), 5), and 6) come into play. Since there is a very low background rate on the ground, effect 2) is very small. There are also no very large events on the ground, so 3) is not present. On-orbit, all the effects will be present.

In Section 5.4 we describe a model, that accounts for STE events and assumes a simple non-extended deadtime for the USA electronics, and a phenomenological approach for describing the above effects for on-ground calibration data, i.e., parameterizing the power spectra of the Poisson calibration data. In this Section we also describe the results of the on-ground calibration and provides recipes for correcting the science data for deadtime effects. To estimate the magnitude of effects 2) and 3) on the data, the power spectra obtained from on-orbit Poisson data (e.g., Crab or Cas A data) should be compared with the power spectrum from the on-ground data. We discuss effect 6) in Section 5.5.

Mode Number	Mode Type	Time Resolution	Number of Spectral Channels	Number of Bits per Event	Layer ID	Detector ID	Telemetry Rate (kbps)
1	event	32 $\mu$ s	16	12	yes	yes	40
2	event	32 $\mu$ s	16	12	yes	yes	128
3	event	2 $\mu$ s	8	15	yes	yes	40
4	event	2 $\mu$ s	8	15	yes	yes	128
5	binned spectral	10 ms	48	192 per spectrum	no	yes	40

Table 5.1 Description of the USA science data modes. For the details refer to [104] and [28].

## 5.2 USA Data Analysis Issues

In this section we discuss specifics of the USA data relevant to the timing analysis.

### 5.2.1 Standard Data Modes

The Detector Interface Board processes data for the transmission to the spacecraft interface. The Digital Signal Processor on the DIB performs data formatting into a particular data mode. The representation of information transmitted about the events depends on the DIB mode. There are five science-telemetry DIB modes currently implemented for the USA mission: four event modes and one spectral mode.

The event mode contains information about individual photons with bits allocated for time stamp, spectral channel value, detector ID and layer ID. The timing resolution and number of spectral channels vary for the four different event modes. The detector ID is the number of the detector, which is recorded for each event and can have a value of either 0 or 1. The layer ID determines what layer of the proportional counter the signal was detected in and can have a value of either 0 or 1.

In spectral mode, the data is binned every 10 ms into two 48 channel spectra (one for each detector). There is no information about individual events. USA has two telemetry rates available. The standard rate is 40 kbps. The high telemetry rate (or high-bit rate) is

Mode Number	Telemetry Rate	Asymptotic Maximum Number of Events in a Frame	Break Rate (Hz)
1	low	3070	~1350
2	high	9950	~8000
3	low	2456	~1100
4	high	7960	~6500
5	low	20000	20000

Table 5.2 Asymptotic maximum number of events one science frame can hold and break rates. The rates in the last column are approximate (rounded to the nearest 100) average rates over 100 simulations of a Poisson process.

128 kbps. The spectral mode is not used at high-bit rates. There are two high-bit rate event modes and two low-bit rate event modes. Table 5.1 gives the summary of the USA data mode properties.

The best timing resolution USA can achieve is 2  $\mu$ s in modes 3 or 4.

The science data from USA is packed into science data frames. USA produces one science data frame every second. Each frame contains housekeeping data (instrument, pointer, and spacecraft status information) and the event data. The data from the two detectors is written into one frame.

In the event mode the arrival time of an X-ray is recorded as an elapsed time since the beginning of the frame. The internal USA clock provides this time in 1  $\mu$ s ticks. The time of the beginning of the current frame is acquired from the Global Positioning System (GPS) or Space Vehicle Clock (if the GPS time is not available), and stored in the housekeeping data. In the event mode, the bits of the event word are distributed throughout the frame to avoid writing common time bits for many events. For the detailed information on how the event words are packed within the science frame see [104] and [28]. Each event mode can hold limited number of events.

The spectral mode can hold all of the events up to the maximum incident counting rate



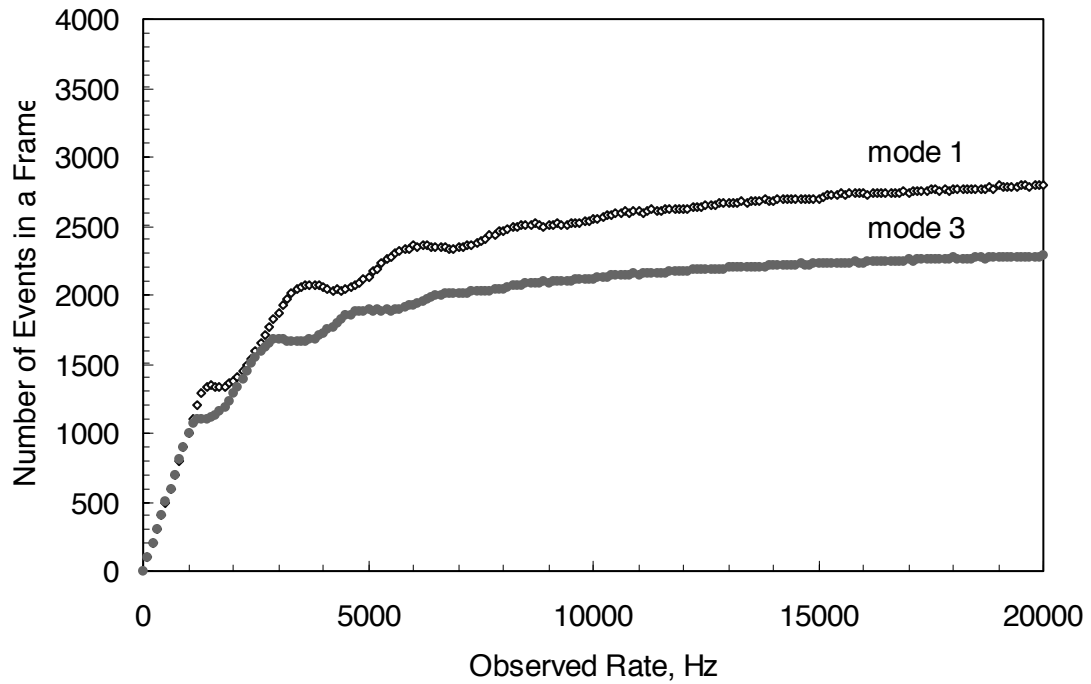


Figure 5.13 Average number of events held in one frame versus observed counting rate for a Poisson event distribution with non-extended deadtime. Each data point is an average of 100 simulations. Low-bit rate modes.

allowed in USA (10 kHz in one detector).

If during an observation the observed source rate exceeds the amount of data the particular mode can hold per second, a portion of the data will be lost and there will be gaps in the source light curves. Table 5.2 shows the asymptotic maximum number of events the science frame can hold in a particular mode. This number is obtained assuming that every available slot in the science frame allocated for the event word is filled. However, the actual number of the events written into the science frame depends on the distribution of the times of photons emitted by the source, on the source counting rate, and on the data mode. Figure 5.13 and Figure 5.14 show the average number of events one science frame holds as a function of the observed rate in both detectors. These results were obtained by Paul Hertz by simulating the USA science frame packing. The

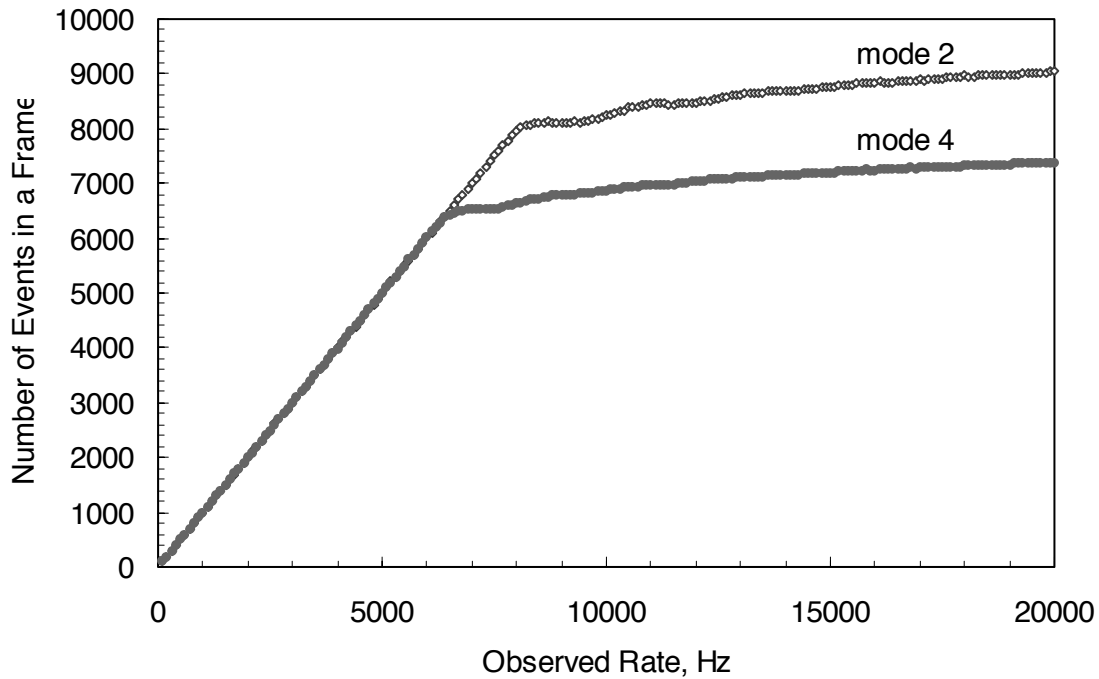


Figure 5.14 Average number of events held in one frame versus observed counting rate for a Poisson event distribution with non-extended deadtime. Each data point is an average of 100 simulations. High-bit rate modes.

simulation assumed a pure Poisson distribution for the incoming events. Each data point is an average of 100 simulations.

As the source rate increases, at some point the loss of events starts. The last column of Table 5.2 shows the average observed rates where losses begin assuming a pure Poisson process. These “break” rates should be kept in mind when choosing the observation mode for a particular source in order to avoid gaps in the light curve. However, since most X-ray sources are not Poisson sources and since there are deadtime effects in the detector, these values only serve as approximate guidelines for real sources.

### 5.2.2 Timing Idiosyncrasies

This subsection addresses the timing peculiarities of the USA data we have observed so far. Corrections should be made for these effects when a thorough timing analysis is

done, in particular when performing a Fourier power spectrum analysis on the data. Ignoring these issues will likely introduce artificial power into the power spectrum.

### **Same Time Events**

A fraction of contiguous events in the USA data stream have the same time values. These events are physically different events that are assigned the same time value by the detector. They have the correct energy value. The first event in a pair arrives earlier than the second, but has the time value of the second event.

This error in timing is introduced by the DIB (discussed in Section 5.1.2). The fraction of these events in the data depends on the rate (for 4100 Hz observed rate from the X-ray calibration source, it is 0.5%). In Section 5.4.1 we discuss how these events affect the time interval distribution and the power spectrum of the data.

Any serious timing analysis should correct for the STE. Note that these events can only be distinguished in the 2  $\mu$ s resolution modes. In the 32  $\mu$ s resolution data modes they are indistinguishable from the events that come less than 32  $\mu$ s apart. However, even when they are indistinguishable, the STE still disturb the original timing of the X-rays. Note also that they cannot be easily corrected by subtracting 17  $\mu$ s from the second event in a pair and assigning this time to the first. Because of the 2  $\mu$ s resolution in the final data stream, all we know is that the first event came either 16  $\mu$ s or 18  $\mu$ s earlier than the second.

### **Data Loss at High Counting Rates**

As discussed in Section 5.2.1, at high source rates the USA science frame fills up in less than a second. In the remainder of the second, the detector has no space to record the remaining events, which results in their loss. The light curve of a source with one-second binning will thus have gaps at the end of each second. The rate at which the light curve

starts to have gaps depends on the data mode and the statistics of the process. For a Poisson process, the values of break rates are listed in Table 5.2.

When performing an FFT analysis on data with gaps in the light curve, one has to account for this effect. For the studies of spectral power at frequencies higher than 1 Hz the FFT can be performed on the data segments within one frame with no gaps in them. The resulting Fourier power will be the average over all such segments.

### **Small Gaps in the Beginning of the Science Frame**

Under certain circumstances, USA data has small (on the order of several milliseconds) timing gaps at the beginning of science frames. Currently, we do not understand the cause of these gaps.

The gaps are present both when the science frame is filled up and when there is no science frame overflow. When there is no overflow, the gaps in the beginning seem to be contained within one millisecond. In the case of the overflow, the gaps are on the order of several milliseconds. The gaps are observed both in on-ground and on-orbit data.

More studies need to be done to find the exact value of the delay in the beginning of the frame and to answer the question of whether the delay is rate-dependent.

When performing an FFT on the USA data, one has to pay attention to the millisecond gaps in the beginning of the science frame.

### **One second of data missing**

During each ground station pass, a record (logbook) containing information on USA pointing and counting rate replaces one second of science data. Thus, over the course of a day, several seconds will not contain event information (they will be empty). Also, some of the frames will be empty due to the checksum error (the data analysis software outputs an empty frame if it detects a checksum error).

$t_b$ ( $\mu$ s)	$N$	$T$ (s)	$f_N$ (Hz)
32	$2^{13}$	0.262	15625
96	$2^{12}$	0.393	5208
960	$2^8$	0.246	521

Table 5.3 PSD parameters used for the calibration data analysis.

### 5.2.3 Fourier Power Spectral Density Analysis of the On-Ground Calibration Data.

In this section we discuss how the effects described in Section 5.2.2 were taken into account for the power spectrum analysis of the USA calibration data. We performed the FFT (4.1) on the data. The power spectrum is normalized using the Leahy normalization (4.2).

For the analysis, the data is divided into equal time segments of length  $T$ . Each segment is divided into  $N$  bins of size  $t_b$  ( $T = Nt_b$ ). The Fourier power spectra are then calculated for each of these segments and averaged over the number of segments. After averaging, the resulting power spectrum is normalized with the Leahy normalization (4.2), where  $N_{ph}$  is an average number of photons in one segment of length  $T$ .

Table 5.3 shows the values of parameters  $N$  and  $t_b$  used for calibration data power spectrum calculations and corresponding Nyquist frequencies  $f_N = 1/2t_b$ .

For the power spectrum analysis the STE were left intact in the data. The results of the power spectrum analysis of Section 5.4 are only applicable to the data not corrected for the STE.

For all the data in all modes we threw away two photons in the beginning and two at the end of the frame. At the time the data analysis software sometimes introduced events with wrong times near the frame boundaries. This problem has been fixed in recent versions of the data analysis software.

The way calibration data is divided into equal segments is different for high-bit rate and low-bit rate data modes. For high-bit rate modes 2 and 4 the data was considered continuous (with no gaps in it) and continuously divided into equal data segments. There were no filled up science frames in modes 2 and 4 for the rates observed during on-ground tests.

For low-bit rate modes 1 and 3 the data was divided into equal one-per-frame segments contained within the boundaries of the science frame. Each segment started in the beginning of the frame and ended before the start of the gap in the science frame (the gap results from the filling of the science frame). Also, the segments started 10 ms from the start of the frame to avoid the few millisecond gaps at the beginning where data loss occurs (Section 5.2.2). (If the segment starts right at the beginning of the frame, it results in an artificial increase of the Fourier power at lower frequencies).

## **5.3 USA On-Ground Calibration Tests**

### **5.3.1 Thermal Vacuum Tests**

On the ground, several thermal vacuum tests were performed on the USA detectors. The purpose of these tests was to simulate closely the thermal conditions in space and check the performance of the detectors. The detectors were put into the thermal vacuum chamber with vacuum pressures below  $10^{-6}$  torr. The temperature inside the chamber was cycled between cold and hot, while allowing the detectors to stay for long periods of time at the cold and hot plateaus. The high-count  $^{55}\text{Fe}$  X-ray source was used to calibrate the detector.

Overall, four complete thermal vacuum tests were performed from 1996 to 1998: in April and June of 1996 at NRL, and from August to October of 1997 and June 1998 at Boeing. In addition, preliminary tests in the vacuum chamber without thermal cycling were made at NRL in December 1995 and February 1996. The same X-ray calibration source was used for all the tests, and the counting rate dropped significantly over these years due to the 2.79 year half-life of the  $^{55}\text{Fe}$  source.

The December 1995 and February 1996 tests were conducted at the Naval Research Laboratory (NRL). In December only detector 0 was tested, and both detectors were tested in February. The tests were done in a small vacuum chamber without thermal cycling. The USA DIB was not used in those tests. Instead, timing data was read out with the temporary data acquisition system that allowed for 0.1  $\mu\text{s}$  timing resolution.

The April 1996 and June 1996 thermal vacuum tests were conducted at the A59 thermal vacuum facility at NRL. By that time, USA was completely integrated and all the systems were tested in the thermal vacuum chamber.

The final thermal vacuum tests of August-October 1997 and June 1998 took place at the Boeing Seal Beach facilities. The ARGOS satellite, USA aboard, was put in the thermal vacuum chamber with all the experiments assembled on the satellite.

The temperature cycle ranges measured in the detector body were from  $-15^{\circ}\text{C}$  to  $50^{\circ}\text{C}$  for the NRL tests and from  $0^{\circ}\text{C}$  to  $24^{\circ}\text{C}$  for the Boeing tests.

This report contains the analysis of the data collected during the last two tests at Boeing. We recommend that the earlier data be used with discretion. During the two early NRL tests the detectors were not integrated together and did not have the DIB attached. During the last two NRL tests major changes were made to the DIB software to correct problems found in the test. Thus, the timing properties of the data are not characteristic of the current state. Two hardware changes were made that affect the USA deadtime. After the December 1995 test the feedback loop between the ADC and the pulse stretcher was

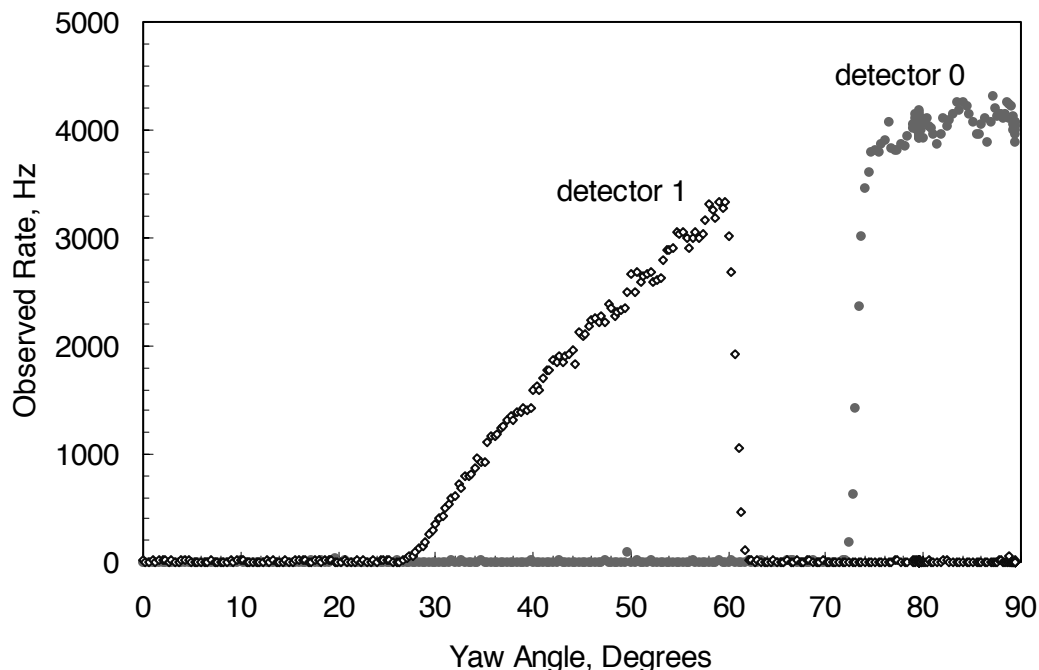


Figure 5.15 Observed counting rate from the X-ray source as a function of yaw angle. Curve on the left corresponds to the rates observed in the detector 1 and on the right in the detector 0.

added to avoid ADC lockup (see Section 5.1.1). After the June 1996 test a hardware fix was made to the perimeter veto logic. Prior to the fix the data collected during the April and June 1996 tests had a distorted timing distribution in cases when the perimeter veto rates were high.

There was no major hardware or software change introduced during or after the last two thermal vacuum tests at Boeing that affected the USA deadtime, thus the data from these tests was used for the final calibration analysis.

The X-ray calibration source used for all the tests was an  $^{55}\text{Fe}$  point source with a 2.74 year half-life. The energy of the emitted X-rays is 5.9 keV. The maximum observed counting rate in one detector from the X-ray source was greater than 10 kHz during the first December 1995 test and 3200 Hz during the last June 1998 test. In the December 1995 and February 1996 tests the X-ray source was placed directly on top of the USA collimators. Sometimes the source was attenuated with aluminum foils to obtain a



reduced value of the counting rate. For all the other tests the source was mounted to the USA yoke

The change of the yaw angle during the experiment allowed us to achieve various counting rates. When the detector rotated in yaw the collimators were exposed to the different fractions of the source active area, and therefore the rate was angle-dependent. As the yaw changed, the source was first seen by detector 1 at lower rates and then by detector 0 at higher rates. Figure 5.15 shows the observed counting rate as a function of yaw rotation angle for the August 97 thermal vacuum test. Only one detector was activated by the X-ray source at a time.

### **5.3.2 Description of the Data Used for the Analysis**

The data used for the analysis presented in this report was taken during the August-October 97 and June 98 thermal vacuum tests. The data covers all four event modes at various observed rates. Table A.1 in the Appendix gives the summary of the analyzed data. Cuts were applied to the data to insure data quality. The analyzed data segments have constant rate, i.e. the detector was not moving and the high voltage was steady.

## **5.4 USA On-Ground Calibration Results**

This section presents calibration results for both USA detectors. The results for the surviving detector 0 should be used in future data analysis. The results for detector 1 are important, since they can be used to predict the behavior of the detector at low rates (the low rate data was collected from detector 1 and the high rate data from detector 0).

### **5.4.1 Deadtime Model**

In this section we present a deadtime model that describes the time-interval distributions and power spectra of the calibration data. Although this model is not an exact representation of all the deadtime processes in the detector, it explains the overall timing effects seen in the data.

The detector electronics and the DIB introduce deadtime effects in USA (for the detailed discussion, see Section 5.1). The detector electronics introduce a complex deadtime that cannot be described by a simple non-extended or extended model. The DIB further disturbs the timing stream by producing same time events (STE).

In summary, the detector electronics deadtime is the longer of the two times: the pulse stretching time and the ADC conversion time counted from the first instant of event detection. The pulse stretching time is nominally  $15.6\ \mu\text{s}$ . Occasionally, in the case of pulses coming close together, the stretching time can decrease to as short as  $5\ \mu\text{s}$  (see Figure 5.3 for the dependence of the pulse stretching time on the distance between event pulses). The ADC conversion time counted from the moment of event detection is  $3.5 \pm 1 + 12 \pm 1\ \mu\text{s}$ , where  $3.5\ \mu\text{s}$  is the time between event detection and start of ADC conversion,  $12\ \mu\text{s}$  is the nominal ADC conversion time, and  $1\ \mu\text{s}$  is the uncertainty imposed by the clock. Thus, this time varies from pulse to pulse from  $13.5\ \mu\text{s}$  to  $17.5\ \mu\text{s}$ . However, the actual mechanism of the electronics deadtime is subtler and is described in detail in Section 5.1.1.

The overall behavior of the USA electronics deadtime is close to non-extended, since, for the majority of events, an event arriving while the detector is dead has no effect. For our on-ground model, we assumed that the deadtime introduced by the electronics is non-extended. The value of the deadtime is a parameter of the fit to the experimental data. The model does not take into account the effect of coincidence or veto events, since these rates were insignificant in the on-ground experiments. In space, high  $Z$  charged particles and other background rates modify this simple behavior.

The events in the model are simulated from a Poisson distribution with a fixed non-extended deadtime. The event times are rounded to emulate the  $1\ \mu\text{s}$  timing accuracy of the electronics clock. All events that occur less than or exactly  $17\ \mu\text{s}$  apart are assigned the same time; specifically, the first photon gets the time of the second. This mimics the DIB action on the event stream (Section 5.1.2). Note that introducing STE into the data

does not change the original counting rate. Afterwards, the 2  $\mu\text{s}$  data mode timing resolution is simulated.

We need to use a simulation since, due to the finite timing resolution of 2  $\mu\text{s}$ , it is impossible to reconstruct exactly the correct time of the first photon in the STE pair. All

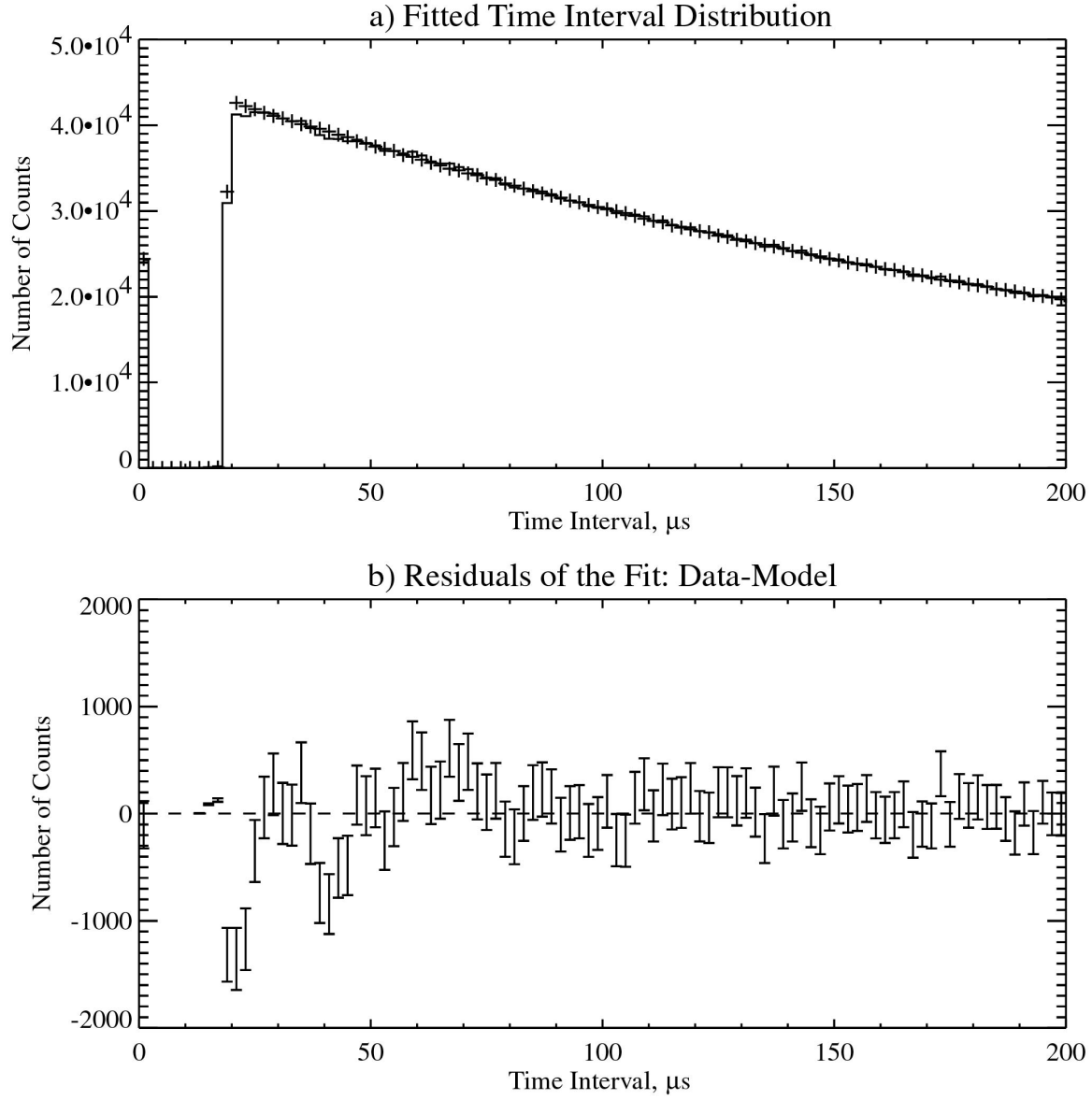


Figure 5.16 The deadtime model fit to the time interval distribution. a) Histogram of the time interval distribution of the detector 0, mode 3 data (5 million events). Crosses represent the model (50 million events). Deadtime  $\tau=16.368 \mu\text{s}$ , bin size:  $t_b=2 \mu\text{s}$ ,  $r_o=4075 \text{ Hz}$ .  $\chi^2=1.707$  (dof=494).

The  $0^{th}$  bin contains the same time events. b) Difference between the data and the model. Range up to  $200 \mu\text{s}$  is shown as the most interesting. There are no deviations of the model from the data beyond this range.

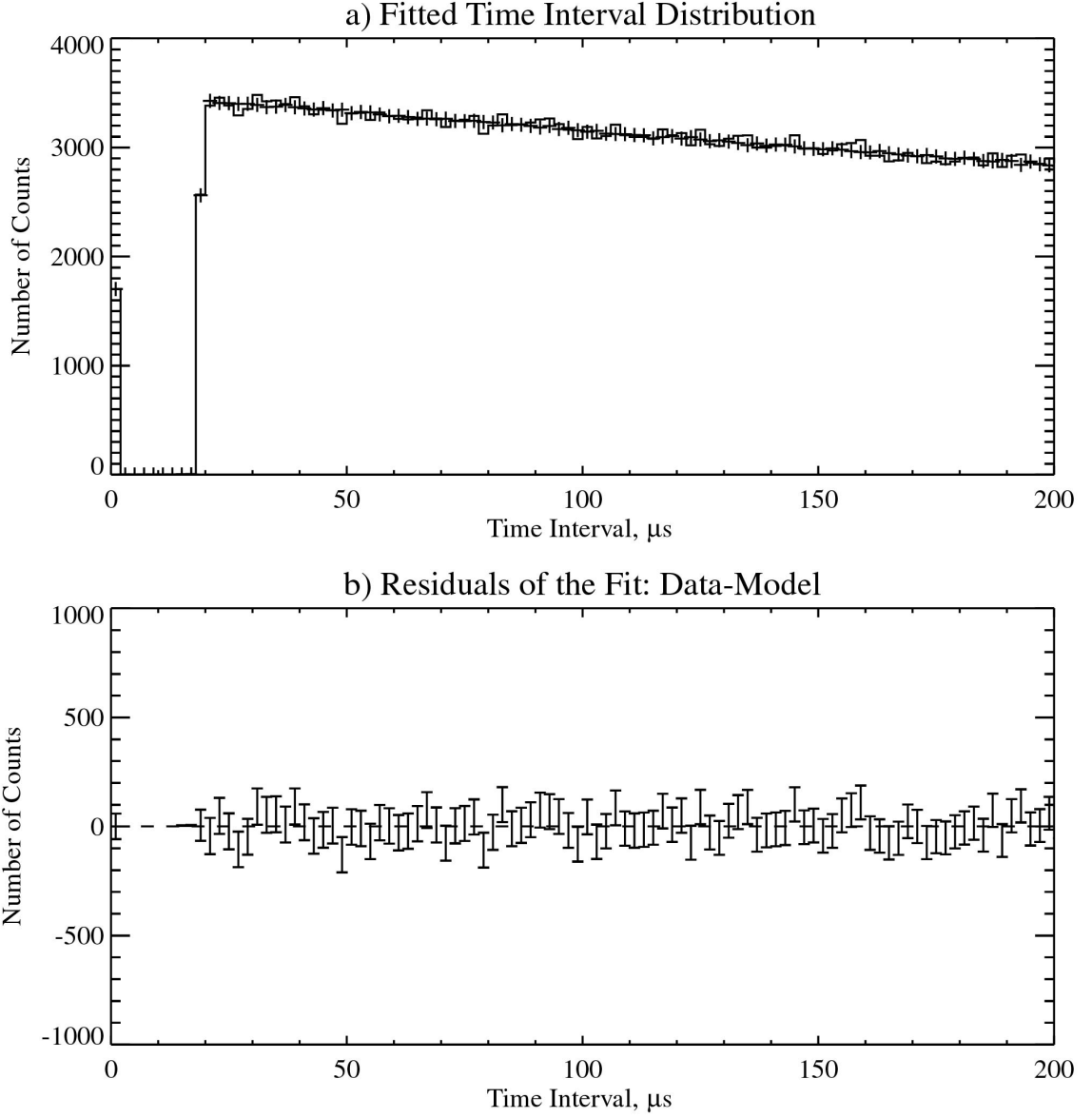


Figure 5.17 The deadtime model fit to the time interval distribution. a) Histogram of the time interval distribution of the detector 1, mode 4 data (2 million events). Crosses represent the model (50 million events). Deadtime:  $\tau=16.51 \mu\text{s}$ , bin size:  $t_b=2 \mu\text{s}$ ,  $r_o=1035 \text{ Hz}$ .  $\chi^2=0.979$  (dof=493).

The  $0^{th}$  bin contains same time events. b) Difference between the data and the model. Range up to  $200 \mu\text{s}$  is shown as the most interesting. There are no deviations of the model from the data beyond this range.

we know is that the first photon arrived either 16  $\mu$ s or 18  $\mu$ s earlier than the second one.

The deadtime value is determined as the value of the parameter that minimizes  $\chi^2$  when comparing the binned time interval distribution of the measured versus the simulated data of the same rate. The time interval distributions are compared for all time intervals below 1 ms.

Figure 5.16a shows the histogram of the time intervals for the calibration data at 4075 Hz observed rate. The counts in the 0<sup>th</sup> bin of the time interval distribution are due to the STE. The crosses correspond to the simulated data. Figure 5.16b shows the residuals of the fit.

The main discrepancy between the Monte Carlo and the data is observed in the 12-22  $\mu$ s time interval range. The Monte Carlo model does not allow any events with time interval less than 16  $\mu$ s due to the electronics non-extended deadtime. Furthermore, all events with time intervals less than 17  $\mu$ s are assigned the same times. Thus, the minimum time interval allowed by the model should be 18  $\mu$ s (after accounting for 2  $\mu$ s time resolution). In rare cases, the Monte Carlo model can allow for 16  $\mu$ s time intervals between events. This happens when three events arrive close together, and, as a result, the first is assigned the time of the second and the second is assigned the time of the third. In this scenario, the first two events can be separated by 16  $\mu$ s.

In the calibration data, we found a small fraction of the events with even smaller time intervals (between 12  $\mu$ s and 16  $\mu$ s). These intervals occur rarely (in less than 0.002% of the cases). Their origin is similar to the origin of the 16  $\mu$ s intervals discussed above; however, in the calibration data three events arrive even closer together. Another discrepancy between the model and the data is a lack of events in the data with time intervals in the 18-22  $\mu$ s range.

The difference between the data and the model for the smallest time intervals arises from

Detector ID	Observed Rate (Hz)	Event Mode Number	Deadtime ( $\mu\text{s}$ )	$\chi^2 / \text{dof}$	DOF
0	4075	3	16.368 $\pm$ 0.007	2.044	494
0	4030	3	16.38 $\pm$ 0.01	1.787	494
0	3836	3	16.377 $\pm$ 0.008	1.776	494
0	3182	3	16.41 $\pm$ 0.01	1.250	494
0	3009	4*	16.400 $\pm$ 0.009	1.181	494
1	3035	3	16.46 $\pm$ 0.01	1.373	494
1	2594	3	16.50 $\pm$ 0.01	1.355	494
1	2151	3	16.48 $\pm$ 0.01	1.112	494
1	1884	3	16.50 $\pm$ 0.02	1.091	494
1	1608	3	16.50 $\pm$ 0.01	1.084	494
1	1035	4	16.51 $\pm$ 0.02	0.979	493

Table 5.4 Summary of the results of the deadtime model fit to the data. The DIB resync time for the data set marked with \* is 63  $\mu\text{s}$ . For the rest of the data the DIB resync time is 40  $\mu\text{s}$ . Samples of 5 million data events (or as many as were available) and 50 million Monte Carlo events were used for each fit.

the simplified assumption of fixed non-extended deadtime. The actual detector electronics deadtime varies from 13.5  $\mu\text{s}$  to 17.5  $\mu\text{s}$  (and for very exotic event sequences can be as short as 12  $\mu\text{s}$  or as long as 20  $\mu\text{s}$ ), while the model assumes a fixed non-extended deadtime between 16  $\mu\text{s}$  and 17  $\mu\text{s}$  (the value of the model deadtime slightly depends on the counting rate). The lack of events in the data with time intervals in the 18-22  $\mu\text{s}$  range suggests that some of the events that arrive within short time intervals might be lost while being processed by the DIB (see discussion at the end of Section 5.1.2). If this is the case, than the actual deadtime of the whole system (electronics and DIB) is longer than that predicted by the model. Further analysis (see Section 5.4.6) points towards this possibility. Nevertheless, this model is a very good approximation for the real detector.

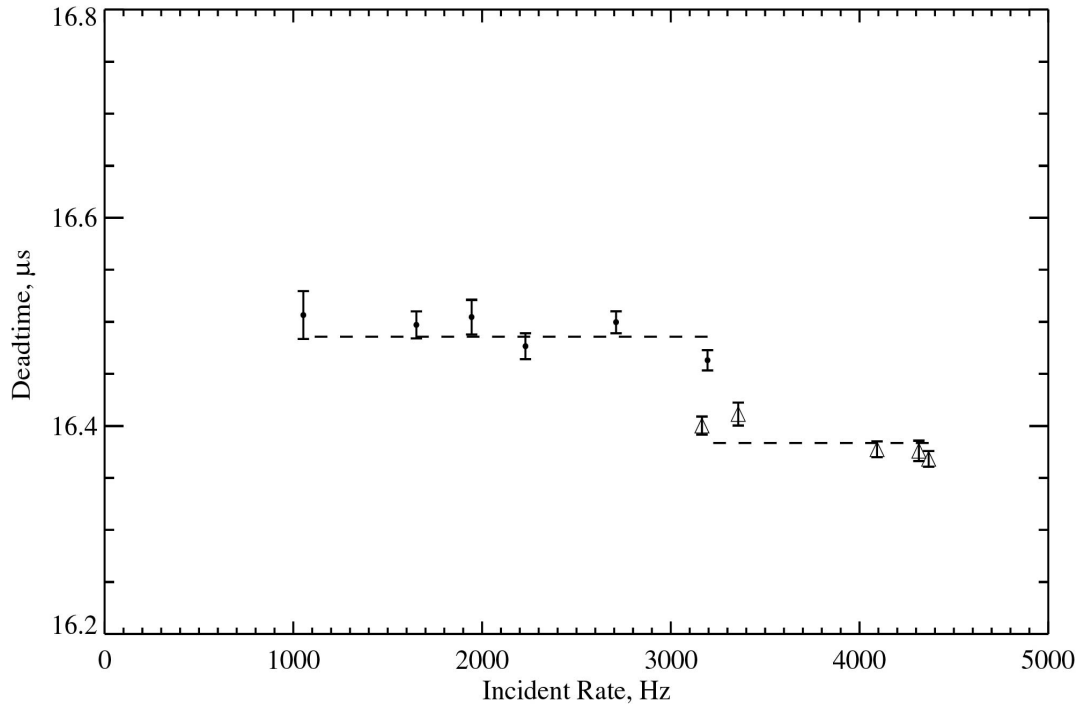


Figure 5.18 Deadtime as a function of the incident rate. Detector 0 and detector 1 are marked with triangles and dots, respectively. The dashed lines show the best constant fit.  $\chi^2=3.870$  for detector 0 (dof=4).  $\chi^2=2.104$  for detector 1 (dof=5).

For the lower counting rates ( $\lesssim 2000$  Hz), these discrepancies disappear. In general, higher order deadtime effects become significant only at high rates. As an example, Figure 5.17a shows the histogram of the time intervals for the calibration data at the lowest available observed rate (1035 Hz). Figure 5.17b shows the residuals of the fit.

The model was fitted to the data in mode 3 and, for the rates that were not available in mode 3, in mode 4. The results of the fit for various data rates are shown in Table 5.4.

Figure 5.18 shows the deadtime as a function of the incident rate. The incident rates are calculated from the observed rates using (4.3). We can see that the deadtime for detector 0 is generally smaller than for detector 1. The data points at the same ( $\sim 3000$  Hz) rate for



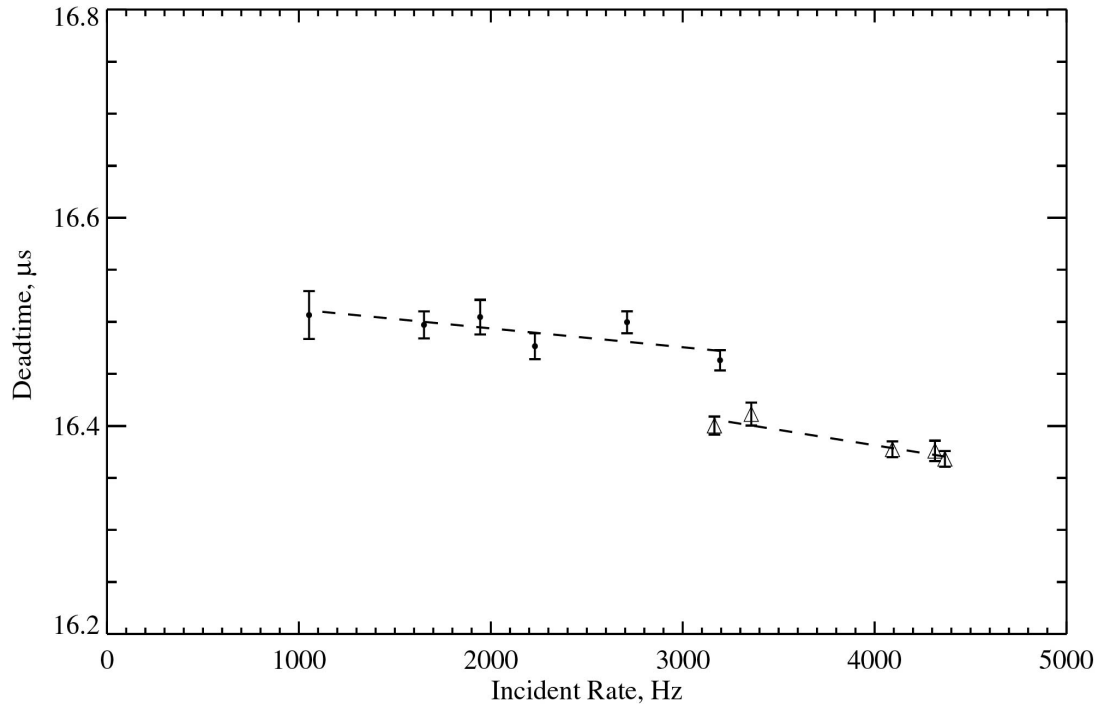


Figure 5.19 Deadtime as a function of the incident rate. Detector 0 and detector 1 are marked with triangles and dots, respectively. The dashed lines show the best linear fit.  $\chi^2=0.573$  for detector 0 (dof=3).  $\chi^2=1.388$  for detector 1 (dof=4).

the two detectors clearly show that the detectors' deadtimes are slightly different. This difference is most likely due to small differences in the electronic components of the two detectors. The constant least squares fit to the deadtime as a function of the rate gives  $\tau_0=16.383\pm0.004$   $\mu\text{s}$  deadtime for detector 0 and  $\tau_1=16.486\pm0.005$   $\mu\text{s}$  deadtime for detector 1 (where the errors are statistical errors from the fit).

It is difficult to determine, based on the available data, whether the deadtime is rate-dependent. The deviations of the deadtime from the constant value could be statistical, or the deadtime could be rate-dependent, or it could be slightly dependent on the position of the point X-ray source relative to the detectors (each rate corresponds to the different position). The linear least squares fit to the deadtime as a function of the rate yields better

Detector ID	a ( $\mu\text{s}/\text{Hz}$ )	b ( $\mu\text{s}$ )	$\chi^2 / \text{dof}$	DOF
0	$(-3.0 \pm 0.8) \times 10^{-5}$	$16.50 \pm 0.03$	0.573	3
1	$(-1.8 \pm 0.8) \times 10^{-5}$	$16.53 \pm 0.02$	1.388	4

Table 5.5 Results of the straight line fit to the deadtime as a function of rate:  $\tau = ar_{in} + b$

value of  $\chi^2$  than the constant fit (see Figure 5.19). Table 5.5 lists the results of the linear fit. This result suggests that the electronics deadtime depends linearly on the incident rate. Qualitatively, we expect that with increased rate the electronics deadtime becomes smaller due to a more frequent one-shot stretching time shortening. However, it is difficult to generalize this dependency for the entire range of rates. Measurements with an on-orbit calibration source at various rates will show how the electronics deadtime depends on the rate.

For our model we make the approximation that the deadtime does not depend on the rate. The difference between a power spectrum generated by a model with constant deadtime and a model with linear deadtime dependence is on the order of magnitude smaller as compared to the difference between a power spectrum generated by the model and the power spectrum of the calibration data.

In order to use the model, described above, for the power spectrum noise correction, we need to compare the power spectrum of the data with the power spectrum generated by our model. This comparison is done in Section 5.4.6.

### 5.4.2 Poisson Noise Power Spectrum Framework

As discussed in Section 4.2.3, the power spectrum of the noise in the detector,  $P_j^{noise}$ , depends on the type and value of the deadtime,  $\tau$ , the counting rate,  $r_o$ , and the size of time series bin,  $t_b$ . The PSD of the Poisson noise with any type of deadtime, can be represented as [106]

$$P_j^{noise} = \sum_{k=1}^N P_k \cos\left(\frac{2\pi j(k-1)}{N}\right) = P_1 + P_2 \cos \frac{2\pi j}{N} + P_3 \cos \frac{4\pi j}{N} + \dots, \quad (5.1)$$

where  $N$  is the total number of bins in the PSD and  $j$  is the frequency bin number. The values of the coefficients  $P_k$  depend on the type and value of  $\tau$ , on  $r_o$  and  $t_b$ . In the case when  $t_b \geq \tau$ , only a few terms are required in equation (5.1). For extended deadtime, only the first two coefficients have nonzero value. For non-extended deadtime, all the coefficients  $P_k$  are nonzero, but they rapidly approach zero as  $k$  increases. When  $t_b < \tau$ , many terms may be required to accurately describe the noise spectrum.

In our calibration data analysis we frequently use equation (5.1) to characterize the power spectrum.

### 5.4.3 Power Spectra of the Calibration Data

The noise power spectrum of the instrument can be described by the analytical function (5.1). This description is a convenient and accurate way to characterize a power spectrum of the noise. This description can also be used to compare the power spectrum of the calibration data with the power spectrum of the data simulated according to the model of Section 5.4.1.

To characterize the calibration data power spectrum, we calculated the PSD for various values of  $t_b$  (see Table 5.3), since the shape of the power spectrum depends on this parameter. The choice of  $t_b$  values is dictated by the choice of the corresponding Nyquist frequencies. We anticipate the Nyquist frequency values, shown in Table 5.3, to be commonly used for USA studies of Fourier power at high frequencies. For the details of how the PSD calculations for the calibration data were performed, see Section 5.2.3. Mode 3 data was used to calculate the power spectrum and mode 4 data for the rates that were not available in mode 3.

The noise power spectrum when the bin size is greater than or equal to the deadtime can be described with good accuracy by (5.1) with only two non-zero coefficients (see Section 5.4.2)

$$P_j^{noise} = P_1 + P_2 \cos \frac{2\pi j}{N}, \quad (5.2)$$

where the values of  $P_1$  and  $P_2$  depend on the bin size, the counting rate, and the type of the deadtime. We performed the least squares fit to the power spectrum of the data using function (5.2). In general, for on-orbit data analysis, the commonly used bin size is greater than the deadtime. (Note that, for example, the bin size  $t_b=2 \mu\text{s}$  corresponds to 250000 Hz Nyquist frequency. The detection of a power at such high frequencies is unlikely). Thus, only the results for the cases when the bin size is greater than the deadtime are of practical importance.

Figure 5.20 shows the fitted power spectrum and the residuals of the fit for the highest observed rate of 4075 Hz in the case when  $t_b=96 \mu\text{s}$  (corresponding Nyquist frequency is 5208 Hz). This range of frequencies (up to several kHz) is the most interesting for the searches of a high-frequency phenomena, such as QPOs and asynchronous high-frequency power.

Table A.2 in the Appendix lists the results of the fit to the power spectrum of the data for various rates and binning.

The residuals of the fits for the various values of  $t_b$  show systematic structure at frequencies between 0 Hz and  $\sim 1000$  Hz (see Figure 5.20b). This occurs only in the data sets with the highest rate and highest statistics available. Note that a similar fit (discussed in detail in Section 5.5. The shape of the structure is similar to the energy-dependent structure (Figure 5.35). To our understanding, the effect arises when the photon energy spectrum has an asymmetrical shape. The effect is small when all the energy channels are

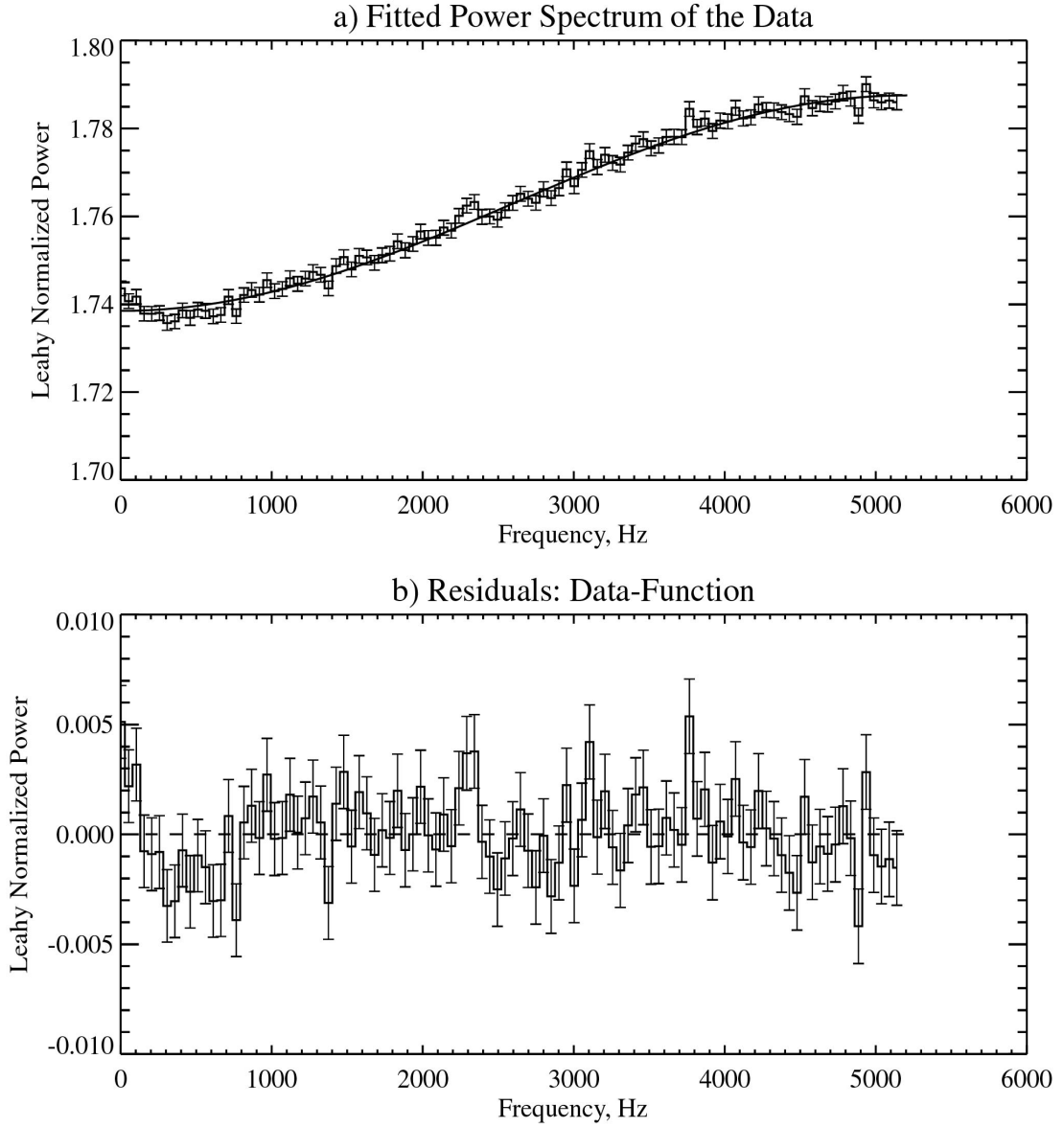


Figure 5.20 a) Power spectrum of the mode 3, detector 0 data fitted with (5.2).  $r_o=4075$  Hz,  $t_b=96$   $\mu$ s. Total exposure time: 21.8 ks. Fitting range: 0-5000 Hz. Solid line: fit. b) Difference between the power spectrum of the data and the fit function.

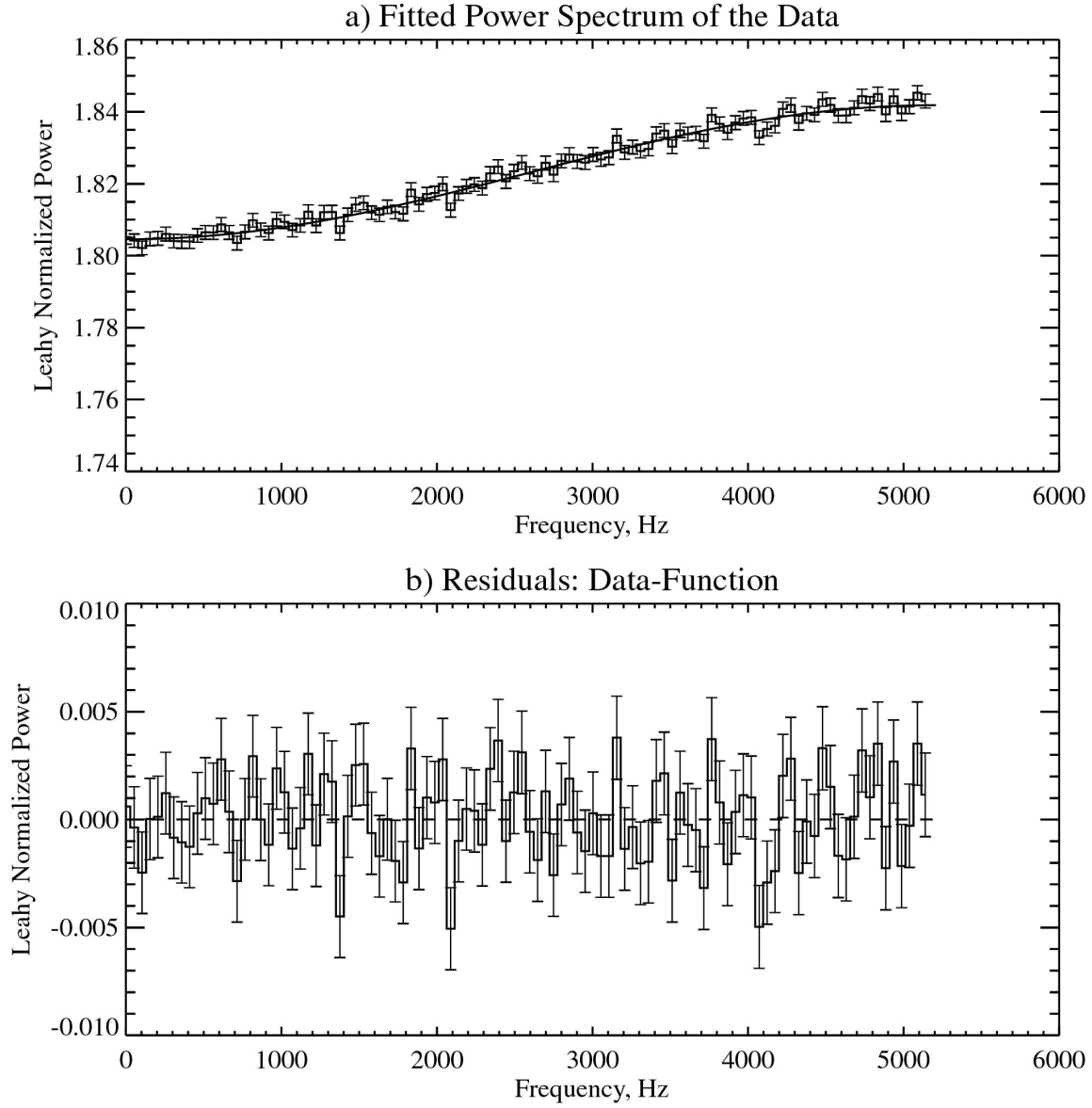


Figure 5.21 a) Power spectrum of the mode 3, detector 1 data fitted with (5.2).  $r_o=3035$  Hz,  $t_b=96$   $\mu$ s. Total exposure time: 17.9 ks. Fitting range: 0-5000 Hz. Solid line: fit. b) Difference between the power spectrum of the data and the fit function.

combined as in Figure 5.20 (the energy spectrum of the  $^{55}\text{Fe}$  calibration source is almost symmetrical in this case). When the selection on energy is made, the energy-dependent instrumental effect becomes more pronounced as in Figure 5.35. Here and in all of the discussions of Section 5.4 we effectively ignore this effect. The final correction method (Section 5.5) takes this effect into account, and uses the results developed in Section 5.4 as a basis. The structure disappears for lower rates (see Figure 5.21).

If one needs to achieve better accuracy in phenomenological description of the calibration data power spectra, more than two coefficients in equation (5.1) should be used.

#### **5.4.4 Comparison of the Power Spectra of the Data in Different Data Modes**

We calculated the power spectrum for various values of  $t_b$  from Table 5.3 for all the data listed in Table A.1. We compared the power spectrum of the data in all four data modes both by looking into the differences between the power spectra and by looking at the results of the fits with function (5.2). We made a comparison between data samples in different modes with the same value of  $t_b$  and similar counting rates. Within statistics of the samples of the data that we had, we did not find any systematic differences between the power spectra of the data in various data modes.

#### **5.4.5 Power Spectra of the Simulated Data**

In this section, we describe the power spectra of the data, simulated based on the Monte Carlo model of Section 5.4.1.

To make the comparison between the data and the model, we simulated time series for various rates by following our model. We used deadtime values of  $\tau_0$  and  $\tau_1$  for detector 0 and detector 1, respectively. We assumed that the non-extended deadtime does not depend on the rate for each detector.

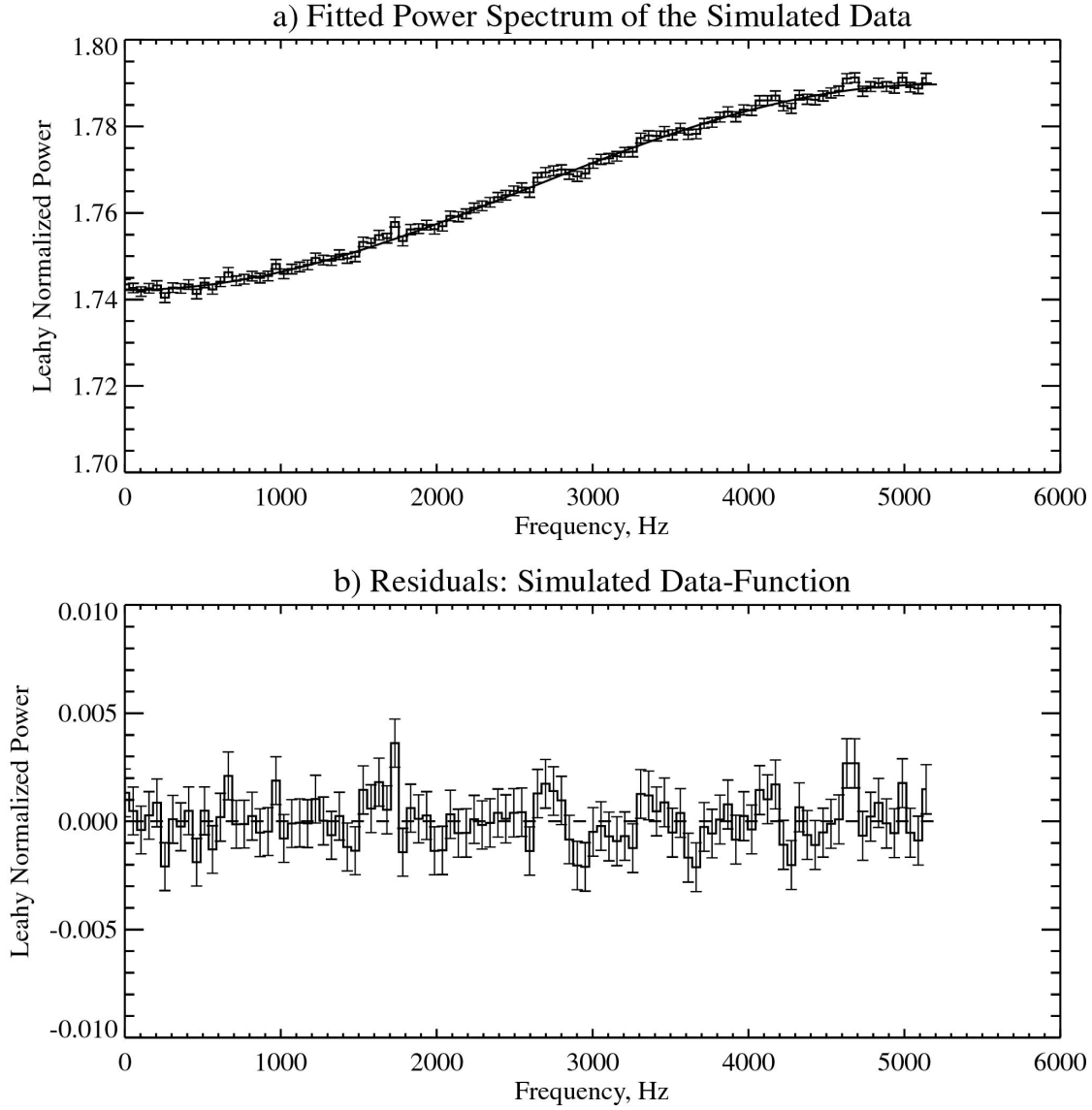


Figure 5.22 a) Power spectrum of the simulated data fitted with (5.2). Parameters of the model:  $r_o=4075$  Hz,  $\tau_0=16.383$   $\mu$ s.  $t_b=96$   $\mu$ s. Total exposure time: 49.0 ks. Fitting range: 0-5000 Hz. Solid line: fit. b) Difference between the power spectrum of the simulated data and the fit function.



We calculated the PSD of the simulated data for various values of  $t_b$  (see Table 5.3). The PSD for the simulated data was calculated in the same way as for the high-bit rate mode calibration data (see Section 5.2.3).

To describe the power spectra of the simulated data, we fitted it with equation (5.2) using the least squares fit method. Figure 5.22 shows the fitted power spectrum of the simulated data and the residuals of the fit for the highest observed rate of 4075 Hz. Table A.3 lists the results of the fits to the power spectrum of the simulated data for various rates and binning.

There are no significant systematic residuals between the power spectrum of the simulated data and the fit function that we could detect with statistics available for any values of  $t_b$  and for any rate.

Next section discusses in detail the accuracy of the model with regard to the on-ground calibration data.

#### **5.4.6 Comparison of the Power Spectra of the Simulated Data With the Power Spectra of the Calibration Data**

In this section, we compare the power spectra of the calibration data (discussed in Sections 5.4.3) and the power spectra of the simulated data (discussed in Section 5.4.5).

The difference between the power spectra of the simulated and the calibration data in the case when the bin size is greater than or equal to the deadtime can be described by (see Section 5.4.2)

$$P_j^{diff} = \Delta P_1 + \Delta P_2 \cos \frac{2\pi j}{N}, \quad (5.3)$$

where  $\Delta P_1 = P_1^{sd} - P_1^d$  is the difference in  $P_1$  coefficients, obtained by fitting power

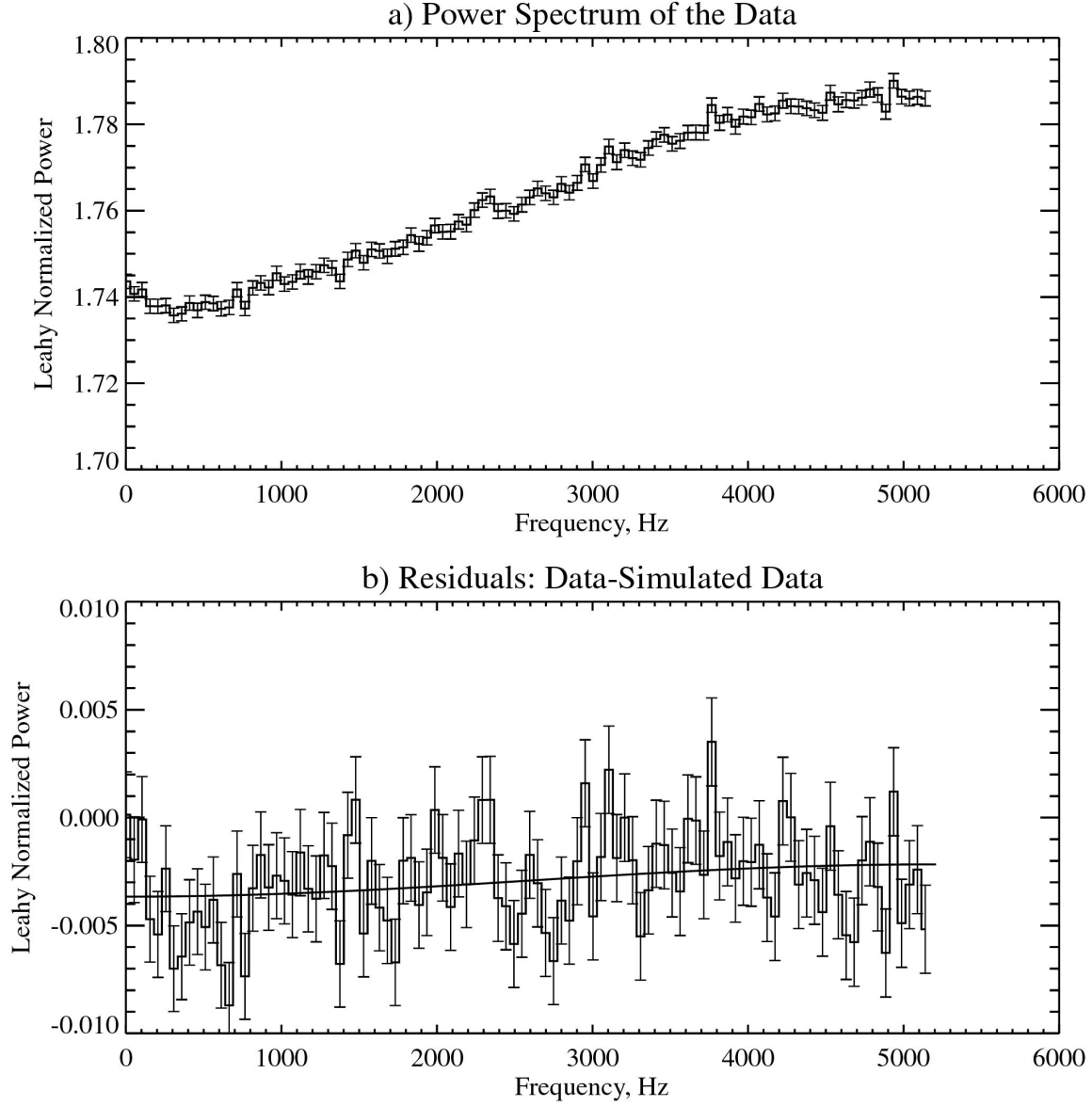


Figure 5.23 a) Power spectrum of the mode 3, detector 0 data.  $r_o=4075$  Hz,  $t_b=96$   $\mu$ s. Total exposure time: 21.8 ks. b) Difference between the power spectra of the calibration data and the simulated data. Parameters of the model:  $r_o=4075$  Hz,  $\tau_0=16.383$   $\mu$ s.  $t_b=96$   $\mu$ s. Total exposure time: 49.0 ks. Solid line: function (5.3).

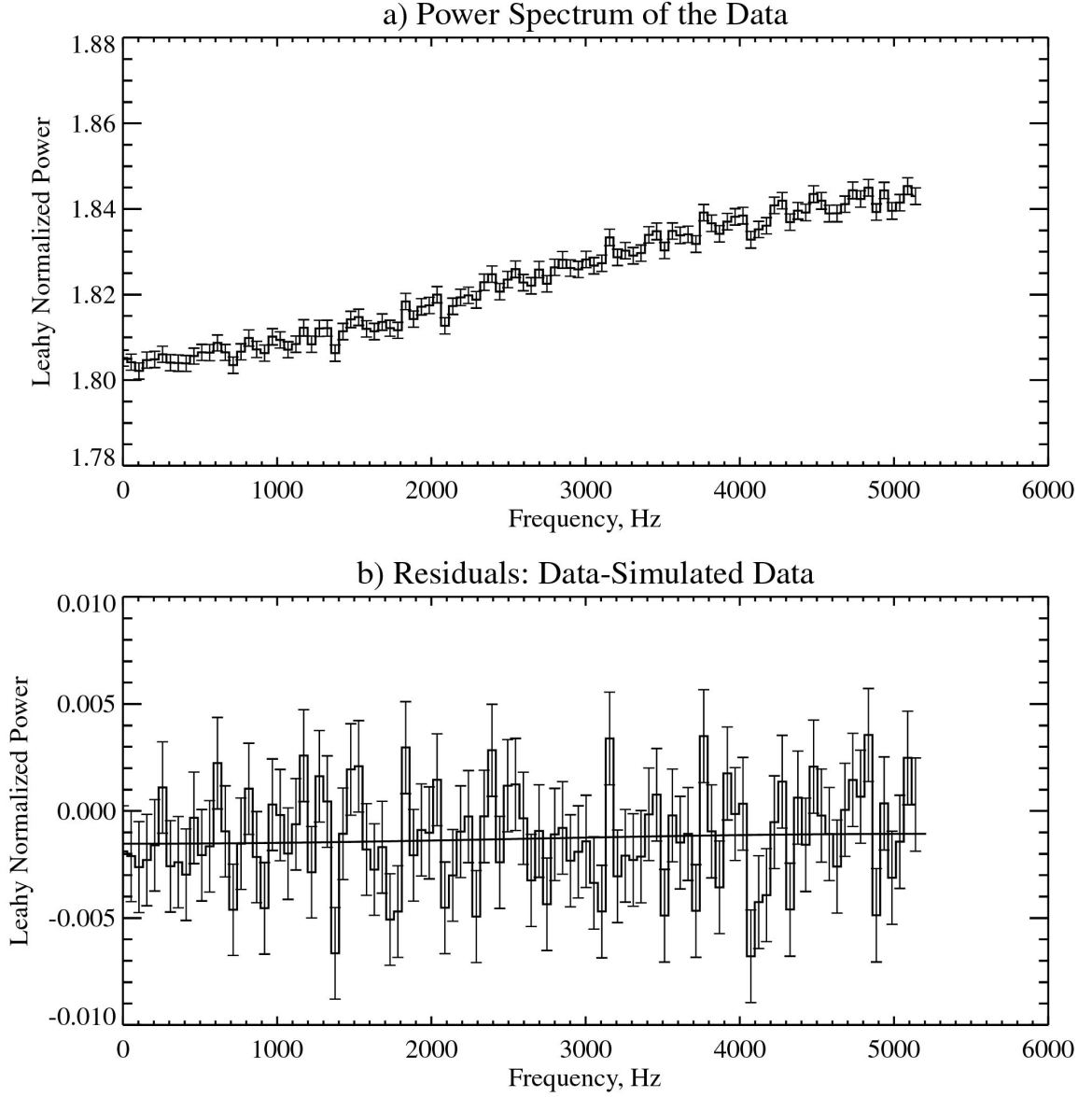


Figure 5.24 a) Power spectrum of the mode 3, detector 1 data.  $r_o=3035$  Hz,  $t_b=96$   $\mu$ s. Total exposure time: 17.9 ks. b) Difference between the power spectra of the calibration data and the simulated data. Parameters of the model:  $r_o=3035$  Hz,  $\tau_0=16.383$   $\mu$ s.  $t_b=96$   $\mu$ s. Total exposure time: 65.9 ks. Solid line: function (5.3).

spectrum of the simulated data and the calibration data, respectively, and  $\Delta P_2 = P_2^{sd} - P_2^d$  is the difference in  $P_2$  coefficients.

The following figures illustrate the difference between the power spectrum of the model and the power spectrum of the data in the case when  $t_b=96 \mu\text{s}$ . Figure 5.23a shows the power spectrum of the calibration data at an observed rate of 4075 Hz. Figure 5.23b shows the difference between the power spectrum of the data and the power spectrum of the simulated data. Function (5.3) is shown in solid line in Figure 5.23b. As seen from the figure, function (5.3) describes the residuals between the power spectrum of the data and the power spectrum of the simulated data well. The residuals deviate slightly from function (5.3) since the calibration data is not adequately described by only two coefficients  $P_k$ , as discussed in Section 5.4.3.

Figure 5.24 shows the power spectrum and the difference between the power spectrum of the data and the power spectrum of the simulated data for the lower 3035 Hz rate.

The parameters  $\Delta P_k$  describe the systematic deviation of the simulated data from the calibration data (values of the  $P_k$  coefficients for the calibration data and the simulated data are listed in Table A.2 and Table A.3, respectively).

The systematic deviations of the model from the data become smaller as the counting rate decreases. In the case of  $t_b=96 \mu\text{s}$ , the agreement between the model and the data is very good for the rates below  $\sim 3000$  Hz.

Figure 5.25-Figure 5.28 help us to characterize these deviations, as well as the noise power spectrum behavior, for various values of  $t_b$  and the rate. Figure 5.25 shows the values of the coefficients  $P_1$  and  $P_2$  obtained by fitting the power spectrum of the calibration data with (5.2) ( $t_b=32 \mu\text{s}$ ). In theory,  $\lim_{r_0 \rightarrow 0} P_1 = 2$  and  $\lim_{r_0 \rightarrow 0} P_2 = 0$  for the power spectrum of the Poisson process with any deadtime. It means that for the low rates,

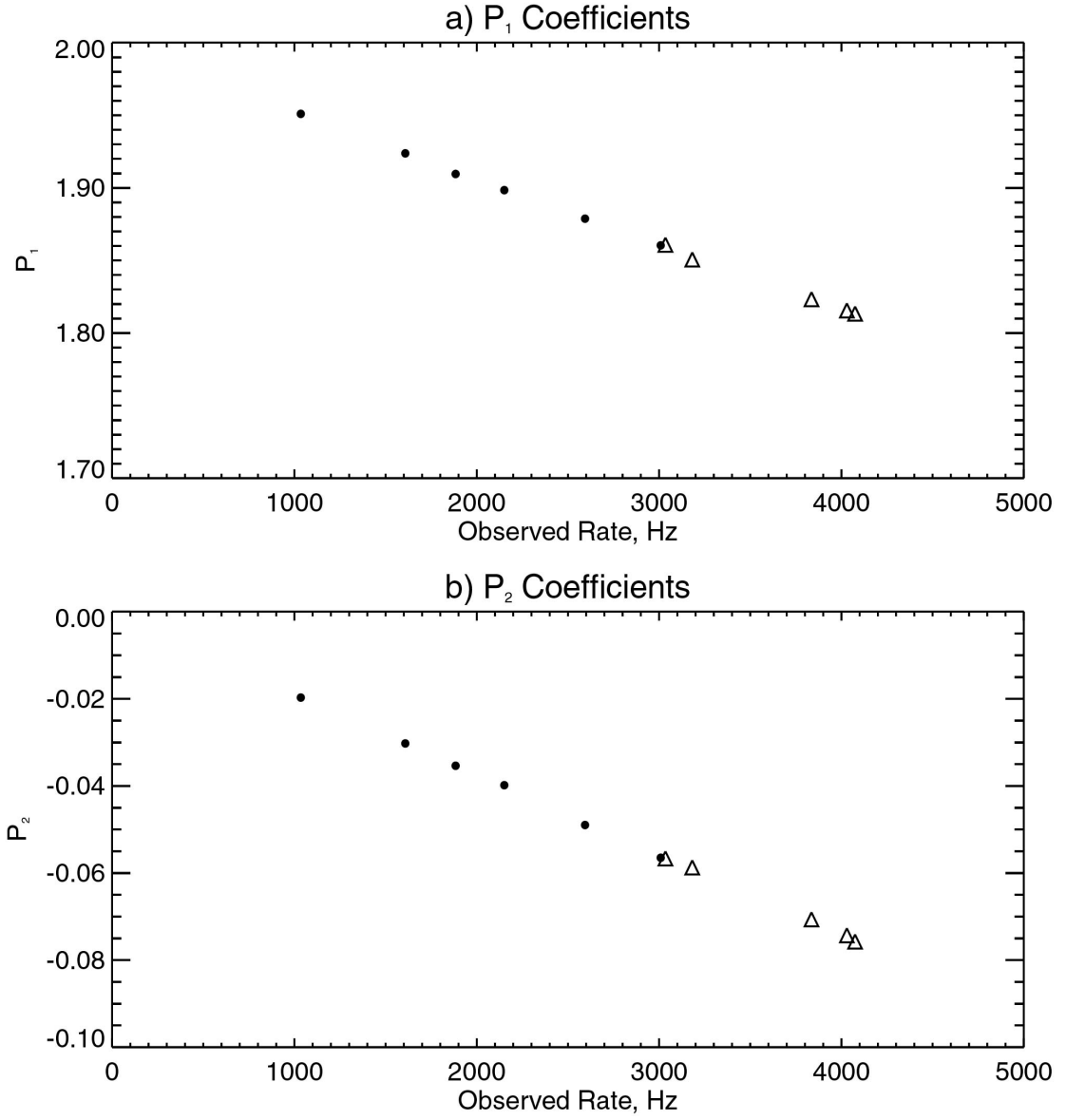


Figure 5.25  $P_1$  and  $P_2$  coefficients describing fit to the calibration data.  $t_b = 32 \mu\text{s}$ . Points marked with triangles correspond to detector 0 and with dots to detector 1. The error bars are omitted, since they are smaller than the size of the data points.

the power spectrum becomes flatter ( $P_2$  is the amplitude of oscillation in the power spectrum) and close to 2.

Figure 5.26 shows the values of the coefficients  $P_1$  and  $P_2$  for the calibration data, for the data simulated using the deadtime model, and for the theoretical values of  $P_1$  and  $P_2$  in the case of a Poisson process with pure non-extended and extended deadtimes ( $t_b=32 \mu s$ ). We chose this binning to better illustrate the trends in the  $P_k$  values. Coefficients  $P_k$  for non-extended and extended deadtimes are calculated analytically using formulas from [106]. To better illustrate the relative differences in the values of coefficients in the various cases, we subtract the values of the coefficients corresponding to the extended deadtime case ( $P_k^{extended}$ ). When calculating  $P_k$  for the non-extended and extended deadtime, we used  $\tau_0$  and  $\tau_1$  as the deadtimes for detector 0 and detector 1, respectively.

Figure 5.26 shows that the data simulated using the deadtime model approximates best the calibration data. The differences in  $P_1$  and  $P_2$  coefficients between the various types of deadtimes ( $\delta P_1$  and  $\delta P_2$ ) decrease as the rate decreases. In theory,  $\lim_{r_o \rightarrow 0} \delta P_1 = 0$  and

$$\lim_{r_o \rightarrow 0} \delta P_2 = 0.$$

Figure 5.27 and Figure 5.28 show  $\Delta P_1 = P_1^{sd} - P_1^d$  and  $\Delta P_2 = P_2^{sd} - P_2^d$  as a function of bin size,  $t_b$ , for the 4075 Hz and 3035 Hz observed rates, respectively. We can see that  $\Delta P_1$  increases and  $\Delta P_2$  decreases with the increase in  $t_b$ :  $\lim_{t_b \rightarrow 0} \Delta P_1 = const$  and

$$\lim_{t_b \rightarrow 0} \Delta P_2 = 0.$$

It means that the difference between the power spectrum of the simulated

data and the calibration data flattens out for large values of  $t_b$ , and the two power spectra remain offset by a constant. We can also see from Figure 5.27 and Figure 5.28 that both  $\Delta P_1$  and  $\Delta P_2$  decrease with decreasing rate for the same value of  $t_b$ , as mentioned above.

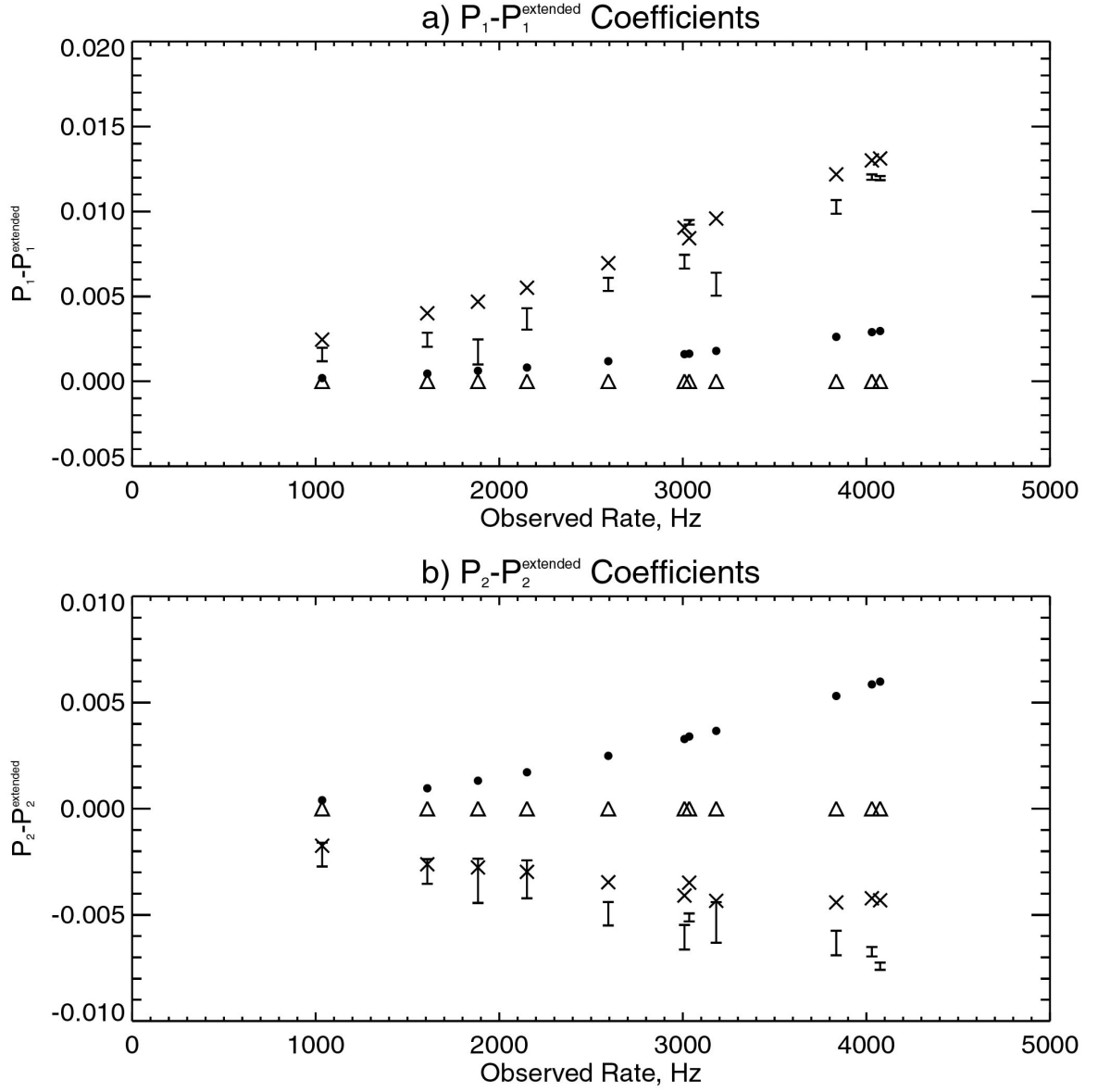


Figure 5.26 a)  $P_1 - P_1^{\text{extended}}$  coefficients. b)  $P_2 - P_2^{\text{extended}}$  coefficients.  $t_b = 32 \mu\text{s}$ . Points with error bars correspond to the calibration data, crosses to the model, dots to the non-extended deadtime, and triangles to the extended deadtime (obviously, triangles form zero baseline). Data at low rates was collected from detector 1 and at high rates from detector 0 (see Table A.1). For all the points, except the ones corresponding to calibration data, the error bars are omitted, since they are smaller than the size of the data points.

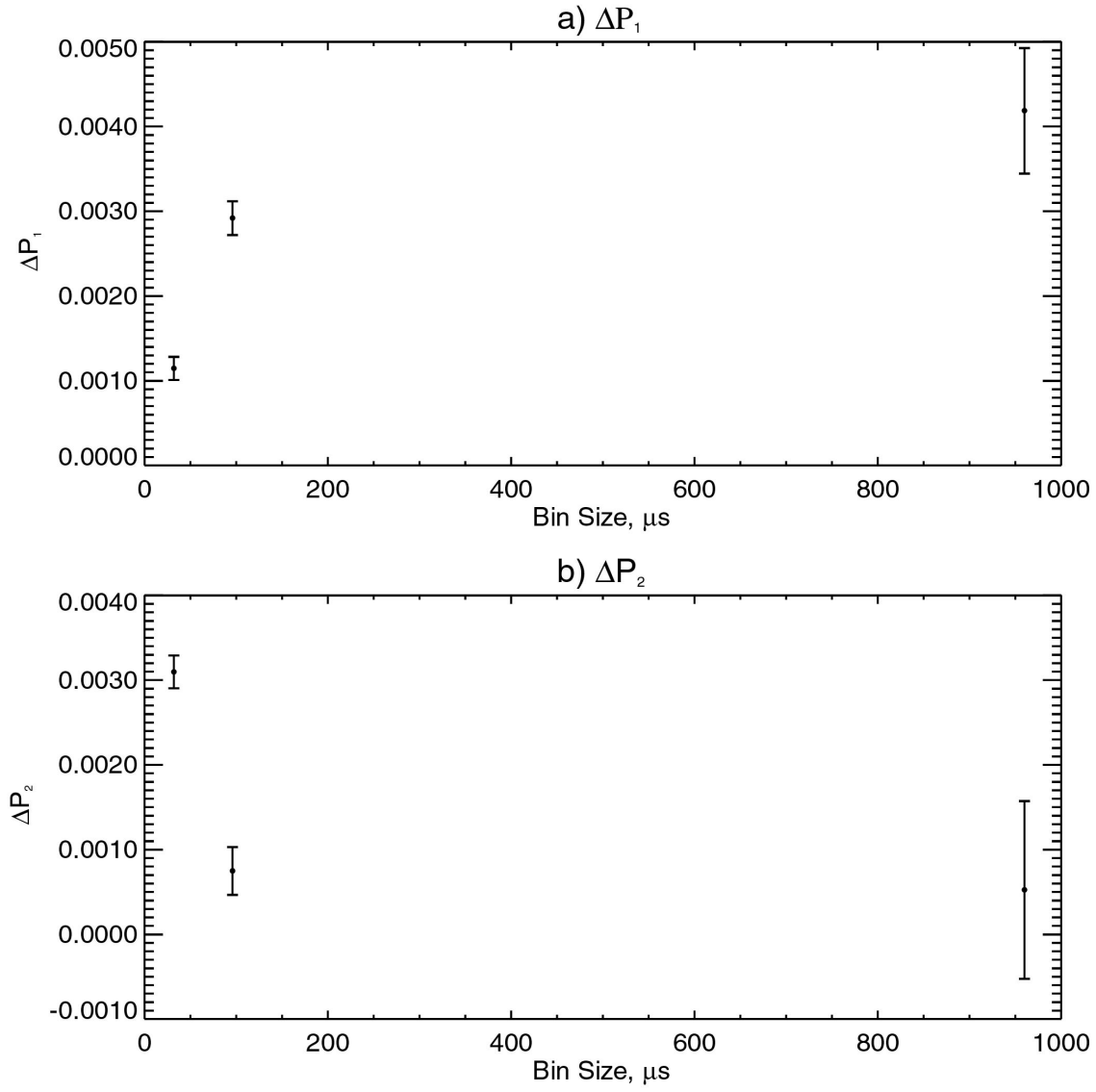


Figure 5.27 a)  $\Delta P_1 = P_1^{sd} - P_1^d$ . b)  $\Delta P_2 = P_2^{sd} - P_2^d$ .  $r_o = 4075$  Hz. Detector 0 data.



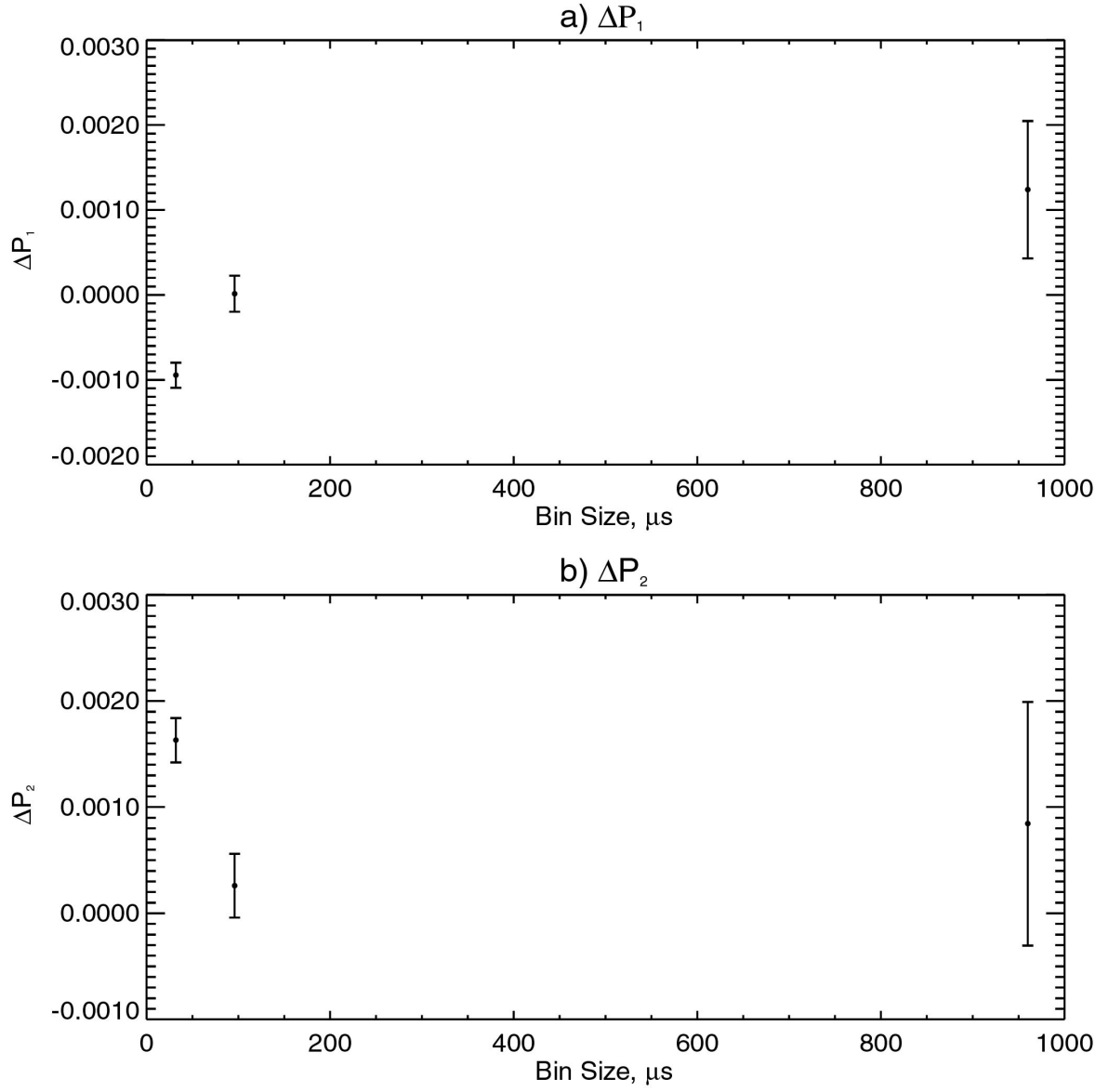


Figure 5.28 a)  $\Delta P_1 = P_1^{sd} - P_1^d$ . b)  $\Delta P_2 = P_2^{sd} - P_2^d$ .  $r_o = 3035$  Hz. Detector 1 data.

Note that we have large statistics on calibration data only for three observed rates: 4075 Hz, 4030 Hz and 3035 Hz (see Table A.1). In discussing the accuracy of the Monte Carlo model, we will focus on the results for the data sets that have observed rates of 4075 Hz and 3035 Hz.

For  $t_b=96 \mu\text{s}$  and the rates between  $\sim 3000$  Hz and  $\sim 4000$  Hz,  $|\Delta P_1| < \sim 0.003$  and  $|\Delta P_2| < \sim 0.001$ . For  $t_b=96 \mu\text{s}$  and the rates below  $\sim 3000$  Hz,  $|\Delta P_1| \approx 0$  and  $|\Delta P_2| < \sim 0.0003$ . The deviations for other values of  $t_b$  can be estimated in the same way. In the USA workhorse regime (rates below 3000 Hz,  $t_b=96 \mu\text{s}$ ), the agreement between the data and the model is very good (less than 0.1%). (Only few known sources, like Crab and Sco X-1, have USA rates higher than 3000 Hz).

Figure 5.26 illustrates the differences between the simulated data, the calibration data and the systems with extended and non-extended deadtimes. The model assumes fixed non-extended deadline,  $\tau_0$ , introduced into the timing stream by the detector electronics, and STE introduced by the DIB. Both the simulated data and the calibration data differ from the case of pure non-extended deadline largely due to effects of the DIB, namely same time events, which are present in the data and in the model. The difference between the model and the data (see Figure 5.23b) is most likely due to several factors. One is the fact that the electronics deadline is not perfectly non-extended, as assumed by the model. Another possible reason for the difference is that there might be an additional event loss in the DIB at high rates (see discussion at the end of Section 5.1.2). If this were the case, it would mean that overall deadline is longer than the one assumed in the model. If the deadline were longer, the  $P_1$  and  $P_2$  coefficients for the model would shift down in Figure 5.26, and the agreement between the model and the data would be better. This suggests that some loss of the events in the DIB might be happening. Those factors, most likely, are responsible for the residuals in Figure 5.23b that are well described by function (5.3). The large-scale variation in the residuals around the function (5.3) in the 0 to  $\sim 1000$  Hz region is probably due to the energy-dependent instrumental effect (discussed

in detail in Section 5.5), which is not accounted for in the Monte Carlo model. The shape of the structure is similar to the energy-dependent structure (Figure 5.35). To our understanding, the effect arises when the photon energy spectrum has asymmetrical shape. The effect is small when all the energy channels are combined as in Figure 5.20 (the energy spectrum of the  $^{55}\text{Fe}$  calibration source is almost symmetrical in this case). When the selection on energy is made, the energy-dependent instrumental effect becomes more pronounced as in Figure 5.35.

The results of this section were derived for the observed counting rates in the 1000-4100 Hz frequency range. We assumed that the deadtime does not depend on the rate (see Figure 5.18). This assumption might not hold for the rates higher than 4100 Hz, since at high rates the deviation of the real detector's deadtime behavior from the one assumed by the model is greater. The results for the observed counting rates in 1000-3000 Hz frequency range were obtained for detector 1, and in 3000-4100 Hz range for detector 0. Since only detector 0 is operating in orbit, the deadtime,  $\tau_0$ , should be used for all rates below 4100 Hz. From the behavior of detector 1 at low rates, we can speculate on the values of the PSD deviations of the model from the data, described by  $\Delta P_k$ , in detector 0.

## 5.4.7 Recipe for the Deadtime Correction

### Incident Rate Correction

In the absence of the background, for the on-ground calibration data, the incident rate can be calculated from the observed rate using

$$r_{in} = \frac{r_o}{1 - r_o \tau_0} , \quad (5.4)$$

where  $\tau_0 = 16.383 \pm 0.004 \mu\text{s}$  is detector 0 deadtime. This is a formula for non-extended deadtime, and it is applicable since the deadtime Monte Carlo model assumes

non-extended deadtime with the same time events that do not change the counting rate. For the purpose of the rate correction, the accuracy of the model is sufficient.

In the case of USA operation in orbit, when background rates become significant, the formula for the rate correction should take into account those rates. In this case, the incident rate can be estimated as

$$r_{in} = \frac{r_o}{1 - DTF}, \quad (5.5)$$

where  $DTF$  is a dead time fraction

$$DTF = r_o\tau_0 + r_p\tau_{logic} + r_c\tau_{one-shot} + r_{LE}\tau_{LE}, \quad (5.6)$$

where  $r_p$  is perimeter veto rate,  $\tau_{logic} = 7.5 \pm 1 \mu s$  is perimeter veto deadtime,  $r_c$  is total coincidence veto rate,  $\tau_{one-shot}$  is a deadtime caused by coincidence events ( $\tau_{one-shot}$  is on average  $15.6 \mu s$ , see Section 5.1.1),  $r_{LE}$  is large energy events rate, and  $\tau_{LE}$  is a deadtime caused by these events ( $\tau_{LE}$  varies with the energy of the event, see Section 5.1.1). This formula is true if all the incident events are independent and can be applied only to the sources with less than 10% deadtime [108]. This formula should be verified by the analysis of the on-orbit calibration data. Note that the value of  $r_{LE}$  is not available and has to be estimated.

### Power Spectrum Correction

In this section we discuss how the power spectrum of a source can be corrected for the noise, based on the findings of the previous sections. The relevant theory is discussed in Section 4.2.3.

It is likely that the power spectrum of the on-orbit calibration data will be different from the power spectrum of the on-ground calibration data. The methods described in this section are useful for the comparison of the on-ground calibration data to the on-orbit

calibration data. Section 5.6 describes what calibration needs to be done on-orbit. Similar correction methods need to be developed based on the on-orbit calibration data analysis. The corrections discussed in this section ignore the energy-dependent instrumental effect, and should be applied when the effect is insignificant. The correction methods of this section lay out the basis for the final correction method that considers the energy-dependent effect (Section 5.5).

The most accurate method one can use to correct the source power spectrum for noise is to subtract the same average rate calibration data power spectrum, which is defined by coefficients  $P_k$ . Section 5.4.3 discusses how the power spectrum of the calibration data is described by the set of coefficients  $P_k$ . Despite the accuracy, this method has a very limited application. Since the power spectrum depends on the bin size, the method is not convenient to use for a different binning than the one used in the Table 5.3. (Although raw calibration data is available and can be binned as desired). The power spectrum is also rate-dependent. We only have on-ground calibration data for five different rates for detector 0, and for only two of these is the amount of data large (4075 Hz and 4030 Hz). It is unclear how to interpolate these results for other rates without losing accuracy. Thus, this method can only be used for rates close to the rates of the calibration data. This method is very useful for the comparison of the on-ground calibration data to the on-orbit calibration data with the same rates. Two coefficients are sufficient when the bin size is greater than or equal to the deadtime. Table A.1 provides the values of  $P_1$  and  $P_2$  for several values of  $t_b$  and available values of  $r_o$ .

The most general way to correct the power spectrum is to use the Monte Carlo model of Section 5.4.1. The model can be used for the Monte Carlo simulation of the Poisson noise power spectrum and subsequent subtraction from the power spectrum of the data (the simulation and the data should have the same average rate). It can also be used for the simulation of the celestial X-ray source timing behavior and comparison with the observed power spectrum of the source. The advantage of the model is that it can be used

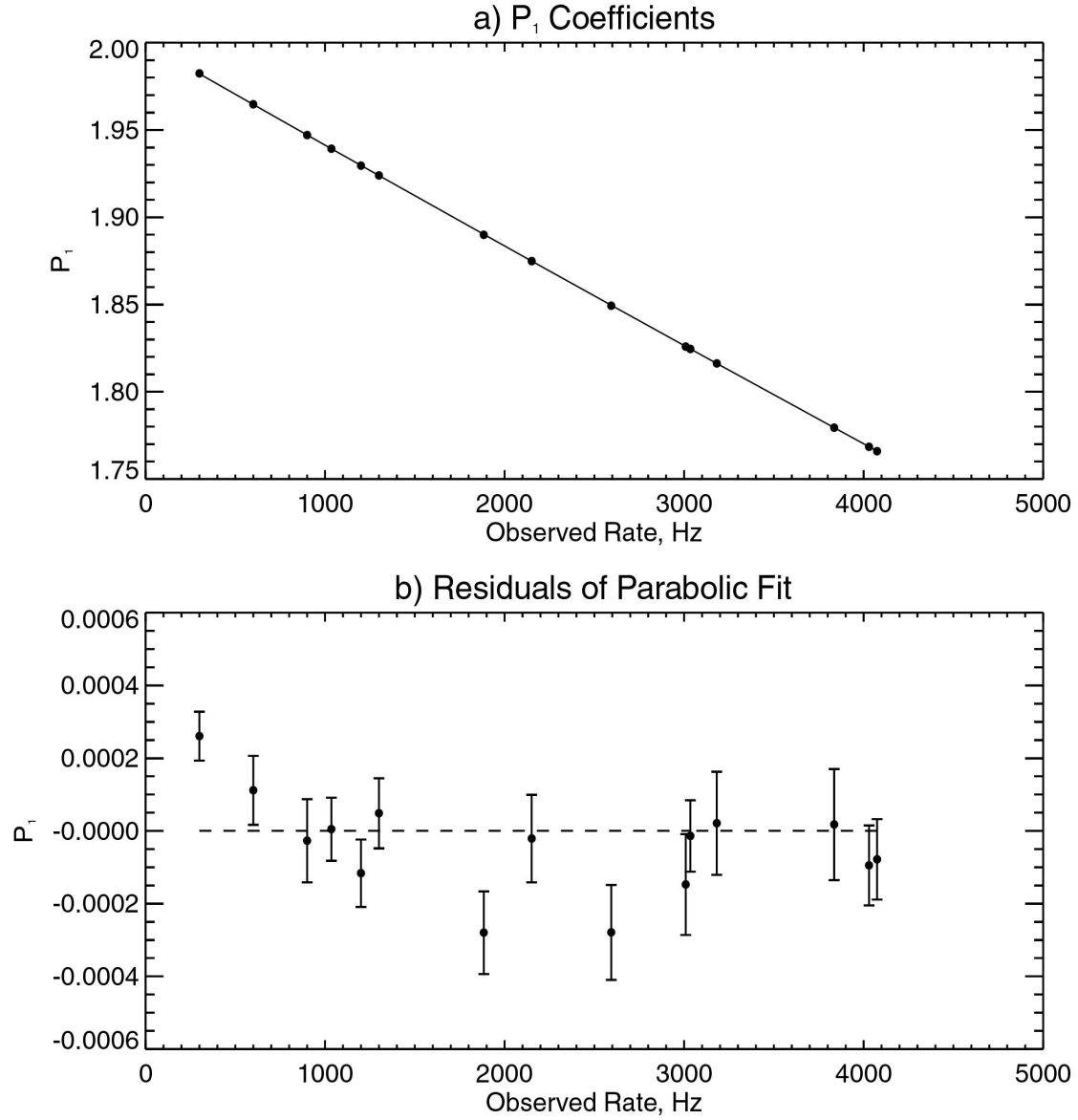


Figure 5.29 a) Parabolic fit to the coefficients  $P_1$  for the simulated data. The error bars are omitted, since they are smaller than the size of the data points. b) Residuals of the fit.  $t_b = 96 \mu\text{s}$ . The deadtime used in the simulation at all rates is the detector 0 deadtime.

for any rate less than 4100 Hz and for any binning. (At rates higher than 4100 Hz it is unclear by how much the model deviates from the data). The deviations of the deadtime model from the data can be estimated for various rates and values of  $t_b$  (see Section 5.4.6). For some specific parameters, these deviations are known exactly. Table A.3 lists the values of  $P_1$  and  $P_2$  for the simulated data power spectrum for some specific parameters. Combining information from Table A.2 and Table A.3, we can obtain the value of function (5.3), which describes the deviations for these parameters. Even in the situations when we need to know the power spectrum with an accuracy better than the model can provide, we should keep in mind that the deviations of the model from the data have specific functional form (5.3) that can be distinguished from physical phenomena, for example QPOs.

The use of the model requires Monte Carlo simulation of a sufficient number of events. For convenience, we interpolated the  $P_k$  coefficients of simulated data for various rates and binning with a parabola. Figure 5.29 shows the parabolic least squares fit to the  $P_1$  values and the residuals of the fit in the 0-4100 Hz rates range. Figure 5.30 shows the parabolic least squares fit to the  $P_2$  values and the residuals of the fit in the same range. Table 5.6 and Table 5.7 list the results of the fits for various binning. The values in the Table 5.6 and Table 5.7 can be used to calculate  $P_1$ ,  $P_2$ , and the noise power spectrum according to (5.2). The deviations of the values of  $P_k$  obtained by the interpolation from the ones describing the model are much smaller than the deviations of the model from the data (see Figure 5.29b).

For low rate sources, a convenient method to describe the power spectrum of the noise is to use the analytical formula for extended deadtime

$$P_j^{noise} = P_1 + P_2 \cos \frac{2\pi j}{N} = \left[ 2 - 4r_o \tau_0 \left( 1 - \frac{\tau_0}{2t_b} \right) \right] - 2 \frac{N-1}{N} r_o \tau_0 \left( \frac{\tau_0}{t_b} \right) \cos \frac{2\pi j}{N}. \quad (5.7)$$

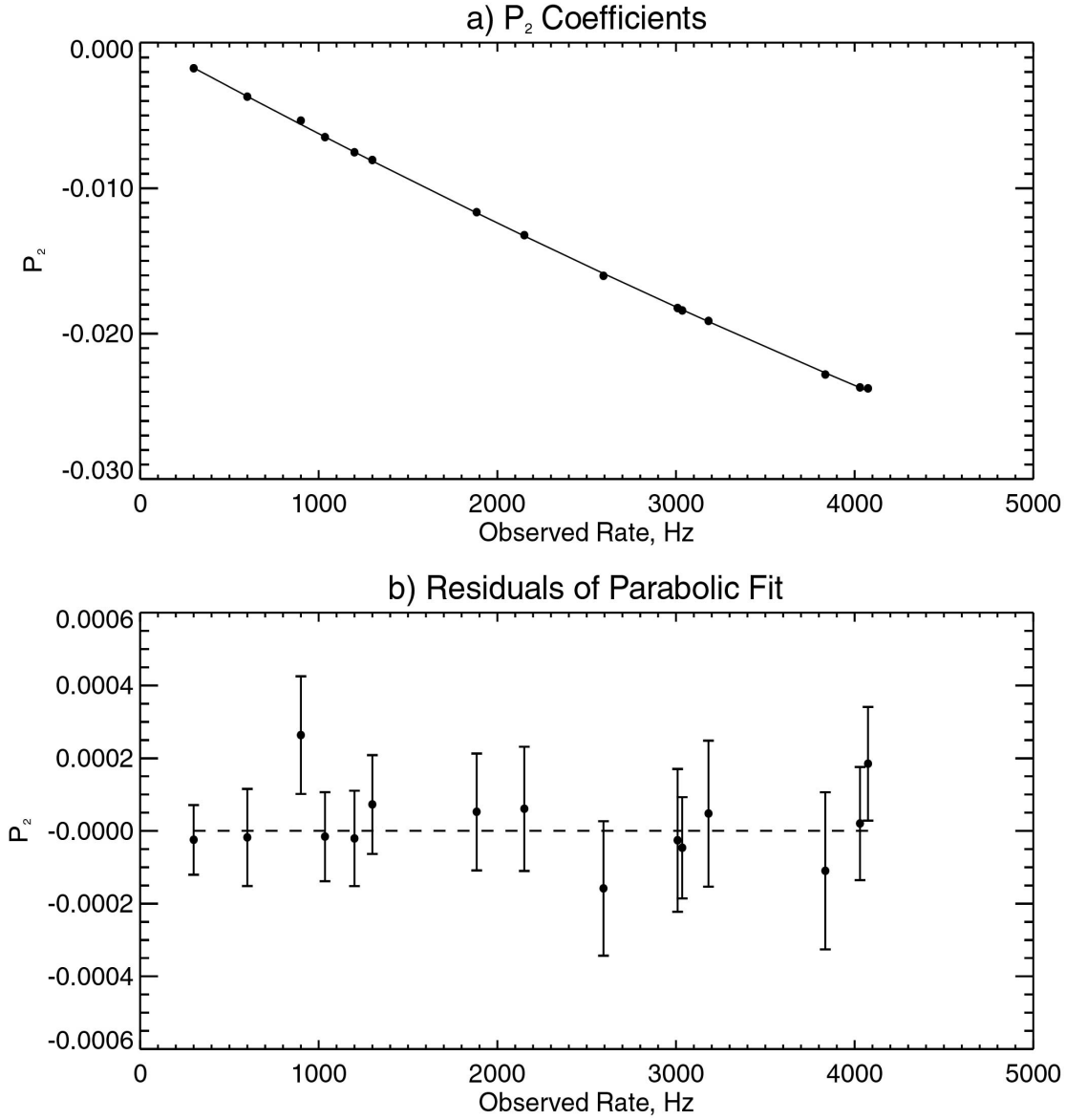


Figure 5.30 a) Parabolic fit to the coefficients  $P_2$  for the simulated data. The error bars are omitted, since they are smaller than the size of the data points. b) Residuals of the fit.  $t_b = 96 \mu\text{s}$ . The deadtime used in the simulation at all rates is the detector 0 deadtime.



$t_b$ ( $\mu$ s)	a	b	c	$\chi^2 / \text{dof}$
32	$(2.20 \pm 0.02) \times 10^{-10}$	$(-4.6432 \pm 0.0005) \times 10^{-5}$	$2.00002 \pm 0.00001$	0.281
96	$(3.7 \pm 0.1) \times 10^{-10}$	$(-5.886 \pm 0.003) \times 10^{-5}$	$1.99977 \pm 0.00004$	2.048
960	$(5.2 \pm 0.4) \times 10^{-10}$	$(-6.497 \pm 0.009) \times 10^{-5}$	$2.0000 \pm 0.0001$	0.703

Table 5.6 Results of the parabolic fit.  $P_1 = ar_o^2 + br_o + c$ . 13 dof.

$t_b$ ( $\mu$ s)	a	b	c	$\chi^2 / \text{dof}$
32	$(3.10 \pm 0.03) \times 10^{-10}$	$(-1.9090 \pm 0.0008) \times 10^{-5}$	$(-4 \pm 2.) \times 10^{-5}$	0.663
96	$(1.9 \pm 0.2) \times 10^{-10}$	$(-6.70 \pm 0.04) \times 10^{-6}$	$(2.6 \pm 0.6) \times 10^{-4}$	0.184
960	$(8. \pm 5.) \times 10^{-11}$	$(-1.0 \pm 0.1) \times 10^{-8}$	$(2 \pm 2.) \times 10^{-4}$	0.684

Table 5.7 Results of the parabolic fit.  $P_2 = ar_o^2 + br_o + c$ . 13 dof.

This formula is convenient to use, because the power spectrum can be calculated for any value of rate and bin size. However, generally, this method is much less accurate than the methods described above. Figure 5.31 shows the difference between the  $P_k$  coefficients for the model and the ones calculated using (5.7) with  $t_b = 96 \mu$ s. At low rates, the discrepancy between the model and the system with extended deadtime decreases. For rates below  $\sim 500$  Hz, the discrepancy between the power spectrum described by (5.7) and the power spectrum of the simulated data is the same as between the power spectrum of the simulated data and the calibration data. We recommend using the extended deadtime formula for low rates if the accuracy is sufficient.

## 5.5 Energy-Dependent Instrumental Effect

In the previous sections of this chapter we described the results of USA on-ground calibration and arrived at a recipe (Section 5.4.7) for deadtime corrections to the power spectra. These results are valid for the power spectra of the ground data when no selection of time series based on energy is made (i.e. power spectra are calculated for all

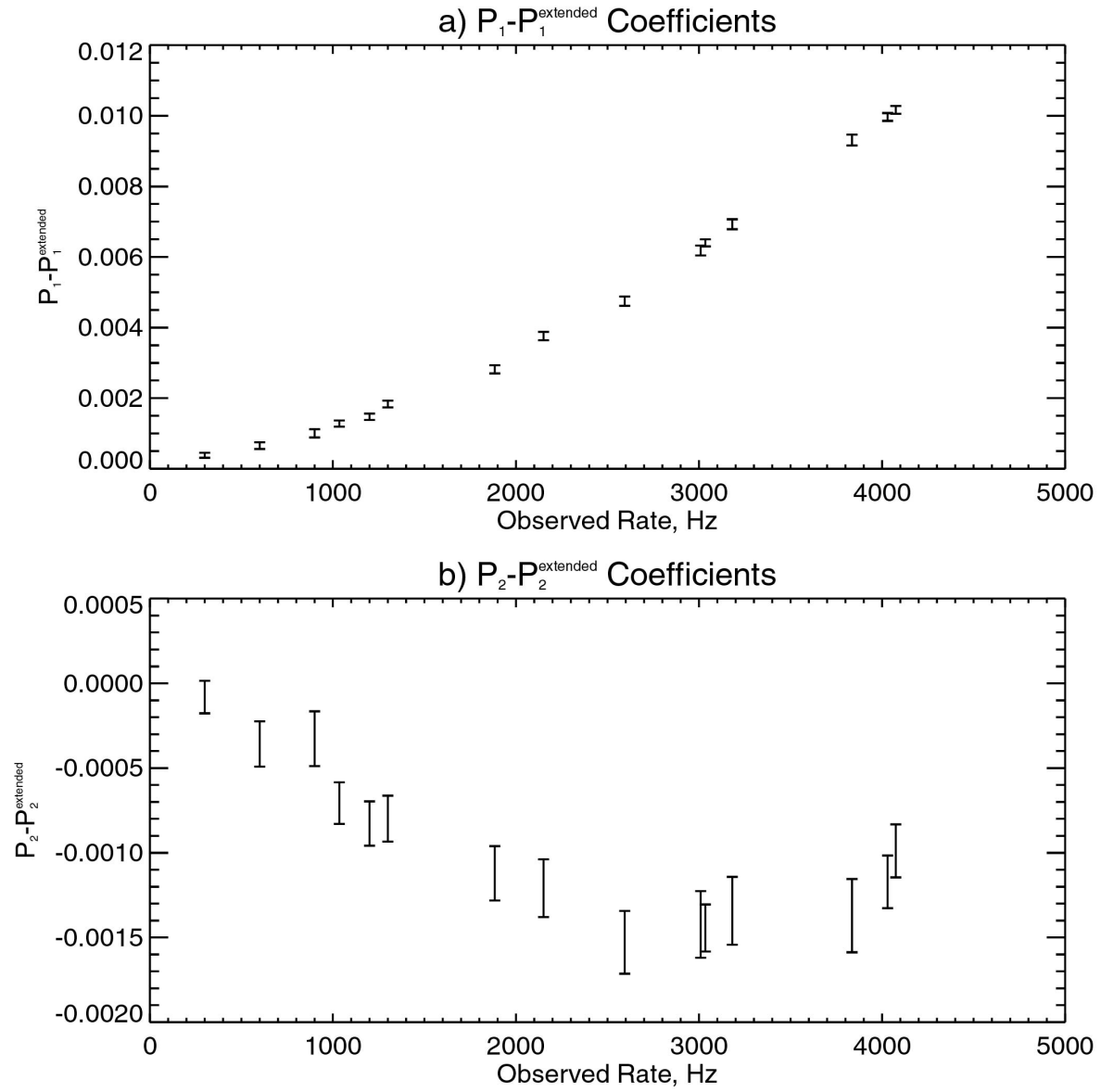


Figure 5.31 a)  $P_1 - P_1^{\text{extended}}$  coefficients. Points with error bars correspond to the simulated data.  
b)  $P_2 - P_2^{\text{extended}}$  coefficients.  $t_b = 96 \mu\text{s}$ . The deadtime used in the simulation at all rates is the detector 0 deadtime.

the energy channels combined) and the energy-dependent instrumental effect is insignificant. While looking at on-orbit data, the USA team discovered that in some cases, power spectra calculated for selected energy channels are distorted. In this section we describe our preliminary understanding of this effect. We derive a correction method, which is based on the results of previous sections. We later use the method to correct power spectra of the source of interest XTE J1859+226 (Section 6.4.1) and further check its validity by applying it to Cas A data – a Poisson X-ray source (Section 6.4.2), and Cygnus X-1 data – a well-studied BHC binary (Section 6.4.3).

### 5.5.1 The Essence of the Effect

In Section 5.5 we consider power spectra of the time series selected for the particular energy channels. Table 5.8 shows channel to energy conversion for mode 1 and mode 2 (these two data modes are used for the study of energy-dependent effect and for the analysis of celestial sources in Chapter 6).

Figure 5.32 shows the energy-dependent instrumental effect for the ground calibration data. For the details on PSD calculations, see Section 5.2.3. Only channel 6 photons were selected for the FFT. The dashed line corresponds to the expected power spectrum without the effect present. It is calculated using (5.2) with coefficients  $P_k$  calculated from Table 5.6 and Table 5.7. This effect introduces large-scale variation relative to the dashed line into the power spectrum.

The effect probably originates in the detector electronics. The current understanding (developed with Gary Godfrey, SLAC) of its cause is the following. Figure 5.4 shows a typical waveform of a signal coming from the chamber after it passes the amplifier. The output pulse has a positive part, and a negative part with the tail quickly approaching zero baseline (top curve in Figure 5.8 shows the tail of the pulse on the longer time scale and finer voltage scale). A second photon, arriving  $\Delta t$  time after the first photon, will ride on the tail of the first. We believe that the tail part of the signal waveform has small

Channel	Energy (keV)	Channel	Energy (keV)
1	1.1	8	9.1
2	2.1	9	10.5
3	3.1	10	11.9
4	4.2	11	13.4
5	5.4	12	14.9
6	6.6	13	16.5
7	7.8	14	18.1-19.8

Table 5.8 Channel to energy conversion for modes 1 and 2 [78]. The energy numbers (except the last one) are lower boundaries. Layer 1.

variation  $\delta V(\Delta t)$  of a particular shape. We estimated that the amplitude of the variation is on the order of several mV, and that it lasts for about 2000  $\mu\text{s}$  (see estimation below). The measurements described in Section 5.1.1 were too coarse to detect this variation. A baseline shift of this order will not be noticeable in Figure 5.8.

This variation in voltage translates into variation in the detected energy  $\delta E(\Delta t)$  for the photon that arrives time  $\Delta t$  after the preceding photon, i.e. the second photon can be recorded in the wrong adjacent energy channel, either one channel up or one channel down. Thus there might be an excess or lack of photons in a particular energy bin compared to the original energy distribution. The large-scale variation in the power spectrum reflects the shape of the  $\delta E(\Delta t)$  function. Note that this effect is different from the one discussed in Section 5.1.1 where the baseline shift is caused by the events with very large pulse amplitude.

The discrete autocorrelation function (ACF) framework helps better illustrate the effect. The ACF is defined as

$$ACF(\Delta t) = \sum_{i=0}^{N-\Delta t-1} x(t_i)x(t_i + \Delta t), \quad (5.8)$$

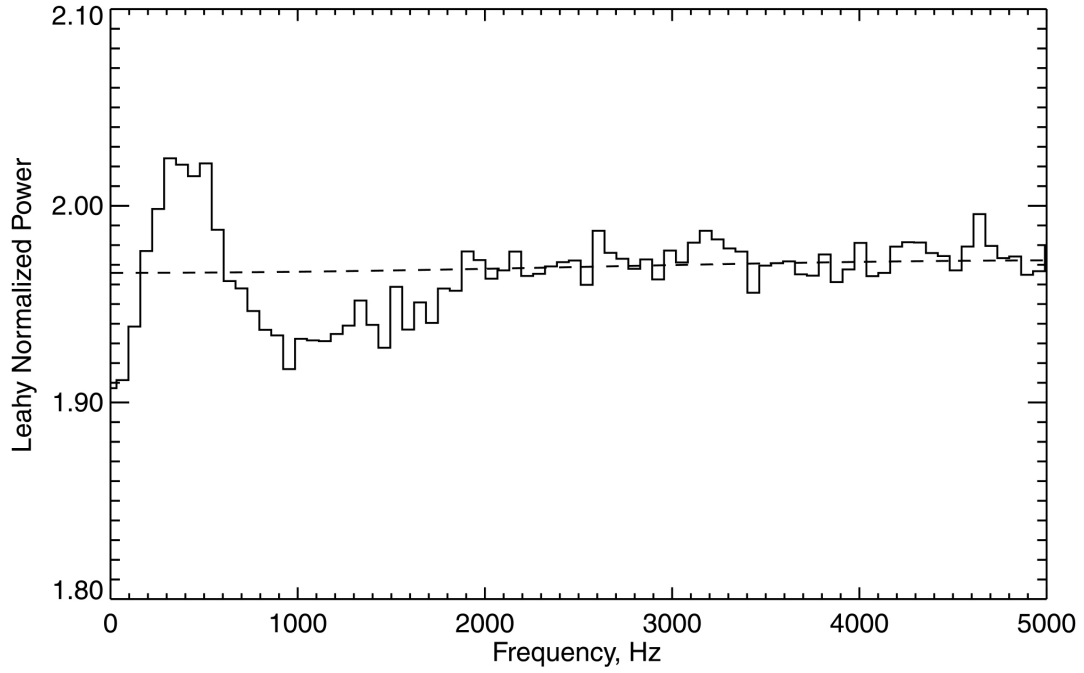


Figure 5.32 Power spectrum of the mode 2, detector 0, channel 6 ground data.  $r_o=523$  Hz.  $t_b=96$   $\mu$ s. Total exposure time 0.7 ks. Dashed line represents expected power spectrum without the energy-dependent instrumental effect present.

where  $x(t_i)$  is the binned light curve,  $N$  is the number of bins in the light curve and  $\Delta t$  is a time between bins (in multiples of the size of the bin).

Figure 5.33 shows the ACF calculated for the same data set as the power spectrum in Figure 5.32. The dashed line is a theoretical value of the ACF for the pure Poisson process calculated with the parameters of the data set. The detector deadtime, discussed in previous sections of this chapter, is ignored for this demonstration (it only causes a small depletion in ACF value in the second bin). The large-scale variation in the ACF relative to the dashed line is believed to be caused by the  $\delta V(\Delta t)$  variation. Godfrey [25] estimated that if this is the case, the difference between the ACF with the effect present (solid line) and ACF with no effect present (dashed line) in first order is proportional to

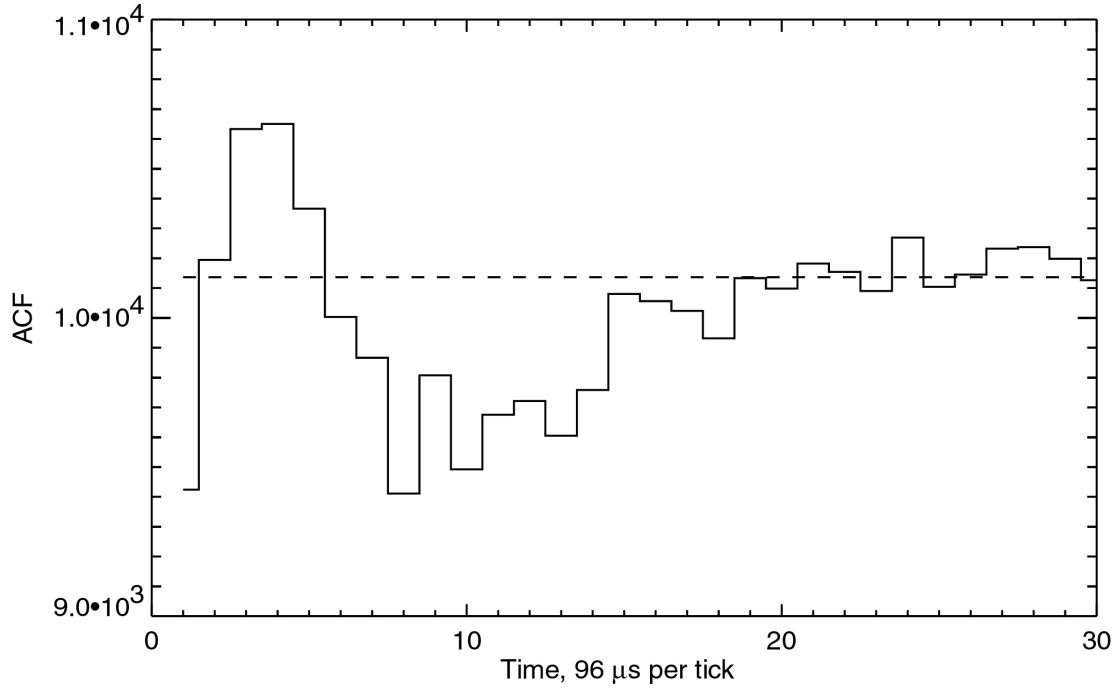


Figure 5.33 ACF. The data set is the same as in Figure 5.32.  $r_o=523$  Hz.  $t_l=96 \mu s$ .  $N_\gamma = 2 \cdot 10^5$ . First bin with  $ACF=N_\gamma$  is omitted. Dashed line represents ACF function calculated for a Poisson process with parameters of the data set. Beyond the shown time range, the data does not deviate from Poisson.

$$\Delta ACF(\Delta t) \sim \left. \frac{dr_o}{dE} \right|_E \delta E(\Delta t), \quad (5.9)$$

where  $\left. \frac{dr_o}{dE} \right|_E$  is the derivative of the observed rate with respect to photon energy and  $\delta E(\Delta t)$  is the energy variation. The derivation of (5.9) assumes that the variation of the baseline,  $\delta V(\Delta t)$ , has the same shape after every signal. Based on (5.9), the large-scale variation in Figure 5.33 has the same shape as  $\delta E(\Delta t)$ , and, therefore, the same shape as the varying baseline  $\delta V(\Delta t)$ . The amplitude of the variation  $\delta E(\Delta t)$  (estimated to the first order by Godfrey [25] based on the value of the amplitude of the large-scale

variation in Figure 5.33), is about 20 eV or roughly 4.5 mV for the amplitude of  $\delta V(\Delta t)$ . The time scale of the variation is about 20 bins in Figure 5.33 or about 2000  $\mu$ s.

The power spectrum (Figure 5.32) shows a large-scale variation of a similar shape to the ACF, which is an inverse Fourier transform of a power spectrum.

The presence of the derivative with respect to energy in (5.9) means that the effect goes away in the case of a flat energy spectrum. It is also not present in the case of energy spectrum that has perfectly symmetrical shape and when all the energies are combined, since negative derivatives cancel out positive ones. The steeper the energy spectrum, the bigger the effect. All of the above properties are seen in the data. In particular, the ground data has an almost symmetrically shaped energy spectrum of  $^{55}\text{Fe}$ , which is centered on channel 5. Thus the effect is very small when all the energies are combined (see Section 5.4.3). When we select only channel 6 photons, the effect is present (Figure 5.32, Figure 5.33). When we select only channel 4 photons, the derivative changes sign, and the variation in ACF and in power spectrum also changes sign (see Figure 5.34).

The variation  $\delta V(\Delta t)$  can depend on parameters, such as counting rate, energy of the selected photons, and possibly others. It also can differ for each photon. The data indicates that the shape of this function is different for the observations with different parameters. Further verification of our understanding of this effect would involve a careful measurement of the baseline variation for various pulse heights using the brass board electronics.

Currently, we do not have a good enough understanding of this effect to be able to simulate it. Instead, we chose a phenomenological approach to the correction of power spectra for the energy-dependent instrumental effect. The approach is discussed in the next section.

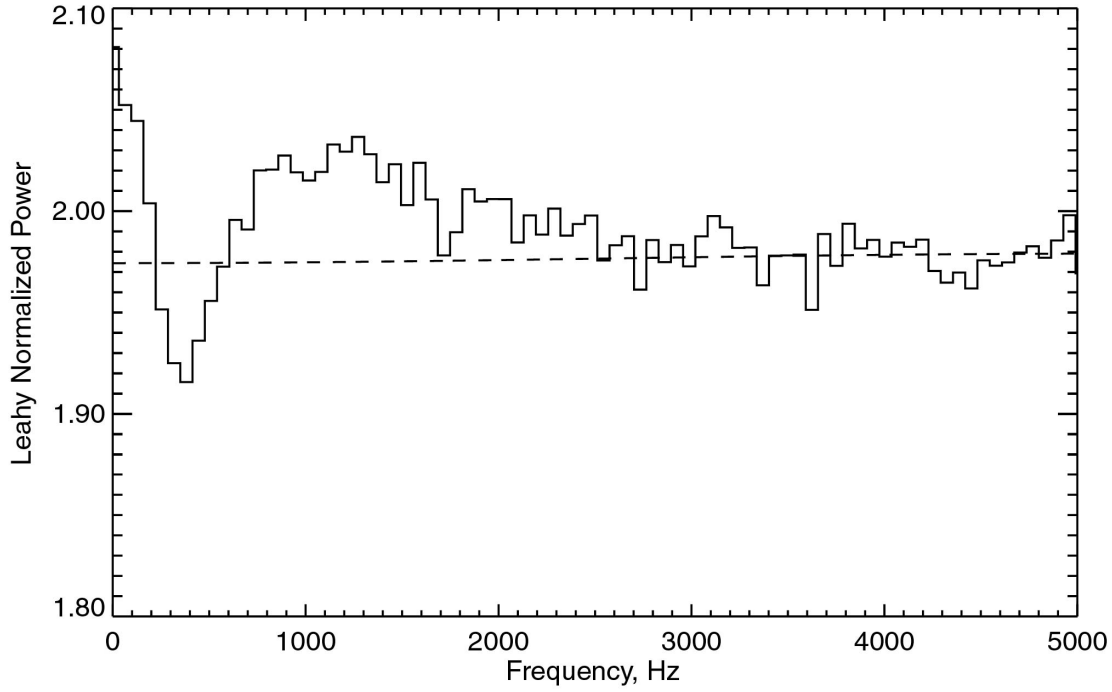


Figure 5.34 Power spectrum of the mode 2, detector 0, channel 4 ground data.  $r_o=394$  Hz.  $t_b=96$   $\mu$ s. Total exposure time 0.7 ks. Dashed line represents expected power spectrum without the energy-dependent instrumental effect present.

### 5.5.2 Procedure for the Deadtime Correction to Energy-Selected Power Spectra

The variation in the power spectra due to the energy-dependent instrumental effect discussed in the previous section has a characteristic functional form. We used ground calibration data to find the functional form  $P^{noise}(f)$  that best describes Poisson noise with deadtime and instrumental effects. This function with parameters depending on a particular observation determines the Poisson noise component in the power spectrum of the celestial source. The parameters are obtained by fitting the power spectra with  $P^{noise}(f)$  in the high-frequency region starting from 300 Hz or higher. This region for BHC binaries does not contain the power from the sources themselves (at least to



detectable levels from the RXTE and USA experiments). After determining the parameters of  $P^{noise}(f)$ , we subtract the noise from the entire power spectrum. The procedure of reconstructing the shape of the noise in the power spectra by fitting high-frequency region (above several hundred Hz) with a phenomenological function was used by Wen [100] to correct for the unknown instrumental effect in the High Energy Astrophysical Observatory (HEAO) A-1 data, and by Jernigan et al. [31] to correct for the deadtime and unknown background effects in RXTE data.

The following function was used to fit ground calibration data

$$P^{noise}(f) = P^{energy}(f) + bP^{other}(f), \quad (5.10)$$

where  $f$  is the frequency,  $b$  is a parameter,  $P^{energy}(f)$  is the noise component due to the energy-dependent instrumental effect and  $P^{other}(f)$  is the noise component due to the USA deadtime and other instrumental effects discussed in Sections 5.1-5.6.

The  $P^{other}(f)$  describes Poisson power spectrum in the presence of non-extended deadtime and same time events (STE) introduced by the Detector Interface Board (DIB), and (according to Section 5.4.6 and 5.4.7) in the case of  $t_b \geq \tau$  can be expressed as

$$P^{other}(f) = P_1 + P_2 \cos(2\pi f t_b), \quad (5.11)$$

where coefficients  $P_k$  are calculated from the values in Table 5.6 and Table 5.7. The value of parameter  $b$  in (5.10) does not exceed 1.001 for all the fits we performed and is consistent with the accuracy in determining coefficients  $P_k$  (see Section 5.4.6). Note that at high frequencies,  $P^{noise}(f)$  is approaching  $bP^{other}(f)$ . Sometimes, at high frequencies  $P^{noise}(f) = P^{other}(f)$  with a good accuracy, in which case parameter  $b$  can be omitted.

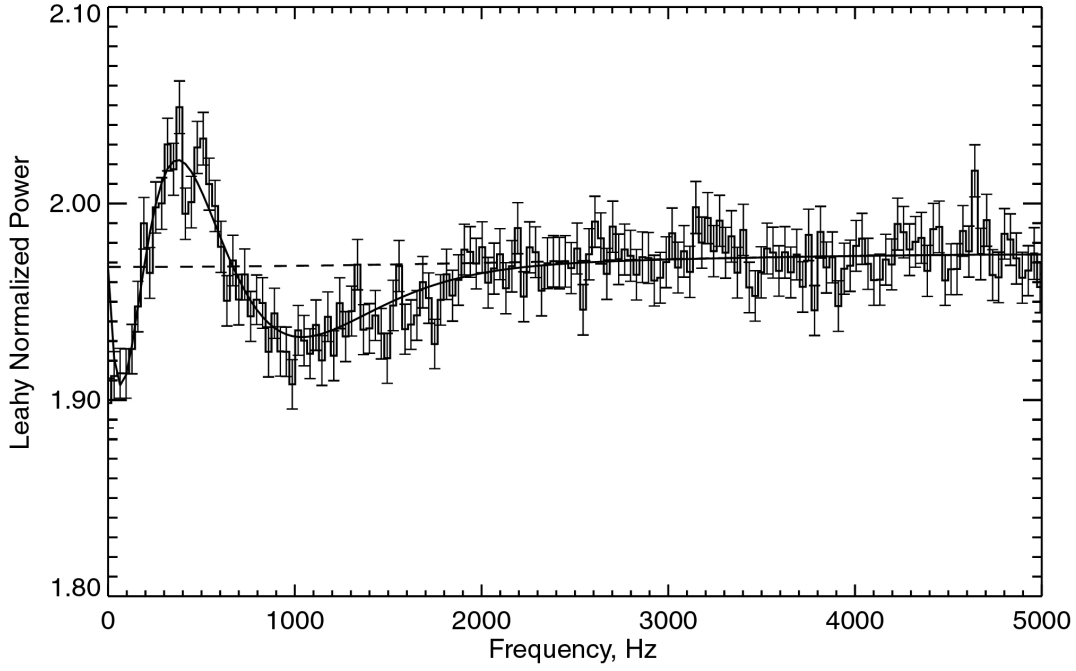


Figure 5.35 Power spectrum of the mode 2, detector 0, channel 6 ground data fitted with (5.12).  $r_o=523$  Hz.  $t_b=96$   $\mu$ s. Total exposure time 0.7 ks. Fitting range: 0-5000 Hz. Solid line: fit. Dashed line:  $bP^{other}(f)$ .

A functional form for  $P^{energy}(f)$  was chosen, by trail and error, to best describe the shape of the energy-dependent instrumental distortion with as few as possible parameters.

The resulting  $P^{noise}(f)$  is equal to

$$P^{noise}(f) = a_0 e^{-a_1 f} f(f - a_2)(f - a_3) + bP^{other}(f), \quad (5.12)$$

where  $a_k$  and  $b$  are parameters.

Figure 5.35 shows the least squares fit to the ground calibration data with function (5.12). The parameters of the fit are listed in Table 5.9. The fit gives good result everywhere but at the lowest frequencies. Figure 5.36 shows the same fit as in Figure 5.35 expanded for the lower frequencies. Below  $\sim 30$  Hz the data deviates from the fit. This is due to the fact that we chose the fitting function that gives good fit in the  $\sim 40$ -5000 Hz range. The

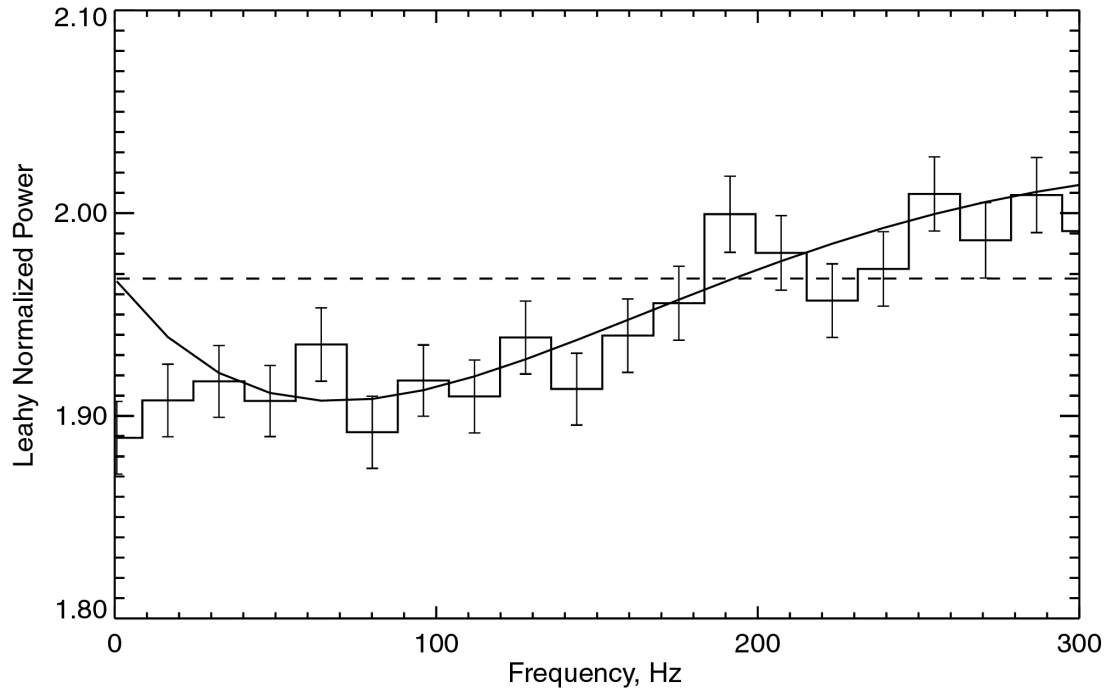


Figure 5.36 Same as in Figure 5.35, but zoomed into the lower frequency region.

deviation at the frequencies below  $\sim 30$  Hz does not present a problem since in this work we are interested in correcting power spectra in frequency region  $\sim 40$ -5000 Hz.

$a_0$	$a_1$ (s)	$a_2$ (Hz)	$a_3$ (Hz)	$b$	$\chi^2 / 178$
$(-1.7 \pm 0.2) \times 10^{-8}$	$(4.8 \pm 0.1) \times 10^{-3}$	$192 \pm 8$	$668 \pm 16$	$1.0009 \pm 0.0007$	1.10

Table 5.9 Results of the fit to the ground data with (5.12).

If we fix the parameter  $a_1$ , it becomes easy to reconstruct the shape of the noise by fitting data only in high-frequency region. We set  $a_1 = 0.0048$  (see Table 5.9) for all the subsequent fits. At the same time to be able to fit all of the data, we have to allow for the rescaling of the frequency.

The final fitting function is

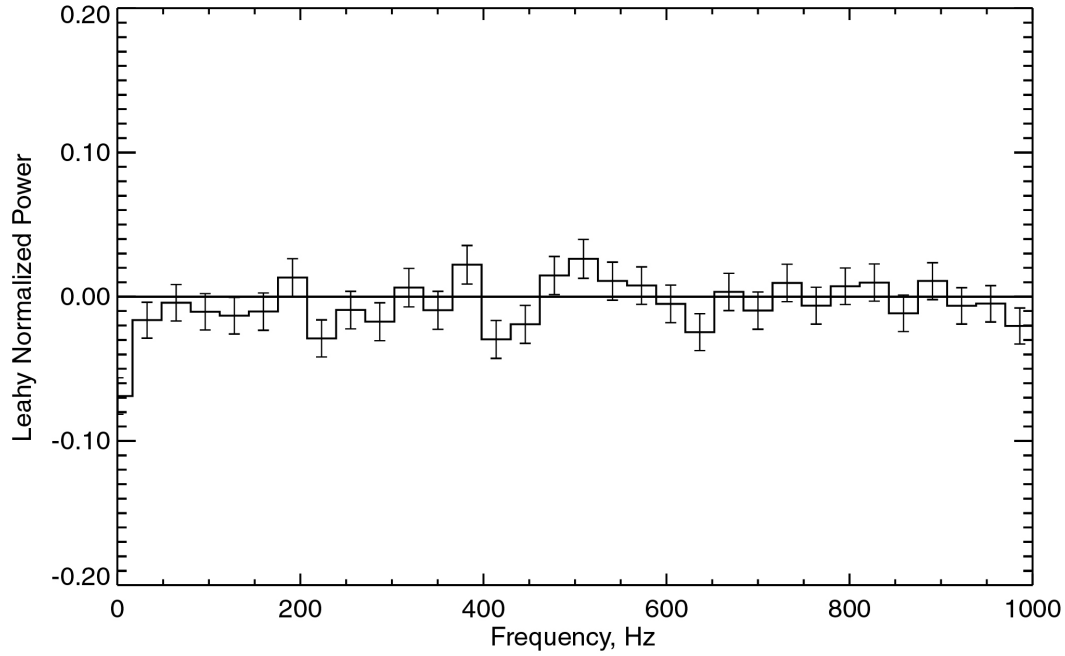


Figure 5.37 Residuals of the fit to the power spectrum with (5.13). Same data set as in Figure 5.35. Fitting range: 300-5000 Hz. The residuals are consistent with zero in  $\sim 30$ -5000 Hz region.

$$P^{noise}(f) = c_0 e^{-0.0048 f'} f' (f' - c_1)(f' - c_2) + b P^{other}(f), \quad (5.13)$$

$$f' = c_3 f$$

where  $c_k$  are parameters. This function is used to describe the noise. The parameters are determined by fitting the power spectra in the frequency range from 300 Hz to 5000 Hz.

Figure 5.37 shows residuals of the fit to the power spectrum of the ground data in the range from 300 Hz to 5000 Hz. The fit parameters are listed in Table 5.10. These parameters are consistent within errors with parameters in Table 5.9. The residuals are consistent with zero in  $\sim 30$ -5000 Hz region ( $\sim 40$ -300 Hz is the region of interest for high-frequency QPO studies). We use function (5.13) to fit the data sets with the counting rates similar to the ground data or less (below  $\sim 500$  Hz). This method may not work for

$c_0$	$c_1$	$c_2$	$c_3$ (s)	$b$	$\chi^2/304$
$(-1.7 \pm 0.4) \times 10^{-8}$	$172 \pm 69$	$644 \pm 44$	$0.97 \pm 0.06$	$1.0010 \pm 0.0007$	0.94

Table 5.10 Results of the fit to the ground data with (5.13).

higher counting rates, since at high rates the pileup effects are stronger and might exhibit more complex behavior.

## 5.6 Future Work

Future on-orbit studies are critical in our understanding of the USA timing as issues of background, and large ionization events play a role in space at high counting rates.

The results of the on-ground calibration have to be verified by the on-orbit timing calibration at high counting rates close to the ones observed in the on-ground calibration tests. This will allow one to compare the on-ground calibration data with the on-orbit calibration data and to investigate the on-orbit background effects on the deadtime: 1) The effect of the perimeter veto and the coincidence veto events. 2) The effect of large energy events (see Section 5.1.2). Most importantly, further verification of our understanding of the energy-dependent instrumental effect is needed. It would involve a careful measurement of the baseline variation for various pulse heights using the brass board electronics, and developing more general correction method based on the simulation of this effect in the power spectrum.

More subtle effects can be further investigated once the questions of influence of the background and the origin of energy-dependent instrumental effect are answered. With better statistics at several rates for the remaining detector, we can find if the non-extended deadtime in the model depends on the counting rate (Section 5.4.1). We should investigate whether the DIB introduces event loss (Section 5.1.2). Also, the model, that takes into account the one-shot stretching time shortening, might produce better fit to the data. However, these are higher order effects and might turn out to be insignificant.

## **CHAPTER 6: DETECTION OF HIGH-FREQUENCY VARIABILITY AND OTHER STUDIES OF BLACK HOLE TRANSIENT XTE J1859+226**

In this chapter we demonstrate that a BHC transient XTE J1859+226 shows excess power in the frequency range from 40 Hz to 300 Hz. The typical power spectrum of a BHC binary in the frequency range from several Hz to 300 Hz can be described as a power law or a broken power law. We show that the power in XTE J1859+226 in this range lies above the power law continuum. We show an analysis of Cas A and Cygnus X-1 power spectra to verify the validity of the noise correction method (Section 5.5.2) for the on-orbit data. We look at the low-frequency variability of XTE J1859+226 ( $\sim 5$  Hz QPO) and at the energy dependence of the temporal properties of the source. At the end we discuss the implications of our results.

### **6.1 X-ray Nova XTE J1859+226**

An X-ray nova XTE J1859+226 was discovered on October 9, 1999 by the All Sky Monitor (ASM) aboard the Rossi X-ray Timing Explorer (RXTE) (Wood et al. [105]). The outburst of the nova was simultaneously monitored by a number of radio, optical, X-ray and Gamma-ray telescopes. The outburst lasted for about 150 days, and was observed

with USA for two months on average 4 times a day (see Section 6.3 for the details on USA observations).

The most recent optical observations revealed a possible binary period of 18.7 hours [47] (the previously reported period of 9.15 hours [23] may be a sub-harmonic). The hard X-ray flux extending to 200 keV was measured by the Burst and Transient Source Experiment (BATSE) aboard the Compton Gamma-Ray Observatory (CGRO) [48], and by the Satellite per Astronomia X (BeppoSAX) [16]. The spectral states of the transient evolved during the outburst from the low state to the very high state, then to the high state, and back to the low state at the very end of the outburst [22]. The energy spectrum through the outburst could be modeled as a combination of blackbody component and power law with reflection component [22].

The low and very high states were accompanied by QPOs in a wide range of frequencies. Early in the outburst  $\sim 0.45$  Hz QPO was reported by the RXTE Proportional Counter Array (PCA) [44], and later a  $\sim 5.5$  Hz QPO by BeppoSAX [16]. Further analysis of PCA/RXTE data by Markwardt et al. [45] and by Cui et al. [15] revealed the occurrence of high-frequency QPOs during the outburst. Their frequency varied during one day of observations in the range from  $\sim 80$  Hz to  $\sim 200$  Hz [15]. As will be shown in this work, the USA experiment detected both low-frequency and high-frequency QPOs during the XTE J1859+226 outburst.

XTE J1859+226 is tentatively classified as a BHC transient based on its timing and spectral characteristics, such as the evolution and character of spectral states during the outburst, strong variability accompanied by low-frequency QPOs, and a hard power-law photon spectrum extending to 200 keV [90]. At this point, there are no dynamical mass measurements of the compact object, which prevents a strong identification of this source as a black hole. However, the spectral and timing behavior of XTE J1859+226 is

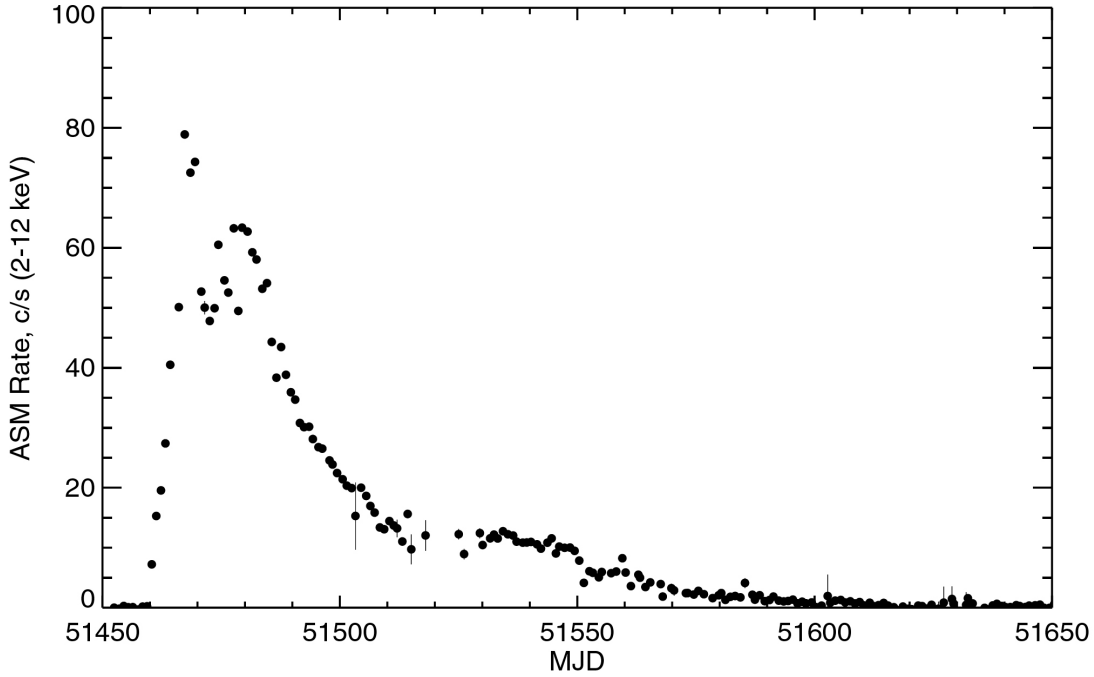


Figure 6.1 The 2-12 keV daily averaged ASM light curve of XTE J1859+226 during the outburst. Modified Julian Date 51450 corresponds to September 29, 1999.

remarkably similar to many other BHC transients, for example GRO J1655-40 [72], [51] - the source with an established mass of  $7.0 \pm 0.2 M_{\odot}$  [61].

## 6.2 Light Curve of the Source

Figure 6.1 shows the XTE J1859+226 X-ray light curve measured by ASM/RXTE during the outburst. The overall shape of the outburst may be described as a fast rise and an exponential decay (FRED), and is common for X-ray novae [9]. Cui et al. [15] estimate the rise time from 10% to 90% of the peak flux to be about 5 days and e-fold decay time about 23 days. At its maximum the source reached 1.5 crab (1 crab = 74 ASM c/s) on MJD 51467 in the range 2-12 keV (Figure 6.1 shows the daily averaged counting rate, which is smaller than 1.5 crab on this date). The source was flaring near the peak of the outburst. A secondary maximum is visible between MJD 51515 and MJD 51540. The



presence of a secondary maximum, as well as the values of the rise and decay time constants, is typical of many X-ray BHC transients with FRED type light curves [91].

### **6.3 Observations and Data Analysis**

The USA experiment observed the outburst of XTE J1859+226 from October 15, 1999 (MJD 51466) to December 16, 1999 (MJD 51528). Overall, 208 pointed observations, uniformly spaced throughout the outburst, were made (on average about four observations per day). Due to the nearly polar orbit of USA, the usable time from each individual observation varied in length from 300 to 1100 seconds.

For all observations but three, event mode 1 was used (see Section 5.2.1 for the detailed description of USA data modes). Three observations on October 15 and 16, 1999 used event mode 2.

To search for QPOs, we performed an FFT on the data (4.1). The power spectra were normalized using the Leahy normalization (4.2).

For the analysis, the data was divided into many equal time segments. The Fourier power spectra were then calculated for each of these segments and averaged over the number of segments. The way data was divided into equal segments differed for mode 2 and mode 1 data.

Mode 1 data was divided into equal length segments of 0.197 seconds. We ensured that these segments never overlapped with the gaps at the end of one-second science frames resulting from rate saturation (see Section 5.2.2). The particular length of the segment was chosen to utilize most of the data, and thus increase sensitivity to the signal. Also, the segments started 10 ms from the beginning of the frame to avoid the small millisecond gaps sometimes seen in the data in the beginning of the frame (Section 5.2.2). Mode 1 data was used only for the high-frequency QPO search. Since mode 1 data allows only shorter than 1 second Fourier transforms, it cannot provide sufficient frequency resolution to detect low-frequency QPOs. To search for a small

signal at high frequencies, we combined about 50 observations together (14.3 ks total) and calculated a single power spectrum of those observations. USA did not collect enough statistics to detect the signal with one day's worth of observations due to the short duration of a USA observation and limited effective area of the instrument. RXTE with more effective area and a much longer single observation time was able to detect a signal in one observation (on the order of 3 ks).

The mode 2 data was continuous (with no gaps in it), and was divided into 31 second segments for Fourier transform. This data was used for the low-frequency and high-frequency QPO analysis. The mode 2 data used for the high-frequency QPO analysis was divided into segments in the same way as the mode 1 data.

We performed an energy-dependent timing analysis by calculating power spectra from time series selected in various energy ranges. USA has 14 energy channels covering the range from 1.1 keV to 19.8 keV in modes 1 and 2. Refer to Table 5.8 for channel to energy conversion.

We subtracted from the power spectra the power due to the Poisson noise with corrections for the instrument deadtime and other instrumental effects. These corrections are described in the next section.

## **6.4 High-Frequency Variability in XTE J1859+226**

### **6.4.1 Power Spectra of XTE J1859+226**

In order to search for high-frequency signals, we had to combine power spectra from many observations, since there is not enough statistics in one observation to detect weak signals. We selected photons in energy channels 4 to 14, since the strength of high-frequency QPOs in BHC transients is known to increase with energy [15], [52], [69], [70], [73]. We combined 50 observations (total exposure time 13.4 ks) covering the period from October 15, 1999 (MJD 51466) to November 4, 1999 (MJD 51486). Observations are listed in Table A.4 of the Appendix. During this period, the source was

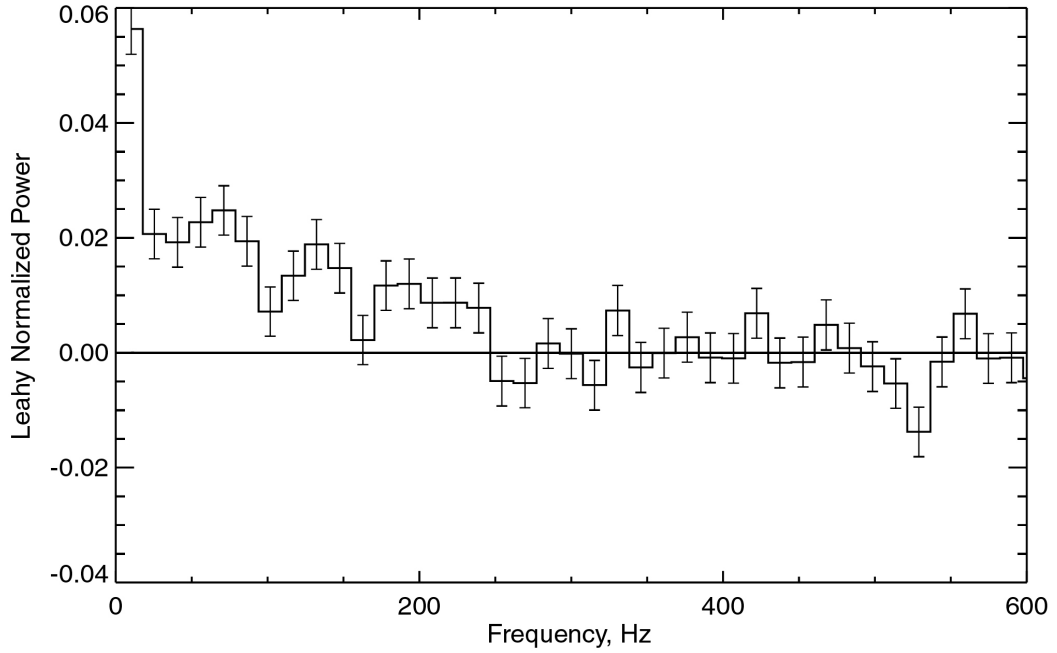


Figure 6.2 Noise-subtracted power spectrum of the mode 1 XTE J1859+226 data. Energy range: 4.2-19.8 keV. Very high state.  $r_o=465$  Hz.  $t_b=96$   $\mu$ s. Total exposure time 13.4 ks. Range used to determine the noise: 300-5000 Hz. Range used to calculate rms amplitude: 40-300 Hz.

in a very high (VH) state [22], which has been associated with strong QPOs [14]. The particular number of observations was chosen for convenience (the limit on the number of observations in FTOOLS 4.2 program powspec). These observations cover the highest rate data in a very high state, stopping four days short of the transition to the high state on November 8, 1999. The counting rate for the selected set of data is very close to the counting rate of the Cygnus X-1 data set used to verify the noise correction method (see Section 6.4.3); the energy range was the same.

Figure 6.2 shows the noise-subtracted power spectrum of XTE J1859+226. The noise power was determined using the procedure described in Section 5.5.2 (see Table 6.1 for the noise parameters). There is a distinct excess of power for the XTE J1859+226 data in the  $\sim 40$ -300 Hz region. RXTE detected [9] a high-frequency QPO with one day's worth of observations in this frequency range. During four observations on October 18, 1999 (MJD 51469), RXTE reported that the QPO appeared in the first two observations,

Fit	$c_0$	$c_1$	$c_2$	$c_3$ (s)	$b$	$\chi^2 / \text{dof}$
1	$(-3.1 \pm 0.7) \times 10^{-9}$	$180 \pm 72$	$936 \pm 67$	$1.09 \pm 0.09$	1.	1.19
2	$(-2. \pm 1.) \times 10^{-9}$	$79 \pm 162$	$658 \pm 86$	$0.9 \pm 0.1$	$1.0012 \pm 0.0002$	1.11
3	$(-2.1 \pm 0.3) \times 10^{-9}$	$53 \pm 58$	$608 \pm 37$	$0.66 \pm 0.04$	$1.0007 \pm 0.0002$	1.01
4	$(-1.9 \pm 0.5) \times 10^{-9}$	$87 \pm 83$	$653 \pm 50$	$0.77 \pm 0.06$	$1.0007 \pm 0.0001$	0.99

Table 6.1 Results of the fit to the on-orbit data with (5.13). 1. XTE J1859+226 in a very high state. 305 degrees of freedom. 2. XTE J1859+226 in a high state. 304 dof. 3. Cas A. 304 dof. 4. Cygnus X-1. 302 dof.

changing its frequency from  $187_{-11}^{+14}$  Hz to  $82_{-26}^{+56}$  Hz, disappeared during the third observation, and reappeared during the last observation at  $150_{-28}^{+17}$  Hz. These QPOs most probably originate from a single process that varies in period on hour timescales. Figure 6.3 shows the high-frequency QPO ( $187_{-11}^{+14}$  Hz) in the power spectrum of the first RXTE observation (Cui et al. [15]).

Figure 6.2 shows the USA cumulative power spectrum over 20 days of the outburst. There appear to be three distinct peaks at three frequencies in the power spectrum. (Although this statement is open to interpretation, since the peaks may be statistical fluctuations.) Also, this fact does not necessarily mean that the QPOs most often appear at those frequencies, it might be the result of the particular selection of observations. The power spectrum shown in Figure 6.2 is consistent with the power spectrum obtained by Markwardt et al. [45] who, similarly, combined 80 RXTE observations to obtain the power spectrum.

We calculated the fractional rms amplitude of the signal from 40 Hz to 300 Hz using the formula [95]

$$RMS = 100\% \sqrt{\frac{I}{r_o}}, \quad (6.1)$$

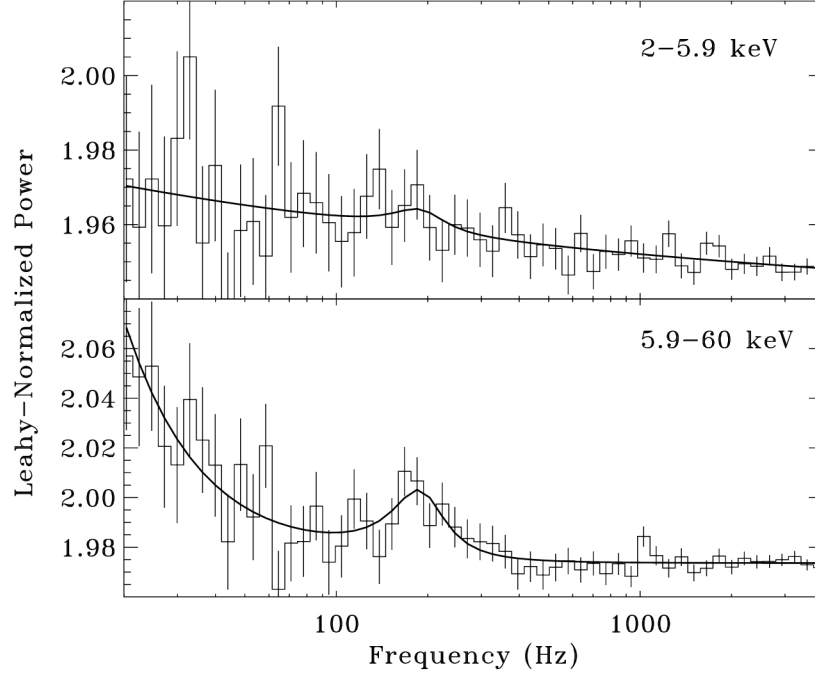


Figure 6.3 Power spectra of XTE J1859+226 RXTE data in two energy bands courtesy Cui et al. [15]. The solid lines represent the best-fit model to the data. The QPO frequency in the hard band is  $187^{+14}_{-11}$  Hz. The power spectra are not corrected for deadtime.

where  $I$  is the integrated Leahy-normalized noise-subtracted power spectrum over the region of interest, and  $r_o$  is the mean observed counting rate. The fractional rms amplitude is  $7.7 \pm 0.4\%$ . The statistical significance of the signal detection is therefore above  $20 \sigma$ .

To obtain the characteristic frequencies of the process that causes the excess power, we fitted the power spectrum with a sum of a power law  $Af^\alpha$  and three Lorentzian functions

$$L(f) = \frac{1}{\pi} I \frac{\Gamma/2}{(f - f_{qpo})^2 + (\Gamma/2)^2}, \quad (6.2)$$

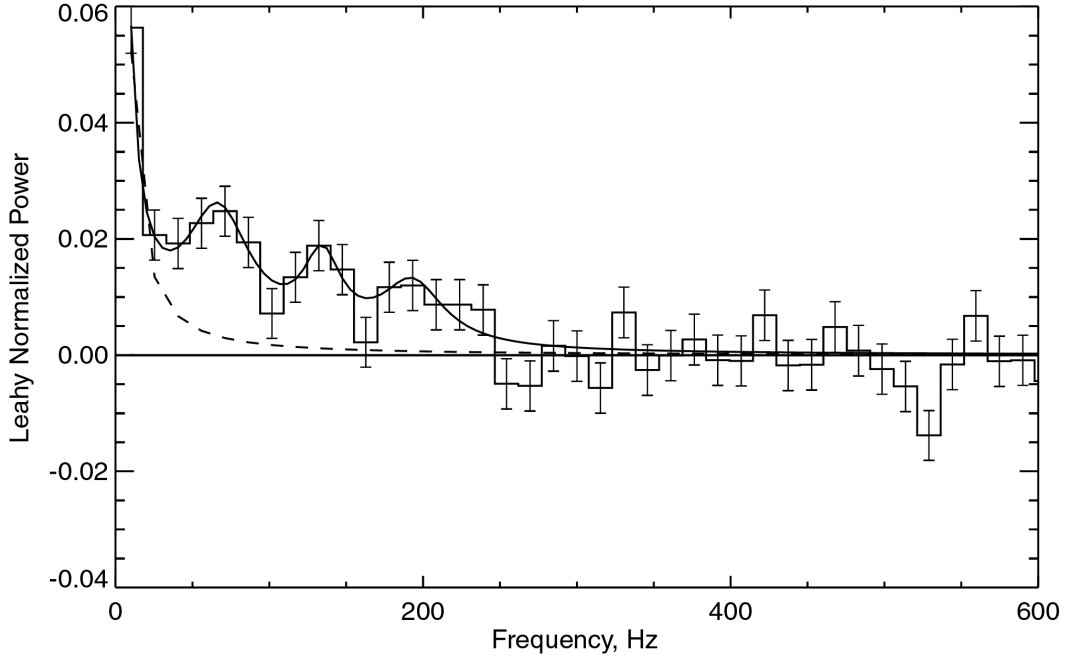


Figure 6.4 Noise-subtracted power spectrum fitted with the three Lorentzian functions and the power law. Same data set as in Figure 6.2. Fitting range: 5-500 Hz. Solid line is a fit. Dashed line is a power law only.

where  $f$  is the frequency,  $f_{qpo}$  is the QPO centroid frequency,  $I$  is the area under the Lorentzian function, and  $\Gamma$  is the full width at half maximum (FWHM). Figure 6.4 shows the fit and Table 6.2 lists the results of the fit. The parameters of the power law fit below  $\sim 30$  Hz do not reflect the real low-frequency power law since all of the low-frequency power is combined in one frequency bin. Also, the systematic error below  $\sim 30$  Hz due to uncertainty in the deadtime correction method for the frequencies below  $\sim 30$  Hz (see Figure 5.36) is not considered (it is estimated to be on the order of 0.01 for the first bin in Figure 6.4).

To trace the evolution of the QPO throughout the outburst, we calculated a power spectrum combining 50 observations from November 10, 1999 (MJD 51492) to November 22, 1999 (MJD 51504). Observations are listed in Table A.4 of the Appendix. During this period the source was in the high state [22], where variability is not

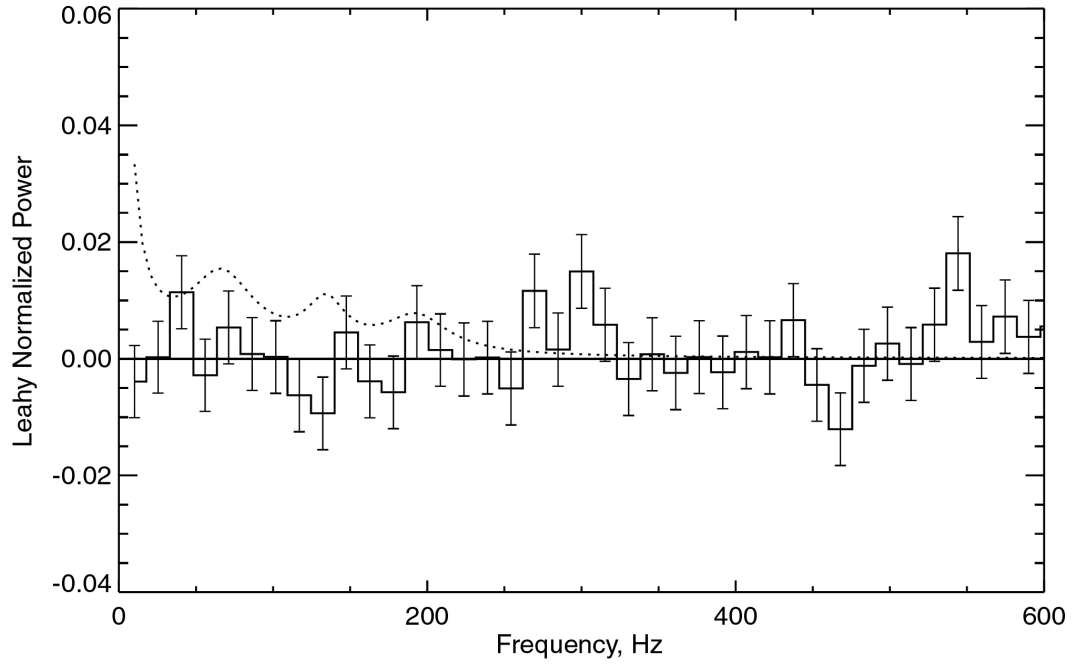


Figure 6.5 Noise-subtracted power spectrum of the mode 1 XTE J1859+226 data. Energy range: 4.2-19.8 keV. High state.  $r_o=274$  Hz.  $t_b=96$   $\mu$ s. Total exposure time 6.6 ks. Range used to determine the noise: 300-5000 Hz. High-frequency variability is weaker or absent in the high state. The dotted line shows how the signal with the same rms amplitude as in the very high state would have looked like.

expected [14]. Figure 6.5 shows the noise-subtracted power spectrum of XTE J1859+226 in the high state. The noise power was determined using the procedure described in Section (5.5.2) (see Table 6.1 for the noise parameters). If a signal with the same rms amplitude and the same structure as in the very high state were present during the high state, it would have 1.7 times less integrated power in the 40 to 300 Hz frequency range (due to the lower counting rate compared to the very high state), and would still be clearly observed (see dotted line in Figure 6.5).

We therefore conclude that the QPO in XTE J1859+226 is significantly weaker or absent in the high state.

The high-frequency QPO rms variability of XTE J1859+556 is the strongest detected so

QPO Number	Freq. (Hz)	FWHM (Hz)	Rms (%)
1	67±5	53±22	6. ±1.
2	134±6	31±5	3.7±0.3
3	193±9	50±27	4.3±0.9

Table 6.2 Results of the QPO fit with three Lorentzian functions and the power law. Power law  $Af^\alpha$  parameters are:  $A=1.6\pm1.7$ ,  $\alpha=-1.5\pm0.5$ . The  $\chi^2$  for 23 degrees of freedom is 1.06. Energy range: 4.2-19.8 keV.

far in BHC transients in the high-frequency region (see Table 2.2).

### 6.4.2 Power Spectra of Cas A

Cas A is a supernova remnant that emits Poisson distributed X-ray radiation. We analyzed Cas A data to test the validity of our noise correction method (Section 5.5.2). We analyzed 48 observations (total exposure time 22.7 ks) of mode 1 Cas A data. The analysis was similar to that of XTE J1859+226 described in Section 6.3. We selected channel 2 photons to reproduce the instrumental effect. We fitted the data with function (5.13) in the frequency range from 300 Hz to 5000 Hz. The fit was consistent with the fit to the same data that starts from 0 Hz. The fit is shown in Figure 6.6, and the residuals of the fit on a different frequency scale are shown in Figure 6.7. The parameters of the fit are listed in Table 6.1

The residuals are consistent with zero, as expected for a Poisson source. The residuals are consistent with zero in ~0-5000 Hz region. As with the on-ground data, we were able to achieve good results in the 40 Hz to 300 Hz region in particular.

The function  $P^{noise}(f)$  (5.13) describes the Cas A power spectrum well. This function takes into account the energy-dependent instrumental effect, electronics non-extended deadtime and DIB same time events. Possible on-orbit background effects on the noise power spectrum are not detectable at comparable counting rates. We did not take them into account when correcting the on-orbit power spectra. (All the data sets from celestial sources considered in this work have counting rates comparable to Cas A data due to the



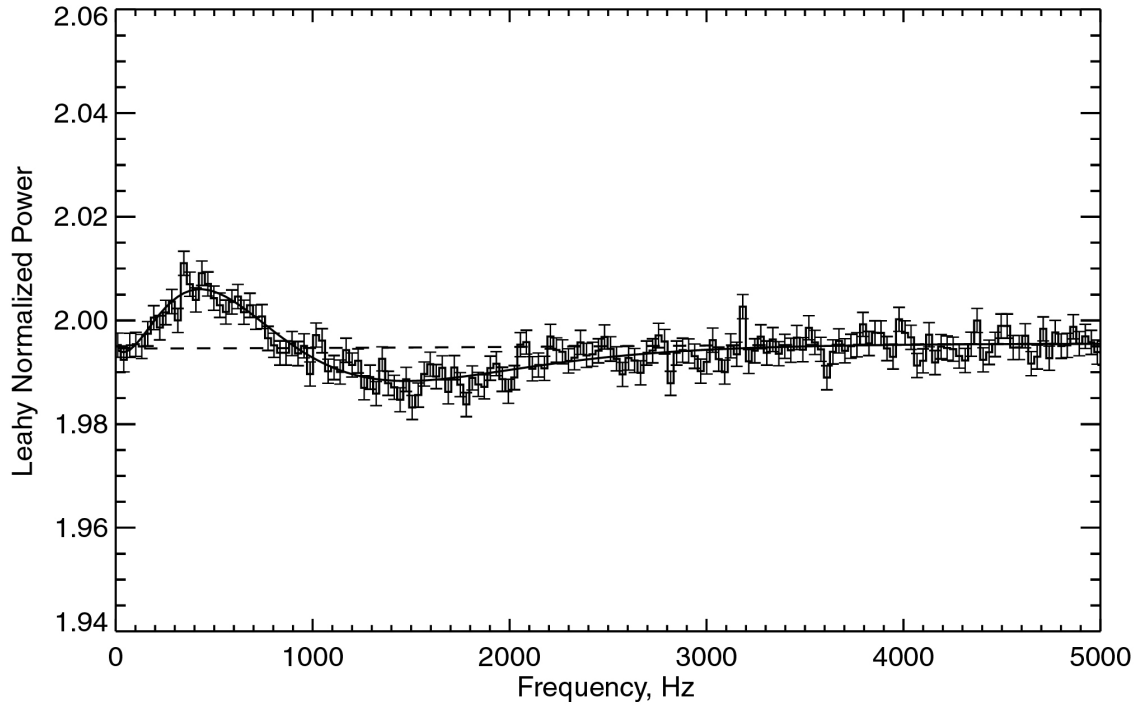


Figure 6.6 Power spectrum of the mode 1, channel 2 Cas A data fitted with (5.13).  $r_o=106$  Hz.  $t_b=96$   $\mu$ s. Total exposure time 22.7 ks. Fitting range: 300-5000 Hz. Dashed line is  $bP^{other}(f)$  (5.10).

energy cuts used). The possible effects of background on the noise, such as the effect of the perimeter veto and coincidence veto events, and the effect of large energy events, still need to be investigated for on-orbit Poisson data at high ( $\gtrsim 1000$  Hz) counting rates (Section 5.6).

### 6.4.3 Power Spectra of Cygnus X-1

Cygnus X-1 is a galactic BHC binary source with well-studied power spectrum [11], [59]. We analyzed 194 USA Cygnus X-1 observations (total exposure time 23.6 ks) in mode 1. The observations covered the period from June 12, 1999 (MJD 51341) to December 31, 1999 (MJD 51543). Cygnus X-1 was in its low state during this period.

The data analysis was similar to that of XTE J1859+226 described in Section 6.3. We

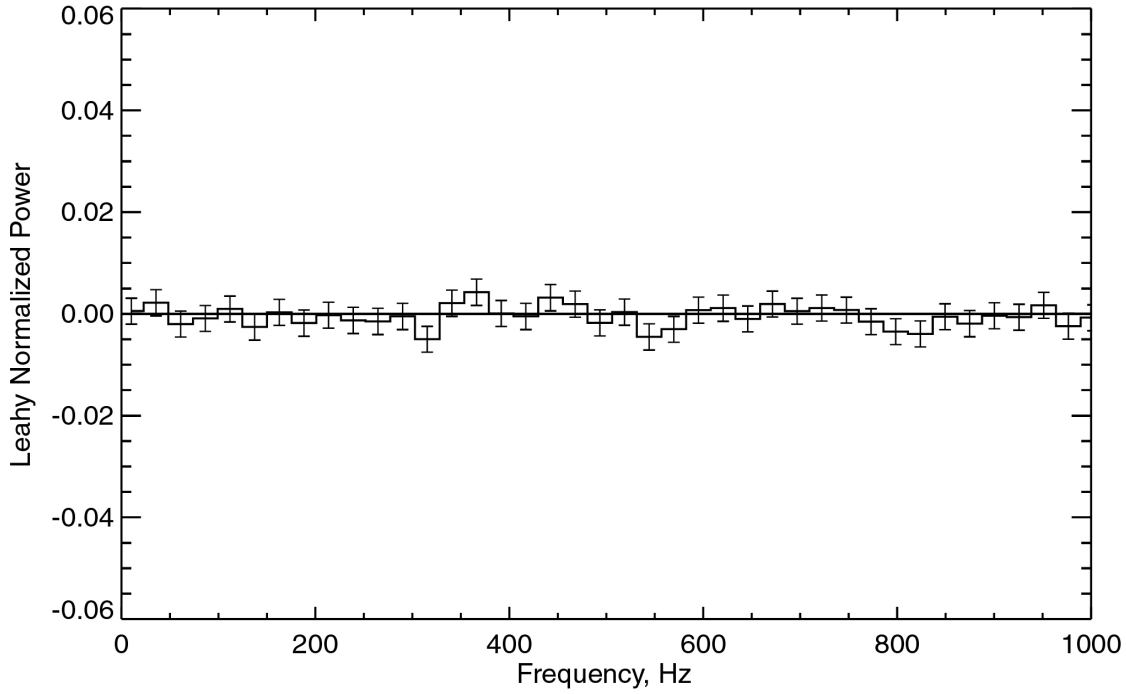


Figure 6.7 Residuals of the fit to the Cas A power spectrum with (5.13). Same data set as in Figure 6.6. Fitting range: 300-5000 Hz. The residuals are consistent with zero in  $\sim 0$ -5000 Hz region.

chose to analyze a data set that had comparable counting rate to the XTE J1859+226 data set (all the deadtime effects are rate-dependent). USA pointing was slightly different for various days of the year, thus providing Cygnus X-1 data in a variety of rates. We selected photons from energy channels 4 through 14 (4.2-19.8 keV), which is the same range as the one used for the high-frequency QPO search in XTE J1859+226.

Figure 6.8 shows the noise-subtracted power spectrum of Cygnus X-1. The noise power was determined using the procedure described in Section 5.5.2 (see Table 6.1 for the noise parameters).

The solid line in Figure 5.8 is a power law with index  $-1.53$ . To obtain this number, we fitted the noise-corrected power spectrum of Cygnus X-1 mode 2 data in the frequency range from 3 Hz to 100 Hz with a power law. We used mode 2 data (spanning the same

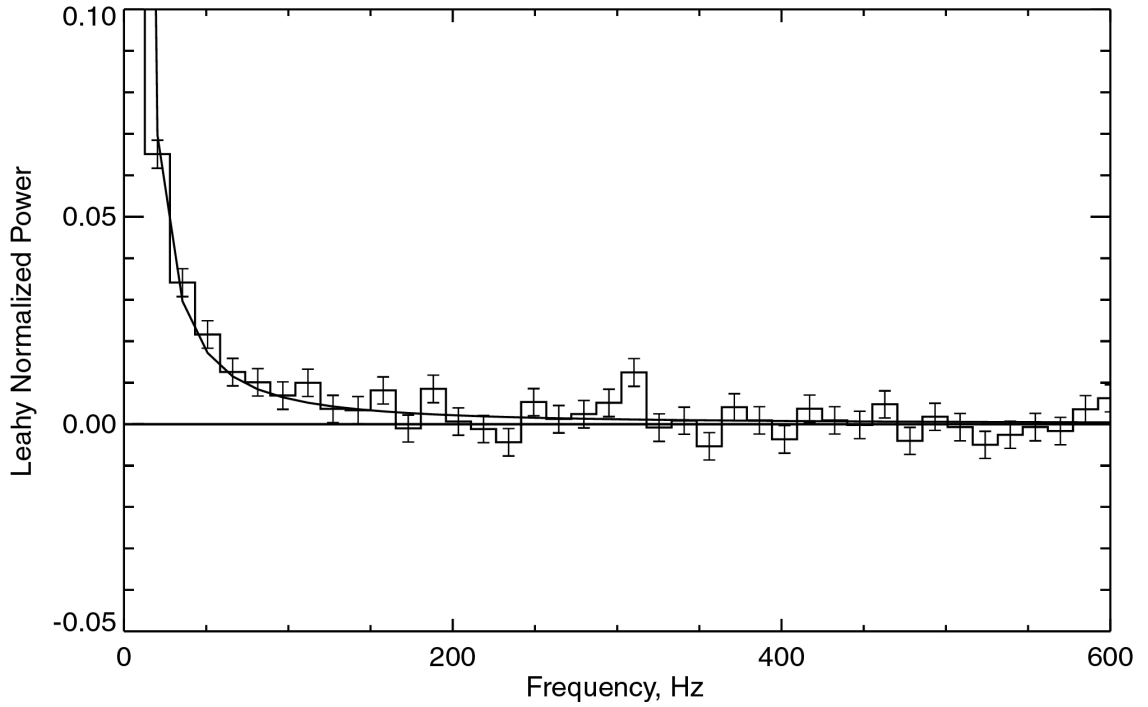


Figure 6.8 Noise-subtracted power spectrum of the mode 1 Cygnus X-1 data. Energy range: 4.2-19.8 keV.  $r_o=377$  Hz.  $t_b=96$   $\mu$ s. Total exposure time 23.6 ks. Range used to determine the noise: 320-5000 Hz. Solid line is a power law with index  $-1.53$ .

period of observations) to get better frequency resolution in this range of frequencies. We show mode 1 data in Figure 6.8 since this data has a comparable total counting rate to XTE J1859+226, and since the high-frequency QPO in XTE J1859+226 is observed in the same mode. The value resulting from the fit for the index of Cygnus X-1 in the low state is  $-1.53 \pm 0.02$ , for the 3 Hz to 100 Hz frequency range and 4.2 keV to 19.8 keV energy range. It is consistent with values previously reported by RXTE [59].

Cygnus X-1 shows clear evidence of variability up to about 200 Hz frequency. Jernigan et al. [31], applying careful deadtime corrections to the RXTE data, detected continuum variability in Cygnus X-1 up to 280 Hz. Revnivtsev et al. just recently reported similar results of variability in Cygnus X-1 up to 300 Hz from RXTE data. Our result is the first confirmation of this detection with data from a different instrument. However, some of

this power is likely to be the result of the “low-frequency leakage” in the power spectrum [18], [97] for which no correction was made either in the RXTE or in the USA data. The results for other non-transient BHC binaries up to now extend only to the 100 Hz region.

The Cas A and Cygnus X-1 analysis shows that deadtime effects are smooth and correctable with no unexplained features, and that the noise correction method gives the expected answer for the power spectrum of both sources.

## 6.5 Low-Frequency QPOs

Low-frequency QPOs in the frequency range from a fraction of a Hz to several Hz are characteristic for the outbursts of the BHC transients. Interestingly, high-frequency QPOs were always accompanied by low-frequency QPOs for all of the BHC transients showing high-frequency QPOs listed in Table 2.2.

We detected a low-frequency QPO and its harmonics on October 15 (MJD 51466) and October 16, 1999 in all but one mode 2 observation. The source was in a very high state on those dates. The rest of our data, taken in mode 1, is not suitable for low-frequency QPO detection.

Figure 6.9 shows a low-frequency QPO detected on October 15 (for the details on calculating mode 2 power spectra see Section 6.3). Channels 1 through 14 (1.1-19.8 keV) are combined. A strong fundamental frequency 4.89 Hz QPO with weaker sub-harmonic at 2.6 Hz and first harmonic at 9.84 Hz is seen.

We fitted the fundamental frequency of the QPO with a Lorentzian function (6.2) in the frequency range from 3 Hz to 9 Hz, its first harmonic with a Lorentzian function and a power law in the range 8-15 Hz, and the sub-harmonic with a Lorentzian function in the range 0.5-4 Hz. Table 6.3 summarizes the centroid frequencies, FWHM and fractional rms amplitudes for each component.

Sobczak et al. [85] have created an extensive classification of low-frequency QPOs

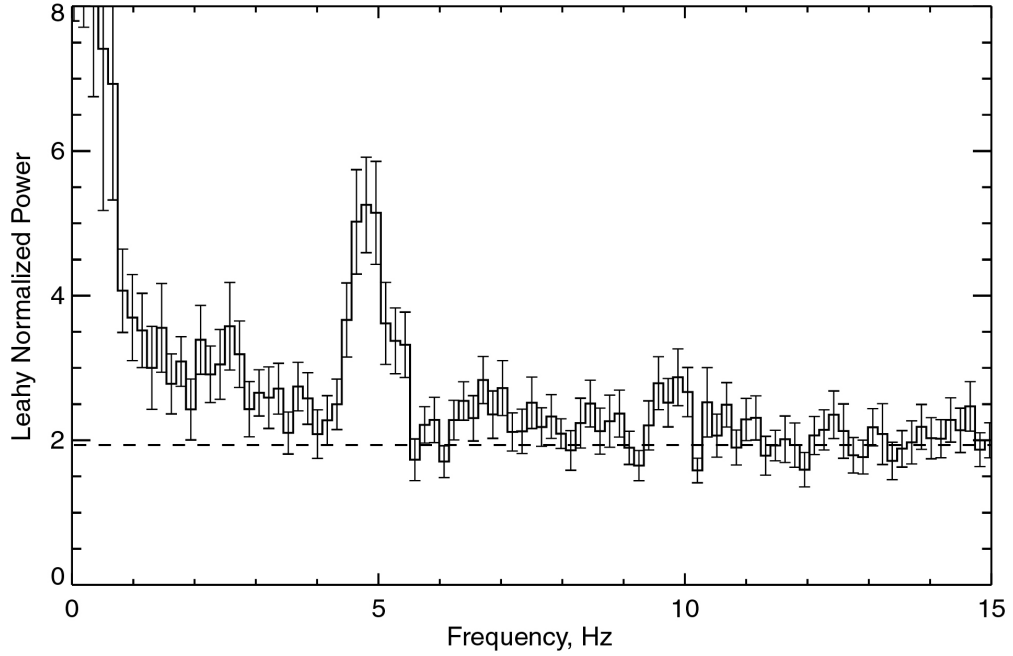


Figure 6.9 Power spectrum of the mode 2 XTE J1859+226 data. Energy range: 1.1-19.8 keV.  $r_o=1049$  Hz.  $t_b=960$   $\mu$ s. Total exposure time 0.3 ks. The power due to the noise, corrected for the deadtime is shown in a dashed line (the energy dependent instrumental effect is ignored, since it is insignificant on the shown y-scale).

during the outburst of a BHC transient XTE J1550-564. The low-frequency QPO discussed above is very similar to the type B QPOs observed in XTE J1550-564. Type B QPOs are characterized by rms amplitude  $\sim 4\%$ , frequency in the range from  $\sim 5$ -6 Hz, and  $Q \sim 10$  ( $Q = f_{qpo} / FWHM$ ). Type B QPOs are accompanied by the sub-harmonic and the first harmonic.

The low-frequency QPOs in BHC binaries form a heterogeneous class of phenomena, and their origins are hardly understood. Several mechanisms were proposed to explain their origin (see Cui [14] for a review). Ebisawa et al. [19] suggest they might be caused by a movement of obscuring structures in the outer parts of the accretion disk. Kato [33] suggests that QPOs might be related to the low-frequency c-mode oscillations in the accretion disk. There are also models that propose that QPOs originate in the Comptonizing region due to the intrinsic oscillations in the region (for more details on

QPO	Freq. (Hz)	FWHM (Hz)	Rms (%)
Sub-harmonic	2.6±0.1	0.32±0.27	2.2±0.8
Fundamental	4.89±0.04	0.46±0.1	4.9±0.4
First harmonic	9.84±0.08	0.4±0.2	2.3±0.5

Table 6.3 Results of the QPO fit. Sub-harmonic:  $\chi^2/16=0.56$ . Fundamental:  $\chi^2/33=1.17$ . First harmonic:  $\chi^2/69=0.93$ . Energy range: 1.1-19.8 keV.

these types of models see Section 6.7.2 and Cui [14]). The results of our energy dependent analysis of the low-frequency QPO in XTE J1859+226 suggests that it originates in the outer part of the accretion disk (see Section 6.7.2).

## 6.6 Temporal Properties versus Photon Energy

In this section we look at the energy dependence of the temporal properties of the source. We computed power spectra for the various energy ranges to investigate the energy dependence of the QPO components and low-frequency noise. We calculated the fractional rms amplitudes using (6.1) in the frequency ranges of interest. We chose not to fit the data, but to compute the rms, which means that our method is model-independent. This method does not completely separate various noise components, but it does provide variability values for the given frequency ranges.

Figure 6.10 shows the fractional rms amplitude of the low-frequency QPOs and the noise component at various energies. We chose the ranges for the QPO rms calculations to be  $f_{qpo} \pm \text{FWHM}$  (see Table 6.3). The low-frequency noise rms amplitude is calculated in the 0.1-1 Hz frequency range. Note that the values for the sub-harmonic may include both variability attributed to the QPO and to the low-frequency noise component in the power spectrum.

The behavior of all the components is very similar. All of them show strengthening towards higher energies. The curves are steep at low energies and level off between ~5-10 keV, suggesting saturation at high energies. The value by which the rms amplitude

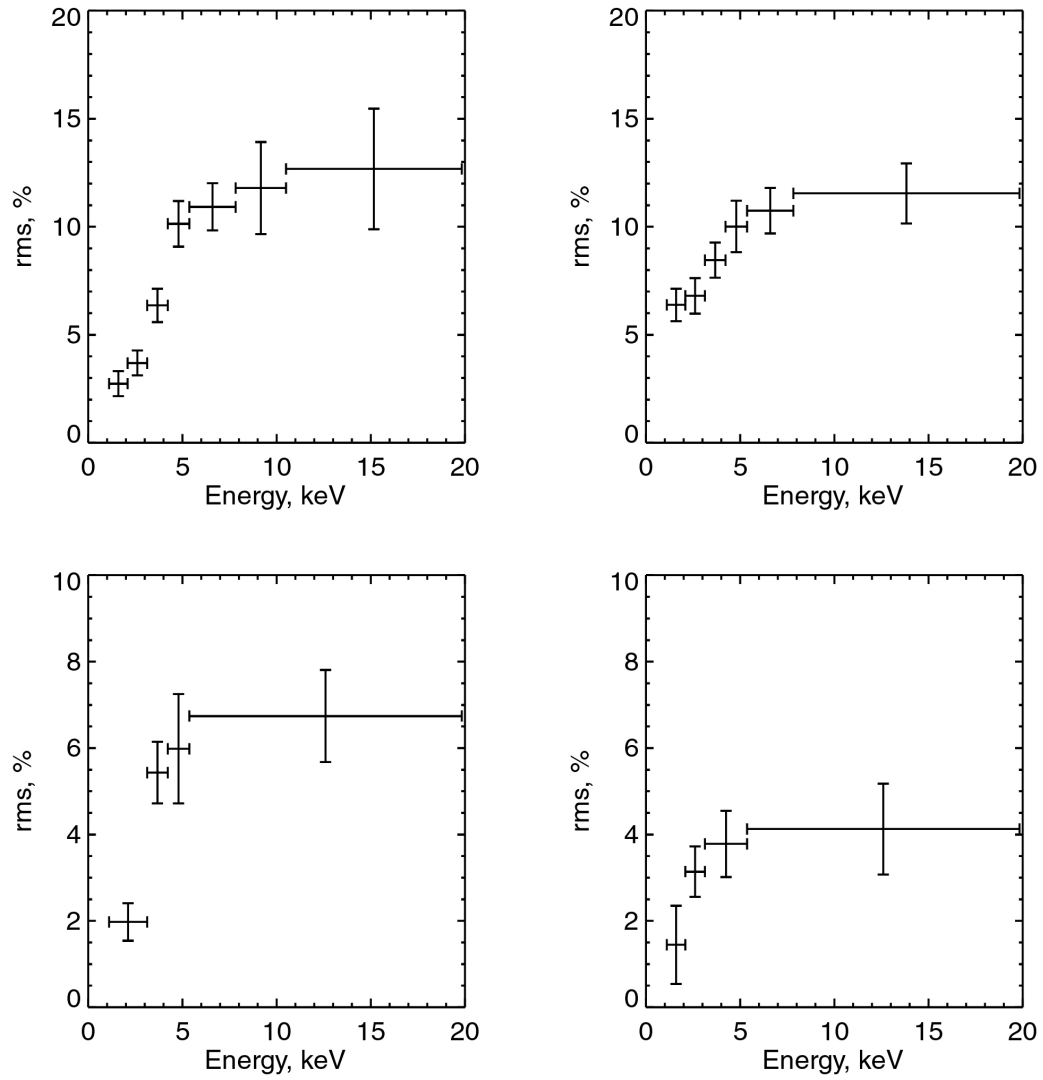


Figure 6.10 Fractional rms amplitudes as a function of energy. Clockwise from upper left: Fundamental frequency QPO, range 4.4-5.5 Hz. Low-frequency noise component, range 0.1-1 Hz. Sub-harmonic, range 2.3-2.9 Hz. First harmonic, range 9.5-10.3 Hz.

increases from 1 keV to 20 keV is different for various components and is most dramatic for the fundamental frequency component.

The strength of the high-frequency 187 Hz QPO detected by RXTE on October 18, 1999 increases with energy from  $1.0^{+0.4}_{-0.8}\%$  in 2-5.9 keV band to  $3.3^{+0.5}_{-0.7}\%$  in 5.9-60 keV band [15]. Unfortunately, due to the low statistics and the presence of an energy-dependent instrumental effect, we could not obtain a rms versus energy dependence for the high-frequency QPO detected with USA in this work

## **6.7 Discussion**

### **6.7.1 High-Frequency QPOs**

In this section we discuss the phenomenology of high-frequency QPOs detected by RXTE and USA in BHC binaries (Table 2.2) in terms of the theoretical models described in Section 2.6.

As discussed in Section 2.5, there are, possibly, two distinct groups among BHC binaries with high-frequency QPOs (in the  $\sim 100$ -300 Hz range). In GRS 1915+105, GRO J1655-40 and 4U 1630-47 the QPO frequency is stable. In two recently discovered transients, XTE J1550-564 and XTE J1859+226, the QPO frequency substantially changes from observation to observation (Table 2.2). Whether these groups represent different phenomena or the different behavior results from insufficient statistics or sporadic coverage, is to be yet discovered. There is a possibility that the stable high-frequency QPO can be a specific signature of a microquasar (both GRO J1655-40 and GRS 1915+105 are microquasars). We do not discuss 4U 1630-47, since very little information on its high-frequency QPO is available at the moment.

Initially, theories (discussed in Section 2.6) were applied to explain high-frequency QPOs in two microquasars with stable frequencies: GRS 1915+105 at 67 Hz and



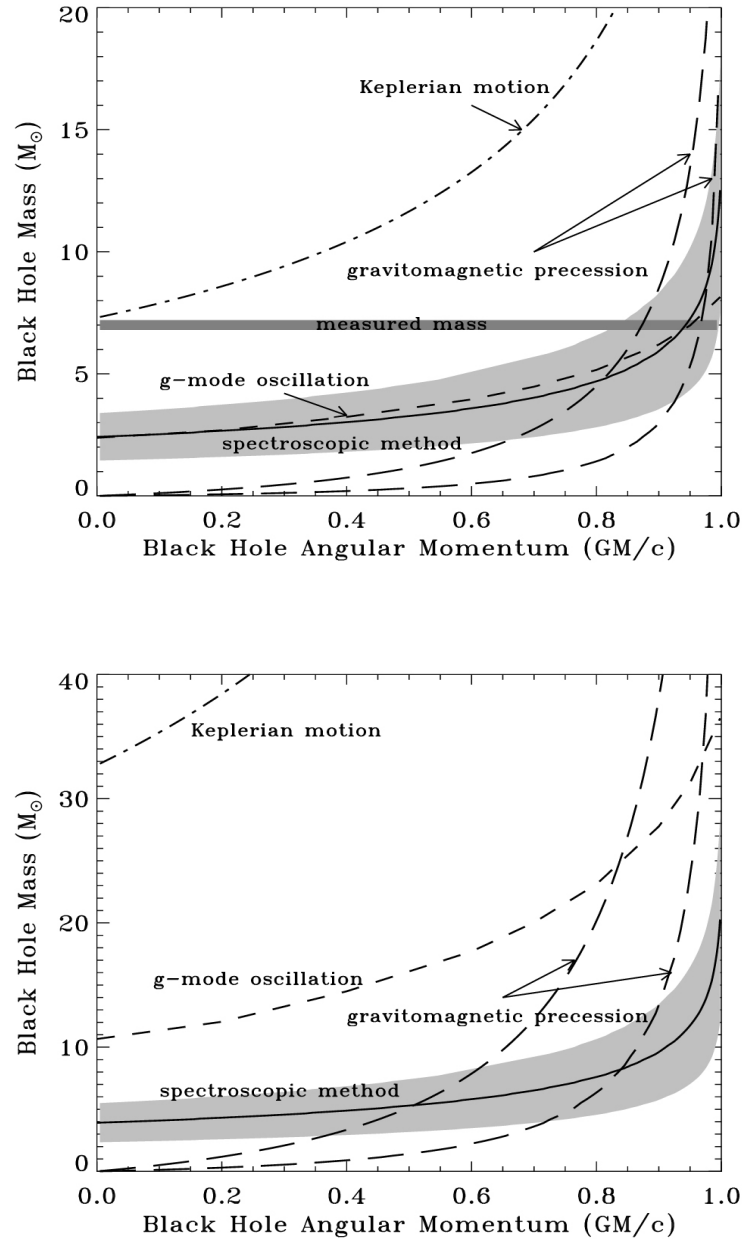


Figure 6.11 Parameter space for the mass and spin of a black hole courtesy Cui et al. [12]. Top: GRO J1655-40. Bottom: GRS 1915+105. The solid line shows the spectroscopic results of Zhang et al. [107], with the shaded region indicating the estimated uncertainty [12]. Two lines corresponding to precession model of Cui et al. (gravitomagnetic precession) were computed for the precession at the marginally stable orbit (upper curve) and at the radius where the integrated flux peaks (lower curve). The shaded area for the measured mass represents the confidence region. The mass of GRS 1915+105 is not known.

GRO J1655-40 at 295 Hz. Of particular interest is GRO J1655-40, that has a measured mass of  $7.0 \pm 0.2 M_{\odot}$  [61].

Cui et al. [12] make a comparison among the Keplerian motion model, the fundamental g-mode oscillation model, and the precession model of Cui et al. [13] for GRS 1915+105 and GRO J1655-40. For each model, the relationship between angular momentum and mass of the source is derived from the measured QPO frequency. The results are shown in Figure 6.11. In the precession model of Cui et al. two limiting cases are considered: precession at the marginally stable orbit and at the radius where the integrated flux peaks (see (2.6) for the value of  $r_{peak}$  for the geometrically thin, optically thick accretion disk).

In the Keplerian model, the frequency is calculated at a marginally stable orbit. The relationship between  $a$  and  $M$  derived from the modeling of the observed energy spectrum (spectroscopic method) is also shown with estimated measurement uncertainties [12]. The intersection between the spectroscopic curve and the model curves yields the solution to the mass and spin relationship as predicted by a particular model. For GRO J1655-40 the known mass can be used to further restrict the models.

For GRO J1655-40 the Keplerian model is ruled out, unless the black hole is non-rotating. The non-rotating black hole is incompatible with the spectroscopic model results. The g-mode model works for GRO J1655-40, predicting the angular momentum to be 93% of the maximum [39]. The precession model of Cui et al. is also in agreement with the mass measurement and the spectroscopic model. The frequency of the precession at the marginally stable orbit yields the spin of  $\sim 87\%$  of maximum rotation (giving the lower limit to the black hole spin). If it is assumed that the QPO originates from the modulation of the disk X-ray emission at the peak of the integrated flux, then the spin is  $\sim 97\%$  of the maximal rotation [12].

For GRS 1915+105, the Keplerian model, as well as the g-mode model, are inconsistent with spectroscopic measurements. The precession model of Cui et al. is consistent with spectroscopic measurements, and constrains the mass to  $\sim 3-8 M_{\odot}$  and spin to  $\sim 37-62\%$

(precession at the marginally stable orbit) and the mass to  $\sim 4-14 M_{\odot}$  and spin to  $\sim 72-90\%$  (precession at the peak effective disk temperature).

The application of the precession model by Stella et al. [86] to GRO J1655-40, gives an angular momentum parameter estimation of  $a < \sim 0.1$  (295 Hz QPO is associated with  $\nu_{per}$  and simultaneous low-frequency QPOs (on the order of several Hz) with  $2\nu_{nod}$ ). This result is in contradiction with high numbers for the angular momentum obtained by Cui et al, when 295 Hz QPO is associated with  $\nu_{nod}$ . See more discussion of the Stella et al. model below. The model cannot be applied to GRS 1915+105, since the corresponding low-frequency QPOs are not observed in the source.

The Keplerian model, diskoseismic model and precession model of Cui et al. were proposed to explain stable high-frequency QPOs in BHC binaries. The accretion disk is thought to a classical disk that extends all the way down to the marginally stable orbit in those models. The question is whether these models can accommodate the large variation in high QPO frequency, as seen in the case of XTE J1550-564 and XTE J1859+226.

The Keplerian model and precession model of Cui et al. [13] can be applied to these sources if the inner edge of the disk is allowed to move. During the 1998 outburst of XTE J1550-564, the QPO frequency changed by  $\sim 32\%$  (Table 2.2.). Since the Keplerian frequency  $\nu_{\phi} \propto r^{-3/2}$  (2.10), the change in the QPO frequency corresponds to  $\sim 22\%$  outward movement of the inner edge of the disk. The precession model of Cui et al. accommodates this change better ( $\sim 11\%$ ), since the dependence of the frequency on radius is steeper  $\nu_{nod} \propto r^{-3}$  (2.10). For XTE J1859+226, using USA frequencies 67 Hz and 193 Hz, the change for the Keplerian model is  $\sim 43\%$  and for the precession model  $\sim 22\%$ . Currently, some ADAF models for disk accretion incorporate a moving inner edge of accretion disks (see section 2.4 for the discussion).

In the g-mode oscillation model, the g-mode frequency does not essentially depend on the radius (2.11) and properties of the disk (unless luminosity exceeds Eddington,  $L \gtrsim L_{Edd}$ ,

or the inner edge of the disk moves out of the g-mode radius ( $\sim 8 M$ ), and thus this model is ruled out for the unstable frequency sources.

The precession model by Stella et al. [86] was initially developed to explain high-frequency QPOs in neutron star binaries. The frequencies of these QPOs are highly variable [98]. The change in the frequency values is explained, as well, by the change in the location of the inner edge of the disk facilitated by the change in the mass accretion rate. Stella et al. applied this model to GRO J1655-40 data and some of the data on XTE J1550-564. We applied this model to all the existing data on high-frequency QPOs for three sources: GRO J1655-40, XTE J1550-564 and XTE J1859+226. We used the frequency dependence of the  $2\nu_{nod}$  on  $\nu_{per}$  in the weak field and slow rotation approximation (2.14). The approximation breaks down at large values of the angular momentum parameter  $a$  and small values of  $r$ . However, for the purpose of this demonstration, the deviation is not significant, since it is much smaller than the deviation of the experimental data from the predictions of the model. Figure 6.12 shows the PBV (Psaltis, Belloni and van der Klis) correlation. The frequency of the low-frequency QPO is plotted versus the frequency of high-frequency QPO detected during the same observation. The references to the data sources are shown in Table 2.2. For XTE J1859+226, RXTE data is used, since we cannot associate a low-frequency QPO with the high-frequency QPO in the USA data in a single observation (the high-frequency QPOs in the USA data are observed in the combined power spectra of 50 observations). Figure 6.12 also shows the theoretically calculated curves for various values of angular momentum parameter  $a = cJ/(GM^2)$  and mass of the black hole  $m = M/M_{\odot}$ . The high-frequency end of each line is determined by the radius of the marginally stable orbit. As discussed above, GRO J1655-40 ( $m = 7$ ) data is in agreement with the model if  $a < \sim 0.1$ . Interestingly, according to the model, the 295 Hz QPO originates close to the marginally stable orbit. However, the values for XTE J1550-564 do not lie along any particular line, and thus are not consistent with particular values of mass and angular

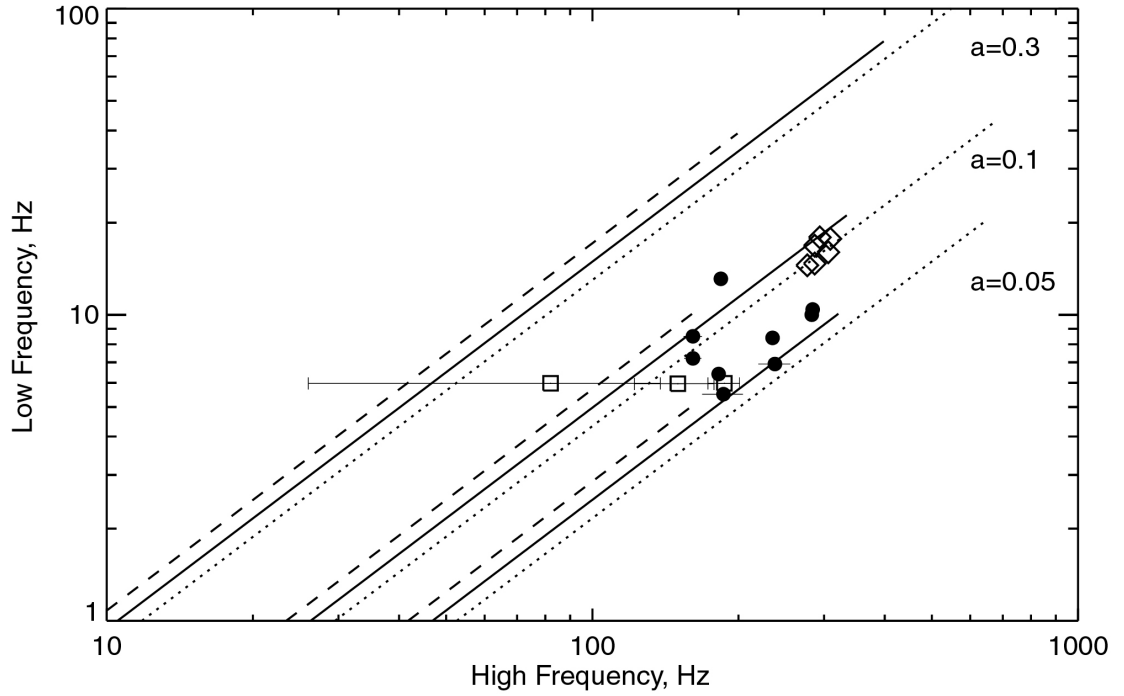


Figure 6.12 PBV correlation. The frequency of low-frequency QPO versus the frequency of the high-frequency QPO detected during the same observation. Diamonds: GRO J1655-40. Circles: XTE J1550-564. Squares: XTE J1859+226. See references in Table 2.2 for the source of data points. The lines are  $2\nu_{nod}$  versus  $\nu_{per}$  in the weak field and slow rotation approximation. Dotted line:  $m=3.5$ . Solid line:  $m=7$ . Dashed line:  $m=14$ . Three groups of lines correspond to different angular momentum parameter  $a$ .

momentum. The model most likely does not apply to XTE J1859+226 either. The RXTE power spectra of the source are not consistent with the appearance of a stable frequency QPO [15]. USA data also indicates that there is a range of frequencies in the source. While the high-frequency QPO varied wildly in frequency and shape within just one day of observations (assuming values  $187^{+14}_{-11}$  Hz,  $82^{+56}_{-26}$  Hz and  $150^{+17}_{-28}$  Hz), the low-frequency QPO remained stable within the same observations. This is not expected in the model.

XTE J1550-564 occupied four distinct “states” during its 1998 and 1999 outburst with frequencies centered around four values ( $\sim 160$  Hz,  $\sim 184$  Hz,  $\sim 236$  Hz and

$\sim 284$  Hz (Table 2.2)). The rms amplitudes of the QPOs were approximately the same. USA data on XTE J1859+226 indicates that the same interesting fact can be true for this source. There might be three dominating “states” with approximately equal rms amplitudes and with frequencies: 67 Hz, 134 Hz and 193 Hz (Table 6.2). Interestingly, the frequencies relate to each other as  $\sim 1:2:3$  within errors suggesting that they might be harmonics. RXTE frequencies for XTE J1859+226 are consistent with those of USA within errors (see Section 6.4.1). No current model provides an explanation for such behavior.

The common feature of all the BHC transients with high-frequency QPOs (Table 2.2) is an increase in the QPO rms amplitude with energy (except for GRO J1655-40, for which the detection of the 295 Hz QPO is limited only to one (2-25 keV) energy range [72]). This behavior is common for the low-frequency QPOs as well. There are two hypotheses that explain this phenomenon. One is to place the origin of the QPO in the Comptonizing region, the other hypothesis assumes the disk origin of the QPO (this model is independent of the particular QPO mechanism). We discuss these issues in the next section.

In summary, there is not sufficient evidence to strongly support any of the high-frequency QPO models. We discussed the applicability and the limitations of the several models: Keplerian, diskoseismic and relativistic precession.

### **6.7.2 Temporal Properties versus Photon Energy**

The QPOs and the broad-band noise in BHC binaries show energy and spectral state dependent variability. There is a lack of systematic studies of the dependence of broad-band variability on the energy and the spectral state (for a review consult van der Klis [96] and Cui [14] and references therein). The dependence was sporadically reported for a number of sources. The data support the idea that variability is associated with a power law component of the energy spectrum. In general, the fractional rms amplitude seems to increase with photon energy in all states for many BHC binary sources and various power

spectrum components, although a more complicated dependence (increase of rms variability and subsequent decrease with a maximum at  $\sim 5$  keV) was reported by Takizawa et al. [89] for the BHC transient GS 1124-683 (Novae Muscae) in the low-frequency broad-band component (0.12-1 Hz). It appears that for most BHC binaries, the QPOs strengthen toward the high energies, although some behave in the opposite manner [14].

The QPO fractional rms amplitude dependence on energy is proportional to the ratio of the energy spectrum of the modulated photons to the total spectrum (independent of the QPO mechanism). Thus the increase of the rms amplitude with energy means the modulated photons have a harder spectrum than the overall emission. Two possible explanations have been proposed to account for this property.

The first class of theories suggests that QPOs do not originate in the disk but in the Comptonizing region that is believed to give rise to the hard power law part of the energy spectrum. Titarchuk et al. [94], Cui et al. [11] and Lee et al. [37] speculate that QPOs are manifestations of the oscillatory nature of the Comptonizing region. Titarchuk et al. [94] suggest that the QPOs arise in the hot centrifugal barrier region that may experience relaxation oscillations (the model applies only to high-frequency QPOs). The X-ray spectrum of the photons coming from this region is upscattered by the hot electrons. Lee et al. [37] propose the time-dependent Comptonization model that allows one to determine whether the variability is due to the oscillations in the injection process of soft seed photons, in the coronal electron density, or in the coronal energy dissipation rate. Applying this model to the neutron star atoll source 4U 1608-52, they find that its 850 Hz QPO is driven predominantly by an oscillation in the electron density of the Comptonizing gas. The assumption that variability is dominated by oscillations in the injection process or coronal energy dissipation rate produces unacceptable fits to the data.

The second class of theories suggests the QPOs originate in the disk. Lehr et al. [40] propose a “Compton microscope” model that quantitatively reproduces the rms/energy dependence for the 67 Hz QPO in the BHC GRS 1915+105. In this model, the QPO

originates in the inner accretion disk, and the spectrum of modulated photons depends on the location of the QPO emitting region in the disk. The model is independent of a particular QPO mechanism. It assumes that the properties of the Compton atmosphere, the electron temperature and/or optical depth, are functions of the distance from the compact object. Due to the radial gradient of the electron temperature and/or optical depth, photons that originate closer to the compact object are more strongly Comptonized and have harder spectra than photons that originate in the outer regions of the disk. The “Compton microscope” method uses the total energy spectrum and the rms energy dependence to restrict the location of the QPO in the disk to the various annuli of area  $2\pi r dr$ . The method restricts the location of the 67 Hz QPO in GRS 1915+105 to the area between the inner edge of the disk and  $\sim 10 M$  (just outside the maximum of the radial epicyclic frequency of  $8 M$  for a non-rotating black hole) [40], where  $M$  is the black hole mass.

This model can also explain the relation of the variability strength to the strength of the power law component in the energy spectrum: the presence of a hot Comptonizing cloud associated with a power law component is essential to magnify the rms amplitude of the variability to the observable magnitude.

Figure 6.13 shows rms/energy dependence, simulated using the energy spectrum of a GRS 1915+105 observation, for various origins of the QPO in the disk (the results were provided by Lehr [38]). The upper curve fits the experimental dependence [40]. The ratio of the spectrum from modulated photons to the total disk spectrum is normalized by  $r dr$  to account for the change in flux for various locations. In general, the overall normalization is a free parameter of the model, which is obtained by fitting the data. The resulting fitted normalization gives the fraction of photons modulated by a QPO mechanism.

An interesting result of this model is that the energy dependence shows a turnover from a monotonic increase as the QPO location moves to larger radii in the disk. While the exact shape of curves in Figure 6.13 depends on the energy spectrum of the source, the



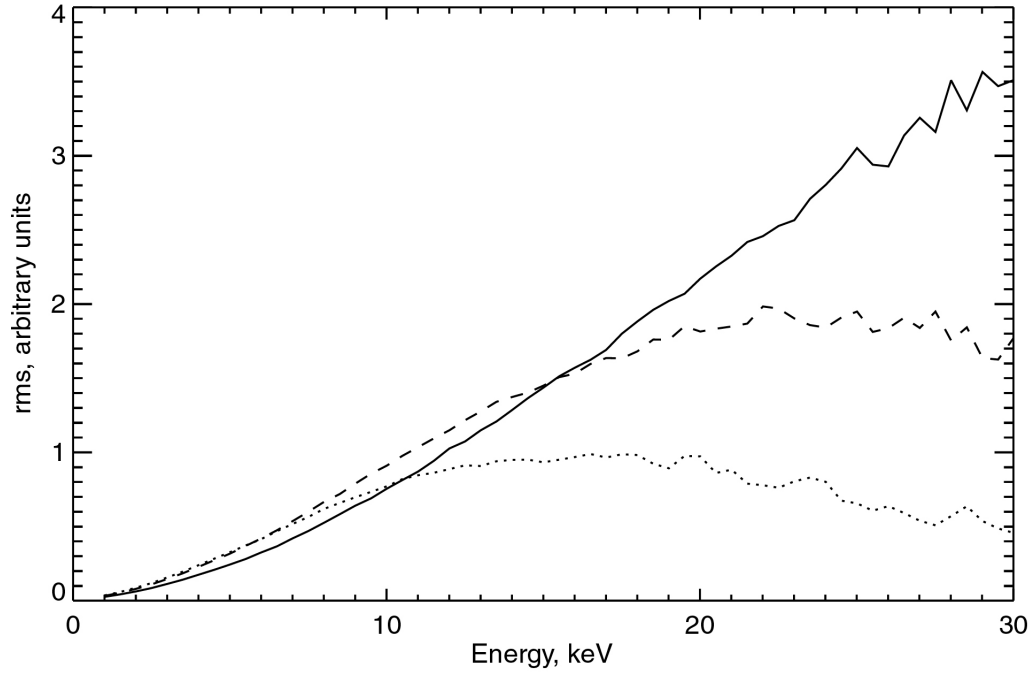


Figure 6.13 Energy dependence of a QPO in GRS 1915+105 on 1996 May 05. Plot is provided by Lehr [38]. Result of Monte Carlo simulations. Solid line: ratio of spectrum from photons injected at  $7.5\text{--}8.5 M$  to total disk spectrum. Dashed: same ratio for photons injected at  $9\text{--}10 M$ . Dotted: same ratio for photons injected at  $11\text{--}12 M$ . Normalized by  $rdr$ .

turnover of the rms amplitude with more distant locations in the disk is common for all the sources that have a Comptonizing region temperature profile decreasing with radius [39]. The low-frequency QPO (0.8-3 Hz) in GRS 1915+105 analyzed by J. A. Tomsick shows an energy dependence resembling the dotted curve in Figure 6.13, with a turnover between 10-20 keV [39]. In summary, the results for GRS 1915+105 are consistent with the idea that a high-frequency 67 Hz QPO is located closer to the compact object than the low-frequency one (0.8-3 Hz).

In light of the above model, we can interpret our low-frequency QPO results of Section 6.6 in the same manner. All the analyzed components of the power spectrum (fundamental frequency QPO, sub-harmonic, first harmonic and low-frequency noise) show a turnover in the 5-10 keV energy range (Figure 6.10). That, according to the model, indicates that the variability originates in the outer layers of the disk relative to the

radial epicyclic frequency. Interestingly, the low-frequency noise variability that is not associated with QPOs has a similar energy dependence (as well as any frequency range broad-band variability of the Figure 6.9 power spectrum). According to the model, it means that the broad-band variability also may be confined to the outer layers of the accretion disk. The value by which the rms amplitude increases from 1 keV to 20 keV is different for various components and is most dramatic for the fundamental frequency component. This can be due to the different annuli of origin in the outer layers of the disk for various components. The fundamental component, probably, originates in the layers closer to the compact object than other components.

Note that the idea that the low-frequency QPOs originate further out in the disk than the high-frequency ones contradicts the precession model of Stella et al. [86] that assumes that both types of QPOs are confined to the same narrow annulus in the disk.

As mentioned in Section 6.6, the high-frequency QPO in XTE J1859+226 shows an increase of the rms amplitude with energy. Other BHC sources listed in Table 2.2 show the same dependence (except for GRO J1655-40, for which the detection of the 295 Hz QPO is limited only to one (2-25 keV) energy range [72]). Unfortunately, sufficient quantitative data for applying the Compton microscope model exists only for GRS 1915+105. Thus for other sources we can explain the increase within this model, but cannot draw conclusions about the location of the high-frequency QPO in the accretion disk.

## CHAPTER 7: SUMMARY

In summary, in the preceding chapters we discussed the experimental work on USA preflight deadtime and timing calibration, the development of a USA Monte Carlo deadtime model and deadtime correction methods. We discussed the detection of high-frequency variability ( $\sim 40\text{-}300$  Hz) in a BHC transient XTE J1859+226 and an energy-dependent timing analysis of low-frequency power spectrum components. We discussed the findings in the context of various theoretical models.

As a result of the on-ground calibration, we were able to correct the noise power spectrum within  $\sim 0.1\%$  accuracy in the case when the energy-dependent instrumental effect was not present. The noise power spectra for various counting rates can be described with a phenomenological function. Alternatively, the Monte Carlo model of the USA deadtime can be used to reproduce noise power spectra. The Monte Carlo model assumes constant non-extended deadtime of  $16.383 \pm 0.004$   $\mu\text{s}$  and the existence of same time events (STE) introduced to the data stream by the Detector Interface Board. The practical recipes for correcting the power spectra are described in Section 5.4.7. The future investigation of the USA deadtime response based on on-orbit data is recommended. In high counting rate on-orbit data additional deadtime effects in the detector can arise due to the influence of the cosmic background.

We discussed the energy-dependent instrumental effect in the power spectra and its possible cause (Section 5.5.1). The effect is believed to originate with the variations in signal baseline after it exits the wire front-end amplifier. We developed a correction method (Section 5.5.2), based on the results of the deadtime calibration when no energy-dependent effect is present. This method allows one to correct the power spectrum for the energy-dependent effect in the  $\gtrsim 40$  Hz frequency range. Our method was tested on data with less than 500 Hz counting rate (after energy cuts). It is recommended that it not be used for higher counting rate data ( $\gtrsim 500$  Hz). We successfully applied this correction to the ground calibration data, Cas A data and Cygnus X-1 data (Sections 5.5.2, 6.4.2 and 6.4.3, respectively). For the ground and Cas A data, the resulting power spectrum is consistent with the power spectrum of a Poisson source. For Cygnus X-1 data, the resulting power spectrum is consistent with the results on this source in the low state previously published by other experiments. We suggest for the future, that a physical measurement of the amplifier baseline fluctuation as a function of counting rate and other parameters be performed on USA brass board electronics to verify our understanding of this effect.

We reported the detection of a  $20\sigma$  high-frequency signal ( $\sim 40$ -300 Hz) with  $7.7 \pm 0.4\%$  fractional rms amplitude in the BHC transient XTE J1859+226 with USA (Section 6.4.1). We applied the deadtime correction methods developed in this work to the combined Fourier power spectrum of 50 observations of the source in the high state. This detection is the first confirmation of high-frequency variability in BHC binaries with an instrument other than RXTE. The USA results can be interpreted as indicating a QPO signal that changes its frequency between three dominant “states” at 67 Hz, 134 Hz and 193 Hz.

We presented details about the observational data on five existing BHC transients that show high-frequency variability in the  $\sim 100$ -300 Hz frequency range, including XTE J1859+226 (Section 2.5). We discussed the high-frequency QPO detection in XTE J1859+226, as well as similar QPO detections in other BHC binaries, in the context of Keplerian, diskoseismic and relativistic precession theoretical models (Section 6.7.1).

Currently, the interpretation of these signals within existing models is ambiguous. We concluded that for the XTE J1859+226 signal, the g-mode diskoseismic model and precession model by Stella et al. [86] are not supported by the observational data. The accommodation by the data of the Keplerian model and precession model of Cui et al. [12] would require the inner edge of the accretion disk to move by  $\sim 43\%$  and  $\sim 22\%$ , respectively, on the scale of several hours. The detection of high-frequency signals in new BHC transients, as well as collecting more data on the sources with the detected QPOs (Table 2.2), will help to answer questions on the frequency stability of the high-frequency QPOs and the character of the rms/energy dependence for these QPOs. Mass measurements of these BHC binaries will help, as well, to constrain the existing models.

We performed an energy-dependent timing analysis of a low-frequency 4.9 Hz QPO, its harmonics, and broad-band noise in XTE J1859+226 (Section 6.7.2). Due to the low statistics and the presence of an energy dependent instrumental effect, we could not obtain a rms versus energy dependence for the high-frequency QPO detected with USA in this work. The increase of fractional rms amplitude of all low-frequency noise components with energy was seen. The result, if interpreted within the Compton microscope theoretical model, may indicate that the variability in this frequency range is confined to the outer parts of the accretion disk (Section 6.7.2). In the future, the determination of both low-frequency and high-frequency QPO locations in the accretion disk by studying their rms energy dependence should place more restrictions on high-frequency QPO models.

The USA experiment has an excellent potential for the detection of similar high-frequency signals in BHC transient sources. USA has a capability to dedicate a large fraction of its observing time to one particular source and collect sufficient statistics for a detection of weak signals. Based on the experience with XTE J1859+226, we modified the observing schedule to extensively monitor the outbursts of potential BHC transients.

## APPENDIX

### A.1 Thermal Vacuum Tests Data Used for the Analysis

Observed Rate (Hz)	Event Mode Number	Detector ID	Duration (ks)
4100	1	0	5
	3	0	55.4
	2	0	1.9
	4	0	3.4
4000	1	0	3.0
	3	0	31.3
	2	0	0.7
	4	0	1.5
3800	1	0	2.5
	3	0	4.8
	2	0	1.0
	4	0	2.1
3200	1	0	1.0
	3	0	1.8
3000	1	0	1.1
	1	1	1.6

	3	1	45.6
	2	1	2.0
	4*	0	1.3
	4	1	0.3
2600	1	1	1.2
	3	1	5.7
	2	1	2.3
	4	1	0.9
2200	1	1	3.6
	3	1	2.2
	2	1	1.4
	4	1	1.4
1900	1	1	1.5
	3	1	1.6
1600	1	1	2.3
	3	1	5.3
	2	1	2.5
	4	1	3.7
1000	4	1	1.6

Table A.1 Summary of the analyzed data from August-October 1997 and June 1998 thermal vacuum tests. The observed rates are rounded to 100 Hz. The duration is rounded to 0.1 ks. The DIB resync time for the data set marked with \* is 63  $\mu$ s. For the rest of the data the DIB resync time is 40  $\mu$ s.

## A.2 The Results of the Fits to the Power Spectra of the On-Ground Calibration Data

$t_b$ ( $\mu$ s)	Observed Rate (Hz)	Detector ID	$P_1$	$P_2 \times 10^{-2}$	$\chi^2 / \text{dof}$	DOF
32	4075	0	1.8133 $\pm$ 0.0001	- 7.58 $\pm$ 0.02	1.040	4094
	4030	0	1.8155 $\pm$ 0.0002	-7.43 $\pm$ 0.02	1.151	4094
	3836	0	1.8232 $\pm$ 0.0004	-7.07 $\pm$ 0.06	1.278	4094
	3182	0	1.8506 $\pm$ 0.0007	-5.9 $\pm$ 0.1	1.019	4094
	3009	0	1.8603 $\pm$ 0.0004	-5.65 $\pm$ 0.06	0.998	4094
	3035	1	1.8608 $\pm$ 0.0001	-5.67 $\pm$ 0.02	1.043	4094
	2594	1	1.8787 $\pm$ 0.0004	-4.90 $\pm$ 0.05	0.999	4094
	2151	1	1.8984 $\pm$ 0.0006	-3.99 $\pm$ 0.09	1.015	4094
	1884	1	1.9095 $\pm$ 0.0007	-3.5 $\pm$ 0.1	1.047	4094
	1608	1	1.9237 $\pm$ 0.0004	-3.03 $\pm$ 0.06	1.024	4094
	1035	1	1.9509 $\pm$ 0.0004	-1.97 $\pm$ 0.06	1.038	4094
96	4075	0	1.7630 $\pm$ 0.0002	-2.45 $\pm$ 0.02	1.080	2046
	4030	0	1.7663 $\pm$ 0.0002	-2.43 $\pm$ 0.03	1.125	2046
	3836	0	1.7753 $\pm$ 0.0006	-2.29 $\pm$ 0.08	1.231	2046
	3182	0	1.8109 $\pm$ 0.0009	-1.9 $\pm$ 0.1	0.983	2046
	3009	0	1.8227 $\pm$ 0.0007	-1.9 $\pm$ 0.1	1.036	2046
	3035	1	1.8232 $\pm$ 0.0002	-1.86 $\pm$ 0.03	1.050	2046
	2594	1	1.8464 $\pm$ 0.0005	-1.55 $\pm$ 0.08	1.036	2046
	2151	1	1.8715 $\pm$ 0.0009	-1.3 $\pm$ 0.1	0.981	2046
	1884	1	1.886 $\pm$ 0.001	-1.3 $\pm$ 0.1	0.994	2046
	1608	1	1.9033 $\pm$ 0.0006	-1.06 $\pm$ 0.08	1.045	2046



	1035	1	$1.9365 \pm 0.0007$	$-0.5 \pm 0.1$	0.982	2046
960	4075	0	$1.7401 \pm 0.0007$	$-0.21 \pm 0.09$	0.910	126
	4030	0	$1.7433 \pm 0.0009$	$0.0 \pm 0.1$	1.323	126
	3836	0	$1.755 \pm 0.002$	$0.2 \pm 0.3$	1.125	126
	3182	0	$1.798 \pm 0.004$	$0.7 \pm 0.5$	1.250	126
	3009	0	$1.805 \pm 0.002$	$-0.1 \pm 0.3$	1.171	126
	3035	1	$1.8057 \pm 0.0007$	$-0.3 \pm 0.1$	0.967	126
	2594	1	$1.830 \pm 0.002$	$0.0 \pm 0.3$	0.995	126
	2151	1	$1.862 \pm 0.003$	$-0.3 \pm 0.5$	0.888	126
	1884	1	$1.876 \pm 0.004$	$0.0 \pm 0.6$	1.238	126
	1608	1	$1.891 \pm 0.002$	$0.0 \pm 0.3$	1.076	126
	1035	1	$1.932 \pm 0.002$	$-0.2 \pm 0.3$	1.303	126

Table A.2 Summary of the results of the fits to the power spectra of the calibration data. The data modes used for the analysis are the same as in Table 5.4. All of the available data in these modes (see Table A.1) was used to calculate power spectra.

### A.3 The Results of the Fits to the Power Spectra of the Simulated Data

$t_b$ ( $\mu$ s)	Observed Rate (Hz)	Detector ID	$P_1$	$P_2 \times 10^{-2}$	$\chi^2 / \text{dof}$	DOF
32	4075	0	1.81443 $\pm$ 0.00007	7.267 $\pm$ 0.009	1.034	4094
	4030	0	1.81651 $\pm$ 0.00007	7.182 $\pm$ 0.009	1.023	4094
	3836	0	1.82515 $\pm$ 0.00009	-6.88 $\pm$ 0.01	0.988	4094
	3182	0	1.85444 $\pm$ 0.00008	-5.77 $\pm$ 0.01	0.989	4094
	3009	0	1.86234 $\pm$ 0.00008	-5.46 $\pm$ 0.01	0.970	4094
	3035	1	1.85984 $\pm$ 0.00006	5.504 $\pm$ 0.008	1.020	4094
	2594	1	1.87996 $\pm$ 0.00008	-4.75 $\pm$ 0.01	0.977	4094
	2151	1	1.90020 $\pm$ 0.00007	-3.95 $\pm$ 0.01	0.977	4094
	1884	1	1.91244 $\pm$ 0.00007	3.477 $\pm$ 0.009	0.955	4094
	1608	1	1.92528 $\pm$ 0.00006	2.993 $\pm$ 0.008	1.004	4094
	1035	1	1.95178 $\pm$ 0.00005	1.933 $\pm$ 0.007	0.959	4094
96	4075	0	1.7659 $\pm$ 0.0001	-2.38 $\pm$ 0.02	1.015	2046
	4030	0	1.7684 $\pm$ 0.0001	-2.37 $\pm$ 0.02	0.972	2046
	3836	0	1.7794 $\pm$ 0.0002	-2.28 $\pm$ 0.02	1.034	2046
	3182	0	1.8162 $\pm$ 0.0001	-1.91 $\pm$ 0.02	0.952	2046
	3009	0	1.8258 $\pm$ 0.0001	-1.82 $\pm$ 0.02	0.991	2046
	3035	1	1.82319 $\pm$ 0.00009	-1.84 $\pm$ 0.01	1.000	2046
	2594	1	1.8483 $\pm$ 0.0001	-1.56 $\pm$ 0.02	1.004	2046
	2151	1	1.8738 $\pm$ 0.0001	-1.30 $\pm$ 0.02	0.990	2046
	1884	1	1.8894 $\pm$ 0.0001	-1.18 $\pm$ 0.02	0.998	2046

	1608	1	$1.9053 \pm 0.0001$	$-0.98 \pm 0.01$	0.977	2046
	1035	1	$1.93885 \pm 0.00008$	$-0.67 \pm 0.01$	1.053	2046
960	4075	0	$1.7443 \pm 0.0003$	$-0.16 \pm 0.05$	1.072	126
	4030	0	$1.7470 \pm 0.0003$	$-0.21 \pm 0.05$	1.147	126
	3836	0	$1.7583 \pm 0.0005$	$-0.21 \pm 0.07$	0.944	126
	3182	0	$1.7983 \pm 0.0004$	$-0.24 \pm 0.06$	0.893	126
	3009	0	$1.8090 \pm 0.0004$	$-0.29 \pm 0.06$	0.842	126
	3035	1	$1.8069 \pm 0.0003$	$-0.21 \pm 0.04$	1.210	126
	2594	1	$1.8343 \pm 0.0004$	$-0.18 \pm 0.06$	1.090	126
	2151	1	$1.8627 \pm 0.0004$	$-0.12 \pm 0.05$	0.835	126
	1884	1	$1.8788 \pm 0.0004$	$-0.08 \pm 0.05$	0.980	126
	1608	1	$1.8963 \pm 0.0003$	$-0.07 \pm 0.05$	0.894	126
	1035	1	$1.9334 \pm 0.0003$	$-0.01 \pm 0.04$	1.117	126

Table A.3 Summary of the results of the fits to the power spectra of the simulated data. The amount of Monte Carlo events exceeded several times the amount of the data, listed in Table A.1.

#### A.4 List of XTE J1859+226 USA Fits Files

Fits Files (Very High State)	Fits Files (High State)
USA_2_Y1999_D288_002447_D288_003832	USA_1_Y1999_D314_142446_D314_142755
USA_1_Y1999_D289_043601_D289_045123	USA_1_Y1999_D314_142748_D314_143326
USA_1_Y1999_D289_061702_D289_063320	USA_1_Y1999_D314_160657_D314_161329
USA_1_Y1999_D289_075902_D289_081450	USA_1_Y1999_D314_174717_D314_175350
USA_2_Y1999_D289_220754_D289_222151	USA_1_Y1999_D314_192701_D314_193527
USA_2_Y1999_D289_234957_D290_000327	USA_1_Y1999_D315_123418_D315_123540
USA_1_Y1999_D291_004053_D291_005314	USA_1_Y1999_D315_140646_D315_141544
USA_1_Y1999_D291_022231_D291_023541	USA_1_Y1999_D315_190944_D315_191809
USA_1_Y1999_D291_040407_D291_041730	USA_1_Y1999_D317_234002_D317_235227
USA_1_Y1999_D291_072722_D291_074033	USA_1_Y1999_D318_012139_D318_013521
USA_1_Y1999_D291_105036_D291_110249	USA_1_Y1999_D318_030317_D318_031723
USA_1_Y1999_D291_123213_D291_124351	USA_1_Y1999_D318_044455_D318_045849
USA_1_Y1999_D291_141515_D291_142429	USA_1_Y1999_D318_062631_D318_064032
USA_1_Y1999_D291_155752_D291_160432	USA_1_Y1999_D318_113124_D318_114406
USA_1_Y1999_D291_173812_D291_174021	USA_1_Y1999_D318_131459_D318_132303
USA_1_Y1999_D291_174013_D291_174443	USA_1_Y1999_D318_145715_D318_150529
USA_1_Y1999_D292_135715_D292_140057	USA_1_Y1999_D318_163835_D318_164524
USA_1_Y1999_D292_140045_D292_140729	USA_1_Y1999_D318_181847_D318_182036
USA_1_Y1999_D293_115732_D293_120935	USA_1_Y1999_D318_195931_D318_200829
USA_1_Y1999_D293_133910_D293_135022	USA_1_Y1999_D319_125530_D319_130751
USA_1_Y1999_D293_152319_D293_153033	USA_1_Y1999_D319_144014_D319_144828
USA_1_Y1999_D294_132149_D294_133313	USA_1_Y1999_D319_162209_D319_162823
USA_1_Y1999_D295_144812_D295_145643	USA_1_Y1999_D319_180203_D319_180843
USA_1_Y1999_D295_163023_D295_163639	USA_1_Y1999_D319_194213_D319_194515
USA_1_Y1999_D295_181001_D295_181658	USA_1_Y1999_D319_194504_D319_195054
USA_1_Y1999_D297_155551_D297_160230	USA_1_Y1999_D320_091512_D320_092836
USA_1_Y1999_D298_103054_D298_104330	USA_1_Y1999_D323_132840_D323_134011

USA_1_Y1999_D298_121231_D298_122433	USA_1_Y1999_D323_151226_D323_152022
USA_1_Y1999_D299_170220_D299_170834	USA_1_Y1999_D323_165404_D323_170035
USA_1_Y1999_D299_184121_D299_184652	USA_1_Y1999_D324_062428_D324_063824
USA_1_Y1999_D301_144628_D301_145441	USA_1_Y1999_D324_080605_D324_081945
USA_1_Y1999_D302_124453_D302_125647	USA_1_Y1999_D324_094743_D324_100106
USA_1_Y1999_D302_142910_D302_143741	USA_1_Y1999_D324_112921_D324_114202
USA_1_Y1999_D302_193122_D302_193950	USA_1_Y1999_D324_131058_D324_132256
USA_1_Y1999_D303_191403_D303_192216	USA_1_Y1999_D324_145451_D324_150322
USA_1_Y1999_D304_135310_D304_135740	USA_1_Y1999_D324_163703_D324_164317
USA_1_Y1999_D304_135728_D304_140324	USA_1_Y1999_D324_181713_D324_182354
USA_1_Y1999_D304_153628_D304_154328	USA_1_Y1999_D324_195727_D324_200229
USA_1_Y1999_D304_185646_D304_190442	USA_1_Y1999_D324_200217_D324_200623
USA_1_Y1999_D306_150125_D306_150937	USA_1_Y1999_D324_232042_D324_233247
USA_1_Y1999_D306_164319_D306_164703	USA_1_Y1999_D325_010220_D325_011541
USA_1_Y1999_D306_164654_D306_164932	USA_1_Y1999_D325_042534_D325_043940
USA_1_Y1999_D306_182255_D306_183009	USA_1_Y1999_D325_125343_D325_130546
USA_1_Y1999_D306_200345_D306_201238	USA_1_Y1999_D325_143810_D325_144103
USA_1_Y1999_D307_125958_D307_131201	USA_1_Y1999_D325_162005_D325_162617
USA_1_Y1999_D307_144424_D307_145237	USA_1_Y1999_D325_175958_D325_180206
USA_1_Y1999_D308_124241_D308_124833	USA_1_Y1999_D325_180154_D325_180637
USA_1_Y1999_D308_161459_D308_161533	USA_1_Y1999_D325_194011_D325_194849
USA_1_Y1999_D308_174907_D308_175536	USA_1_Y1999_D326_073130_D326_074525
USA_1_Y1999_D308_192910_D308_193731	USA_1_Y1999_D326_091308_D326_092629

Table A.4 List of XTE J1859+226 USA fits files. The files correspond to 50 observations in the very high state and 50 observations in the high state used for the analysis in this thesis. The number after the letter Y is the calendar year and after D is the day number of observation counting from January 1<sup>st</sup>. For the reference, Y\_1999\_D288 corresponds to October 15, 1999 or MJD51466.

## REFERENCES

- [1] Benensohn, J. S., Lamb, D. Q., & Taam, R. E. 1997, *ApJ*, 478, 723
- [2] Bisnovaty-Kogan, G. S., & Blinnikov, S. I. 1977, *A&A*, 59, 111
- [3] Bloom, E. B. 1994, Particle Physics, Astrophysics & Cosmology, Proceedings of the XXII SLAC Summer Institute on Particle Physics, SLAC-Report 484, 133
- [4] Bradt, H. V., Rothschild, R. E., & Swank, J. H. 1993, *A&A*, S97, 355
- [5] Boyer, R. H., & Lindquist, R. W. 1967, *J. Math. Phys.*, 8, 265
- [6] Carter, B. 1979, General Relativity: An Einstein Centenary Survey, The General Theory of the Mechanical, Electromagnetic and Thermodynamic Properties of Black Holes, ed S. W. Hawking and W. Israel (Cambridge: Cambridge Univ. Press)
- [7] Chakrabarti, S. K., & Titarchuk, L. G. 1995, *ApJ*, 455, 623
- [8] Chaput, C., Bloom, E., Cominsky, L., Godfrey, G., Hertz, P., Scargle, J., Shabad, G., Wen H., Wood, K., & Yentis, D. 2000, *ApJ*, 541, accepted, astro-ph/9901131
- [9] Chen, W., Shrader, C. R., & Livio, M. 1997, *ApJ*, 491, 312

- [10] Conti, P. S. 1978, A&A, 63, 225
- [11] Cui, W., Zhang, S. N., Focke, W., & Swank, J. H. 1997, ApJ, 484, 383
- [12] Cui, W., Chen, W., & Zhang, S. N. 1998, astro-ph/9811023
- [13] Cui, W., Zhang, S. N., & Chen, W. 1998, ApJ, 492, L53
- [14] Cui, W. 1999, ASP Conf. Ser. 161, High Energy Processes in Accreting Black Holes, ed. J. Poutanen & R. Svensson (San Francisco: ASP), 97, astro-ph/9809408
- [15] Cui, W., Shrader, C. R., Haswell, C. A., & Hynes, R. I. 2000, ApJ, 535, L123
- [16] Dal Fiume, D., et al. 1999, IAU Circ. 7291
- [17] Davis, R. E., & Pringle, J.E. 1980, MNRAS, 191, 599
- [18] Deeter, J. 1985, ApJ, 281, 482
- [19] Ebisawa, K., Mitsuda, K., & Inoue, H. 1989, PASJ, 41, 519
- [20] Eddington, A. S. 1926, The Internal Constitution of the Stars, (Cambridge: Cambridge Univ. Press)
- [21] Esin, A. A., McClintock, J. E., & Narayan, R. 1997, ApJ, 489, 865
- [22] Focke, W. B., Markwardt, C. B., Swank, J. H., & Taam, R. E. 2000, BAAS, 195, 12602
- [23] Garnavich, P.M., & Quinn, J. 2000, IAU Circ. 7388
- [24] Godfrey, G., & Shabad, G. 1998, Charge Injection Study of the USA Brass Board Electronics, SLAC Astro Gravity Note 26.
- [25] Godfrey, G. 2000, private communication

- [26] Hanawa, T. 1989, ApJ, 341, 948
- [27] Hawley, J., Balbus, & Steven, A. 1999, ASP Conf. Ser. 160, Astrophysical Disks, ed. J. Sellwood & J. Goodman (San Francisco: ASP), 108
- [28] Hertz, P. 1994, USA Standard Data Modes, Memo USA-SWG-004
- [29] Homan, J., Wijnands, R., & van der Klis, M. 1999, IAU Circ. 7121
- [30] Horowitz, P., & Hill, W. 1989, The Art of Electronics, 2d ed, (Cambridge: Cambridge Univ. Press), p. 520
- [31] Jernigan, J. G., Klein, R. I., & Arons, J. 2000, ApJ, 530, 875
- [32] Kato, S., & Fukue, J. 1980, PASJ, 32, 377
- [33] Kato, S. 1990, PASJ, 42, 99
- [34] Kerr, R. P. 1963, Phys. Rev. Lett., 11, 237
- [35] King, A. 1995, in X-Ray Binaries, ed. W. H. G. Lewin, J. van Paradijs, & E. P. J. van der Heuvel (Cambridge: Cambridge Univ. Press)
- [36] Leahy, D.A., Darbro, W., Elsner, R. F., Weisskopf, M. C., Sutherland, P. G., Kahn, S., & Grindlay, J.E. 1983, ApJ, 266, 160
- [37] Lee, H. C., & Miller, G. S. 1998, MNRAS, 299, 479
- [38] Lehr, D. 2000, private communication
- [39] Lehr, D. 2000, Ph.D. Thesis, Observational Diagnostics of Relativistic Accretion Disks and Their Central Compact Objects, Physics Department, Stanford University
- [40] Lehr, D., Wagoner, R., V., & Wilms, J. 2000, ApJL, submitted, astro-ph/0004211



- [41] Lense, J., & Thirring, H. 1918, *Physik Z.*, 19, 156
- [42] Liang, E. P. T., Price, R. H. 1977, *ApJ*, 218, 247
- [43] Lochner, J. C., Swank, J. H., & Szymokowiak, A. E. 1989, *ApJ*, 337, 823
- [44] Markwardt, C. B., Marshall, F. E., & Swank, J. H. 1999, *IAU Circ.* 7274
- [45] Markwardt, C. B., Focke, W. B., Swank, J. H., & Taam, R. E. 2000, *BAAS*, 195, 12603
- [46] Matsuda, T., Inoue, M., & Sawada, K. 1987, *MNRAS*, 226, 785
- [47] McClintock, J. E., Remillard, R. A., & Tomsick, J. A. 2000, *IAU Circ.* 7466
- [48] McCollough, M. L., & Wilson, C. A. 1999, *IAU Circ.* 7282
- [49] Meekins, J. F., Wood, K. S., Hedler, R. L., Byram, E. T., Yentis, D. J., Chubb, T. A., & Friedman, H. 1984, *ApJ*, 278, 288
- [50] Merloni, A., Vietri, M., Stella, L., & Bini, D. 1999, *MNRAS*, 304, 155
- [51] Mendez, M., Belloni, T., & van der Klis, M. 1998, *ApJ*, 499, L187
- [52] Morgan, E. H., Remillard, R. A., & Greiner J. 1997, *ApJ*, 482, 993
- [53] Muller J.W. 1973, *Nucl. Instr. Meth.*, 112, 47
- [54] Narayan, R. 1996, *ApJ*, 462, 136
- [55] Novikov, I. D., & Thorne, K. S. 1973, in *Black Holes*, ed. C. DeWitt & B. DeWitt (New York: Gordon & Breach), 343
- [56] Nowak, M. A., & Wagoner, R. V. 1992, *ApJ*, 393, 697
- [57] Nowak, M. A., & Wagoner, R. V. 1993, *ApJ*, 418, 187

- [58] Nowak, M. A., Wagoner, R. V., Begelman, M. C., & Lehr, D. E. 1997, *ApJ*, 477, L91
- [59] Nowak, M. A., Vaughan, B. A., Wilms, J., Dove J. B., & Begelman, M. C. 1999, *ApJ*, 510, 874
- [60] Okazaki, A. T., Kato, S., & Fukue, J. 1987, *PASJ*, 39, 457
- [61] Orosz, J. A., & Bailyn, C. D. 1997, *ApJ*, 477, 860
- [62] Ostriker, J. P. 1976, *ApJ*, 218, 243
- [63] Page, D. N., & Thorne, K. S. 1974, *ApJ*, 191, 499
- [64] Perez, C. A., Silbergleit, A. S., Wagoner, R. V., & Lehr, D. E. 1997, *ApJ*, 476, 589
- [65] Petterson, J. A. 1978, *ApJ*, 224, 625
- [66] Press, W., & Schechter, P. 1974, *ApJ*, 193, 437
- [67] Psaltis, D., Belloni, T., & van der Klis, M. 1999, *ApJ*, 520, 262
- [68] Ray, P. S., Wood, K. S., Fritz, G., Hertz, P., Kowalski, M., Johnson, W. N., Lovellette, M. N., Wolff, M. T., Yentis, D., Bandyopadhyay, R. M., Bloom, E. D., Giebels, B., Godfrey, G., Reilly, K., Saz Parkinson, P., Shabad, G., Michelson, P., Roberts, M., Leahy, D. A., Cominsky, L., Scargle, J., Beall, J., Chakrabarty, D., & Kim, Y. 1999, *astro-ph/9911236*
- [69] Remillard, R. A., McClintock, J. E., Sobczak, G. J., Bailyn, C. D., Orosz, J. A., Morgan, E. H., & Levine, A. M. 1999, *ApJ*, 517, L127
- [70] Remillard, R. A., Morgan, E. H. 1999, *AAS Meeting 195*, 3702
- [71] Remillard, R., Morgan, E., Levine, A., McClintock, J., Bailyn, C., Jain, R., & Orosz, J. 1999, *IAU Circ.* 7123

- [72] Remillard, R. A., Morgan, E. H., McClintock, J. E., Bailyn, C. D., & Orosz, J. A. 1999, *ApJ*, 522, 397
- [73] Remillard, R. A. 2000, private communication
- [74] Revnivtsev, M., Gilfanov, M., & Churazov, E. 2000, *A&A* accepted, astro-ph/0007092
- [75] Rhoades, C. E., & Ruffini, R. 1974, *Phys. Rev. Lett.*, 32, 324
- [76] Rothschild, R. E., Boldt, E. A., Holt, S. S., & Serlemitsos, P. J. 1974, *ApJ*, 189, L13
- [77] Rutledge, R. E., Lewin, W. H. G., van der Klis, M., van Paradijs, J., Dotani, T., Vaughan, B., Belloni, T., Oosterbroek, T., & Kouveliotou, C. 1999, *ApJS*, 124, 265
- [78] Saz Parkinson, P. 2000, private communication
- [79] Shakura, N. I., & Sunyaev, R. A. 1973, *A&A*, 24, 337
- [80] Shapiro, S. L., & Lightman, A. P. 1976, *ApJ*, 204, 555
- [81] Shapiro, S. L., & Teukolsky, S. A. 1983, *Black Holes, White Dwarfs, and Neutron Stars*, (John Wiley & Sons, Inc)
- [82] Silbergleit, A. S., Wagoner, R. V., & Ortega-Rodriguez, M. 2000, *ApJ* submitted, astro-ph/0004114
- [83] Sobczak, G. J., McClintock, J. E., Remillard, R. A., Levine, A. M., Morgan, E. H., Bailyn, C. D., & Orosz, J. A. 1999, *ApJ*, 517, L121
- [84] Sobczak, G. J., McClintock, J. E., Orosz, J. A., & Bailyn, C. D. 2000, *ApJ*, 531, 537

- [85] Sobczak, G. J., Remillard, R. A., Muno, M. P., & McClintock, J. E. 2000, astro-ph/0004215
- [86] Stella, L., Vietri, M., & Morsink, S. M. 1999, ApJ, 524, L63
- [87] Sunyaev, R., & Revnivitsev, M. 2000, A&A, 358, 617
- [88] Schwarzschild, K. 1916, Sitzungsberichte der Deutschen Akademie der Wissenschaften zu Berlin, Klasse für Mathematik, Physik, und Technik, 189
- [89] Takizawa, M., Dotani, T., Mitsuda, K., Matsuba, E., Ogawa, M., Aoki, T., Asai, K., Ebisawa, K., Makishima, K., Miyamoto, S., Iga, S., Vaughan, B., Rutledge, R. E., & Lewin, W. H. G. 1997, ApJ, 489, 272
- [90] Tanaka, Y., & Lewin, W. H. G. 1995, X-Ray Binaries, ed. W. H. G. Lewin, J. van Paradijs, & E. P. J. van der Heuvel (Cambridge: Cambridge Univ. Press)
- [91] Tanaka, Y., & Shibazaki, N. 1996, ARA&A, 34, 607
- [92] Thorne, K. S. 1974, ApJ, 191, 507
- [93] Thorne, K. S., & Price, R. H. 1975, ApJ, 195, L101
- [94] Titarchuk, L., Lapidus, I., & Muslimov, A. 1998, ApJ, 499, 315
- [95] van der Klis, M. 1989, Proc. NATO Advanced Study Institute “Timing Neutron Stars”, Cesme, Turkey, NATO ASI Series C, 262, 27
- [96] van der Klis, M. 1995, X-Ray Binaries, ed. W. H. G. Lewin, J. van Paradijs, & E. P. J. van der Heuvel (Cambridge: Cambridge Univ. Press)
- [97] van der Klis, M. 1997, astro-ph/9704273
- [98] van der Klis, M. 2000, astro-ph/0001167

- [99] Wagoner, R. W. 1999, PhR, 311, 259
- [100] Wen, H. C. 1997, Ph.D. Thesis, 10 Microsecond Time Resolution Studies of Cygnus X-1, Physics Department, Stanford University
- [101] Weisskopf, M. C., & Sutherland, P. G. 1978, ApJ, 221, 228
- [102] White, N. E., Nagase, F., & Parmar, A. N. 1995, X-Ray Binaries, ed. W. H. G. Lewin, J. van Paradijs, & E. P. J. van der Heuvel (Cambridge: Cambridge Univ. Press)
- [103] Wilkins, D. C. 1972, Phys. Rev. D, 5, 814
- [104] Wolff, M.T., & Leahy D.A. 1998, USA Handbook, Draft 1
- [105] Wood, A., Smith, D. A., Marshall, F. E., & Swank, J. H. 1999, IAU Circ. 7274
- [106] Zhang, W., Jahoda, K., Swank, J. H., Morgan, E. H., & Giles, A. B. 1995, ApJ, 449, 930
- [107] Zhang, S. N., Cui, W., & Chen, W. 1997, ApJ, 482, L155
- [108] Zhang W., & Jahoda, K. 1998, Deadtime Effects in the PCA, RXTE Calibration Memo



